

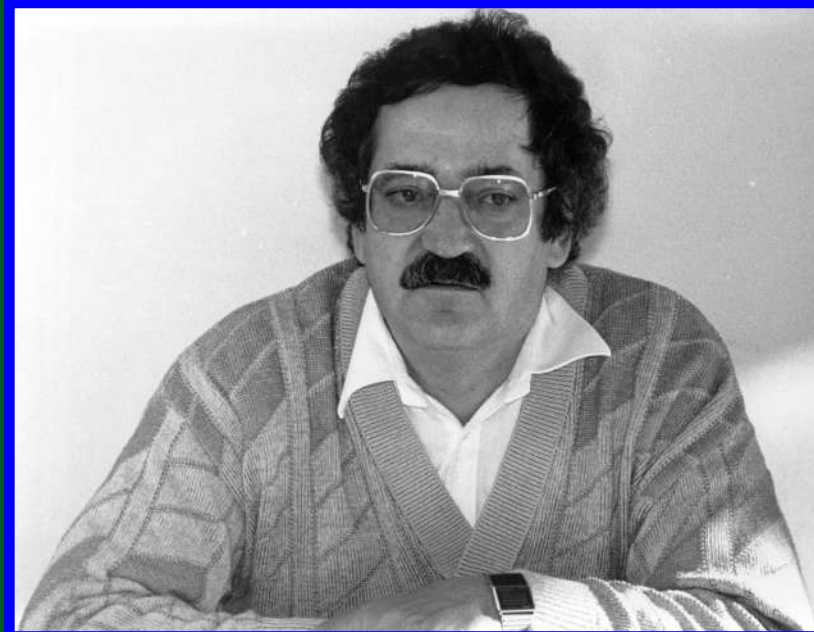
AJP

ISSN : 0971 - 3093

Vol 25, No 2, February, 2016

ASIAN JOURNAL OF PHYSICS

An International Research Journal



Professor Wolfgang Kiefer



ANITAPUBLICATIONS

FF-43, 1st Floor, Mangal Bazar, Laxmi Nagar, Delhi-110 092, India
B O : 2, Pasha Court, Williamsville, New York-14221-1776, USA

Asian Journal of Physics

Edited by
Jürgen Popp
&
Michael Schmitt

Asian Journal of Physics

Volume 25

Number 2

February, 2016

Special Issue
in
Honour of Professor Wolfgang Kiefer
on
the occasion of his 75th birthday



Prof Wolfgang Kiefer during ICOPVS-2006



ANITA PUBLICATIONS

FF-43, 1st Floor, Mangal Bazar, Laxmi Nagar, Delhi-110 092, India

Website : <http://asianjournalofphysics.in>

Asian Journal of Physics

(A Publication Not for Profit)

Volume 25, No 2 (2016)

CONTENTS

Editorial

Guest Editorial

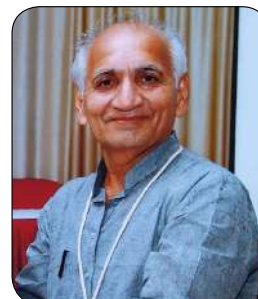
About the Guest Editor

- Two dimensional graphene derivatives supported isolated gold nanoparticles as an efficient SERS substrate
Shiju Abraham, Matthias König, Shobhit Pandey, Sunil K Srivastava, Bernd Walkenfort and Anchal Srivastava 121
- Encapsulation of optical gratings using nanoporous alumina layers
Lilit Ghazaryan, Ernst-Bernhard Kley and Adriana Szeghalmi 131
- Mechanism of intramolecular multi-electron photochemistry in a 4H-imidazole Ruthenium dye
Linda Zedler, Stephan Kupfer, Sven Krieck, Rainer Beckert, Sven Rau, Michael Schmitt, Jürgen Popp and Benjamin Dietzek 137
- Dehydration of 3-octanol studied by 2D Raman, IR and NMR hetero correlation spectroscopy
Robby Fritzsich, Robert Geitner, Thomas W Bocklitz, Benjamin Dietzek, Micheal Schmitt and Jürgen Popp 157
- Isotopic effects in (surface enhanced) Raman spectroscopy – Single molecule aspects
Stephan Kupfer, Volker Deckert and Stefanie Gräfe 167
- Binary heavy metal bismuthate glass-ceramics with classical glass forming oxide
S Simon, M Muresan-Pop, C Leordean M Baia and L Baia 179
- Femtosecond time-resolved four-wave mixing spectroscopy of coupled electron-nuclear motion
Julian Albert and Volker Engel 189
- The accuracy of the M06L DFT method in the prediction of the vibrational Spectra of 4-amino-2-chlorobenzonitrile: A detailed interpretation of the Molecular Structure and vibrational IR and Raman spectra and other molecular properties using several DFT methods
M Alcolea Palafox, Anupama, Rachna Rastogi, M Jane Alam, Daisy Bhat, and V K Rastogi 199

Editorial

There are three very important occasions for me:

Firstly, it is a matter of great satisfaction and pride for me that *Asian J Phys* has most successfully completed 24 volumes since its inception in 1992 with the opening paper by **Prof Wolfgang Kiefer**, University of Wurzburg, Germany, and is now running in Volume 25 (2016). Secondly, Month of February is important being the month of discovery of **Raman Effect** on Feb 28, 1928 for which Raman was awarded *Nobel Prize* in 1930. And thirdly, Feb 2016 is the month of 75th birthday of Wolfgang Kiefer: A great Raman Spectroscopist. Many Happy Returns of the day Wolfgang.



During the period of long 24 years, we were able to release several special issues of AJP on different topics, including an special issue on Raman Spectroscopy by Wolfgang (Vol 7, No 2, 1998.) In his editorial Wolfgang writes, "This is an special issue of the Asian Journal of Physics which celebrates the seventieth anniversary of the discovery of the "Raman Effect" by Professor **Chandrasekhara Venkata Raman** at the Indian Association for the cultivation of Science, Kolkata, India. In the seventy years that have elapsed since the discovery of this new scattering phenomenon of a fundamental character, the field of Raman spectroscopy has grown enormously and continues to grow, encompassing a wide range of topics and applications in physics, chemistry, biology, biochemistry, medicine, pharmacy, environmental sciences and even in technology and art". This is still true - The range of applications of Raman Spectroscopy is very wide. Many applications of Raman Spectroscopy have been developed during the past decade.

Professor Wolfgang is not only well known among Raman Community for his outstanding contributions in the field of Raman Spectroscopy, but also known for his kindness and his willing support to many colleagues, Researchers and Students including me. I visited his laboratory in 2004 and 2006 and recorded several spectra, which resulted into a number of joint publications. He not only made numerous contributions in the fields of both linear and non-linear Raman spectroscopy but paved the way for new developments and insights into the exciting field of Raman Spectroscopy which is based on inelastic scattering of light. As mentioned by Guest Editors in Guest Editorial, the list of his contributions is very long and his work is being continuously cited in current literature.

During my stay in his Laboratory and his visits to Meerut, Trichi,.. Trivandram, I found that besides his academic interest Wolfgang is equally interested in the Social life also.

Please permit me to thank the Guest Editors Prof Juergen Popp and Dr Michael for editing this nice special issue of Asian J Phys, on the occasion of 75th Birth Day of Prof Wolfgang Kiefer. They have been able to collect 8 original articles to organize this special issue. I am happy to present this issue to Wolfgang and our readers.

Vinod Rastogi

Feb 12, 2016 (4:00 am)

Guest Editorial

An Appreciation to Wolfgang Kiefer on the occasion of his 75th birthday

Wolfgang Kiefer one of the most distinguished Raman spectroscopists will celebrate his 75th birthday on February 12, 2016. It gives us great pleasure to dedicate him on this occasion the 2nd issue of 25th Anniversary of Asian Journal of Physics (ISSN 0971-3093). This anniversary issue contains eight contributions by friends, colleagues and former students of Wolfgang Kiefer. The contributions nicely feature the broad range of Raman spectroscopic approaches and their broad applicability.

Wolfgang Kiefer worked throughout his impressive scientific career for the further development of Raman spectroscopy and its application towards new scientific fields. Raman spectroscopy fascinated Wolfgang Kiefer already as a diploma and Ph D student and was a solid companion throughout his scientific career. Wolfgang Kiefer developed and applied a great number of Raman approaches to unravel the structure of molecules in the gas, condensed and solid phase and on metal surfaces. In addition, the ultrafast dynamics taking place within and between these molecular systems took center stage of his scientific work.



Wolfgang Kiefer was born in 1941 in Pforzheim, Germany. He studied physics in Munich. After his PhD in 1970, he went for postgraduate studies to the National Research Council in Ottawa, Canada where he stayed for two years. He subsequently returned to Munich where he finished his habilitation in 1977. Between 1977 to 1984, Wolfgang Kiefer was a Professor in Bayreuth, Germany and from 1985 to 1988, he was appointed as full professor of Physics at the University of Graz, Austria. In 1988, he received a call for the chair for Physical Chemistry at the University of Wuerzburg, Germany, which he accepted. He stayed in Wuerzburg until his retirement in 2006. Wolfgang Kiefer graduated 85 PhD students among them are twelve who also successfully pursued an academic career as Professor. The Kiefer Raman labs were throughout his scientific career an extremely popular meeting place, hosting a large number of friends and colleagues as well as students of many different countries who always have enjoyed the fruitful and also pleasant stays in the Kiefer group.

It is impossible and would go much beyond this brief editorial to comprehensively summarize the scientific achievements of Wolfgang Kiefer, which are published in 865 (!) publications. In the following, just some key words of his groundbreaking research are listed:

- Resonance Raman spectroscopy and development of theories for resonance Raman spectroscopy
- Atomic Raman spectroscopy
- Raman and Mie scattering from micro-particles
- Development of special techniques for linear and nonlinear Raman spectroscopy (e.g. Raman difference spectroscopy with rotating cell, Raman matrix isolation spectroscopy)
- Raman spectroscopy on:
 - o Non-crystalline samples (e.g. glasses)
 - o Nanostructures
 - o Semiconductor quantum dots and quantum wires
 - o Biological and biochemical samples

- o Polymers
- o Etc.
- o Surface enhanced Raman spectroscopy (SERS)
- o Raman- and IR spectroscopy in combination with density functional theory calculations on metal complexes
- o Nanosecond coherent anti-Stokes Raman spectroscopy (CARS)
- o Femtosecond coherent four-wave mixing spectroscopy (degenerate four-wave mixing = DFWM, CARS):
 - Ultrafast ground- and excited state dynamics in gases and condensed phase
 - Coherent control of vibrations

The eight contributions of this special issue nicely reflect this list of topics and deal with SERS, resonance Raman, theoretical concepts to interpret Raman spectra, Raman spectroscopy on glasses, femtosecond four-wave mixing spectroscopy, Raman spectroscopy in combination with DFT calculations. These contributions nicely show how Wolfgang Kiefer's work inspired the authors and how he infected most of the senior authors with the "Raman gene".

Raman spectroscopy has matured to become one of the most important laser spectroscopic methods and has found its way into almost all natural sciences. Raman spectroscopy has become an indispensable analytical method for physics, chemistry, mineralogy and also recently for the life sciences and medicine. It is not exaggerated to say that the work of Wolfgang Kiefer significantly contributed to this success story of Raman spectroscopy. It is too bad, that the inventor of Raman spectroscopy the great Indian scientist CV Raman is not able to witness the scientific impact his invention had and more importantly will still have even after more than 80 years of its discovery. However, he would be definitely very proud of what his "Raman followers" like Wolfgang Kiefer achieved and how they utilized his invention.

It is no surprise and more than deserved that Wolfgang Kiefer was awarded with the Raman Lifetime Award on the XXIV. International Conference on Raman Spectroscopy (ICORS 2014) in Jena. Despite this latest award, Wolfgang Kiefer received several more prestigious awards. Here, we would only like to mention the Pittsburg Spectroscopy Award and an Honorary Doctor degree from the University of Cluj-Napoca, Romania.

Although Wolfgang Kiefer is celebrating his 75th birthday, he is still "infected by the virus Raman spectroscopy". In the basement of his house in the city of Eisingen he established a small but fine Raman lab he calls "Eisingen Laboratory for Applied Raman Spectroscopy" where he performs research work he always wanted to do but had no time for. Thus, for Wolfgang Kiefer Raman spectroscopy was not only his profession but also his hobby.

We hope that you will enjoy reading this 25th Anniversary of Asian Journal of Physics, which is dedicated to you.

Dear Wolfgang we wish you a happy 75th birthday and lots more exciting research results from your Eisingen Laboratory for Applied Raman Spectroscopy! But most importantly we wish you good health, long life and prosperity in the circle of your family!

Jürgen Popp and Michael Schmitt on behalf of all authors and the editorial board of AJP.

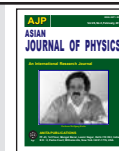
About the Guest Editors

Juergen Popp studied chemistry at the universities of Erlangen and Würzburg. After his Ph D in Chemistry he joined Yale University for postdoctoral work. He subsequently returned to Würzburg University where he finished his habilitation in 2002. Since 2002 he holds a chair for Physical Chemistry at the Friedrich-Schiller University Jena. Since 2006 he is also the scientific director of the Leibniz Institute of Photonic Technology, Jena. His research interests are mainly concerned with biophotonics. In particular his expertise in the development and application of innovative Raman techniques for biomedical diagnosis should be emphasized. He has published more than 750 journal papers and has been named as an inventor on 12 patents. He is Editor-in-Chief of the Journal of Biophotonics. In 2012, he received an honorary doctoral degree from Babeş-Bolyai University in Cluj-Napoca, Romania. Professor Jürgen Popp is the recipient of several awards, including, the 2013 Robert Kellner Lecture Award and the prestigious 2016 Pittsburgh Spectroscopy Award. In 2016 he was elected to the American Institute for Medical and Biological Engineering (AIMBE) College of Fellows. He is Member of Editorial Board of Asian J Phys.



Michael Schmitt received his Ph.D. in chemistry from the University of Würzburg in 1998. From 1999 to 2000 he went for postgraduate studies to the Steacie Institute for Molecular Sciences at the National Research Council of Canada. He subsequently joined the group of Prof. Kiefer at the University of Würzburg, where he finished his habilitation in 2004. Since March 2004 he has been a research associate in the group of Prof. Jürgen Popp at the Institute for Physical Chemistry at the Friedrich-Schiller-Universität Jena. His main research interests are focused on non-linear spectroscopy for biomedical and material research. He has published more than 200 journal papers and is Assistant Editor of the Journal of Biophotonics.





Two dimensional graphene derivatives supported isolated gold nanoparticles as an efficient SERS substrate

Shiju Abraham^{a,b}, Matthias König^b, Shobhit Pandey^c, Sunil K Srivastava^d,
Bernd Walkenfort^b and Anchal Srivastava^a

^aDepartment of Physics, Banaras Hindu University, Varanasi, 221005, India

^bFaculty of Chemistry, University of Duisburg, 45141 Essen, Germany

^cMetallurgical Engineering Department, Indian Institute of Technology – (BHU), Varanasi

^dDepartment of Pure and Applied Physics, Guru Ghasidas University, Bilaspur, 495 009, India

(Dedicated to Professor Wolfgang Kiefer on the occasion of his 75th birthday)

The present work accomplishes surface enhanced Raman scattering (SERS) studies using the combination of stable, diluted and isolated gold nanoparticles (Au NPs) of tailored size (~ 50 nm) and distribution on two dimensional carbon nanostructures (2D-CNS) i.e. graphene oxide (GO) and reduced graphene Oxide (RGO). Fabricated using a simple, quick and cost effective method, these SERS substrates have enough synergistic enhancement from each Au NPs and underlying CNS matrix with sensitivity enough to easily detect 10^{-6} molar concentrations of analyte, 4-mercaptobenzoic acid (4-MBA). Further, uniform distribution of Au NPs ensures great reproducibility showing potential for standardization in future. © Anita Publications. All rights reserved.

Keywords: Surface enhanced Raman scattering (SERS), Nanoparticles, Graphene oxide (GO), 4-mercaptobenzoic acid (4-MBA)

1 Introduction

Surface-enhanced Raman scattering (SERS) is a surface selective and highly sensitive spectroscopic technique for molecular detection and surface analysis [1,2]. SERS offers higher magnitude of increased intensity and suppresses the fluorescence signal while selectively enhancing the Raman signal, and produces chemical fingerprinting with sensitivity enough to enable single-molecule detection [3]. The two widely accepted enhancement mechanisms are the dominant electromagnetic mechanism (EM) and the chemical mechanism (CM) which contributes only about one or two orders to the enhancement together contributing the overall enhancement [4]. The long range nature of EM relies on the roughness, high curves or gapped metal regions of the substrate in order to develop localized electromagnetic field regions called as “hot” spots. In this respect, rough noble metal nanoparticles substrates, especially Au NPs having good curvature and required optical properties for enhanced surface plasmons on excitation, proved out to be one of the most popular traditional SERS substrates with additional advantages such as biocompatibility, stability, controllable size and shape distributions [5,6]. Mostly, due to complex distribution of molecules on SERS substrate, molecules near the hot spots keep on fluctuating, which is further aggravated by other factors like chemical interactions between the molecules and the metal substrate, chemical adsorption-induced vibrations, molecular deformation and distortion, etc. [7,8]. These disadvantages demand new materials for SERS substrates, which can be fabricated uniformly and economically with particles size small enough that an isolated particle can give the required localized surface plasmon resonance effect.

Corresponding author :

e-mail: anchalbhu@gmail.com, phone: +91 9453203122 (Anchal Srivastava)

Often termed as a “first layer effect”; unlike EM, CM is a short range effect which requires the distance between the molecule and the substrate to be below 0.2 nm. Further, the charge transfer between molecule and substrate is possible by having the Fermi level of the metal substrate symmetrically aligned with the highest occupied molecular orbital (HOMO) and lowest unoccupied molecular orbital (LUMO) of the molecule [1,9]. These requirements mark the inefficiency of CM in case of noble nanoparticles based SERS substrates, but paved the way for graphene substrates based SERS; called now as Graphene Enhanced Raman Spectroscopy (GERS). In case of graphene, relatively smooth surface, visible range optical transitions [10], and lower surface plasmon [11] make EM ineffective, making CM as the dominant mechanism. However, unlike metal substrates, the Raman enhancements are limited and not enough for standardization [12]. Nevertheless, flexibility offered by graphene and its derivatives and particularly their ability to combine with metal nanoparticles attests its potential as a promising matrix for forming hybrids [13] which can take advantage of both EM and synergistically enhanced CM, for an overall commendable Raman enhancement; the prime motivation of the present work.

With this aim, the present work utilizes Au NPs supported 2D-CNS matrix, as a commendable SERS substrate for testing the efficacy of the Raman Marker; 4-MBA. Finally, in order to produce reproducibility enabling future standardization, the present work uses the enhancement upraised from isolated Au NPs of tailored size decorated at distances higher than the spectral resolution of the exciting source, still producing commendable enhancements without any signal degradation; enough for detecting smallest of the concentrations (10^{-6} M) of the Raman marker.

2 Experimental

Typically the 2D- CNS used here (GO and RGO) were produced using the earlier reports [14,15] (supplementary information). Further to produce non agglomerating Au NPs with tailored size, seeded-growth method proposed by Perrault *et al* was followed [16] (Supplementary information). However, in order to maximize the localized surface plasmon resonance (LSPR) effect for maximum enhancement from each Au NPs, the size was then tailored to 50 nm while simultaneously stabilizing with, polyvinylpyrrolidone (PVP).

The 2D- CNS- Au nanoparticles composites were prepared by simply adding 300 μ L of diluted spherical Au NPs into 700 μ l of 2 mg/mL (in distilled water) dispersion of 2D- CNS, succeeded by sonication and storage in vibration stand until thin film formation (supplementary information). These two composites i.e RGO- Au NP and GO- Au NP were then uniformly spin coated covering entire 5×5 mm² silicon substrate to form the SERS substrate on which 5 μ L of Raman marker solution of 4-MBA (1 μ M) was then incubated for overnight at room temperature.

3 Results and Discussion

The transmission electron microscopy (TEM) image shown in Fig 1 manifests the homogenously stabilized Au NPs, which were well separated and spherical in shape (\sim 50 nm). Figure 2(a) shows the TEM image of GO sheets, which is non-contaminated, continuous and few layered in nature. Figure 2 (b) corresponding to TEM of GO-Au NPs, clearly shows a single Au NP is decorated on $\sim(2 \times 2)$ μ m² area. The Au NPs have required shape (spherical) and size (50 nm) for effective Raman enhancement effect, while the distribution is such that, the distance between Au NPs exceeds the spectral resolution of the laser, enabling isolated particles enhancement. Figure 2(c) shows the TEM image of few layered RGO sheets of long lateral uniformity like GO. Similarly RGO-Au NPs shown in Fig 2(d) denotes the isolated Au NP distribution on the RGO surfaces as in case of GO.

In order to check the reproducibility and potential to be used as a standardized SERS substrate in future, the work involves Raman mapping (using confocal Raman microscope of WITec Alpha 300R,632.8

nm laser line) of $(100 \times 100) \mu\text{m}^2$ area on substrate scanned with an interval of $2 \mu\text{m}$ with an integration time of 1 second. Figure 3 represents a simplified schematic of the SERS substrate and the SERS signal enhancement obtained.

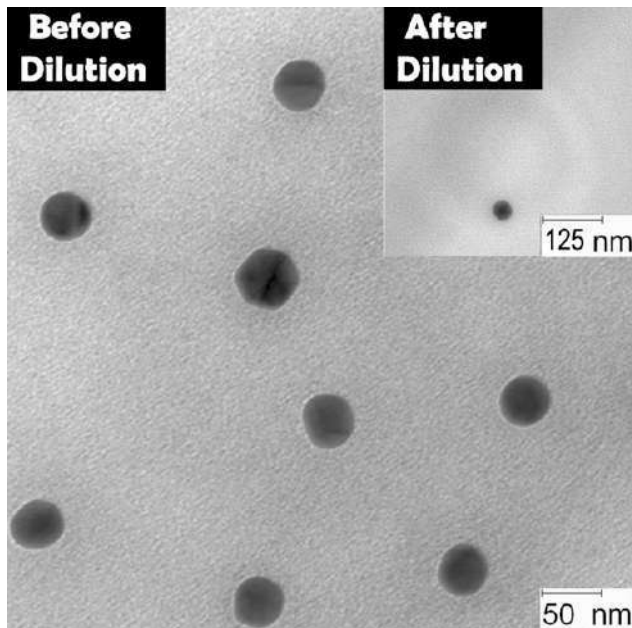


Fig 1. TEM Image of Au NPs; on inset, isolated Au N

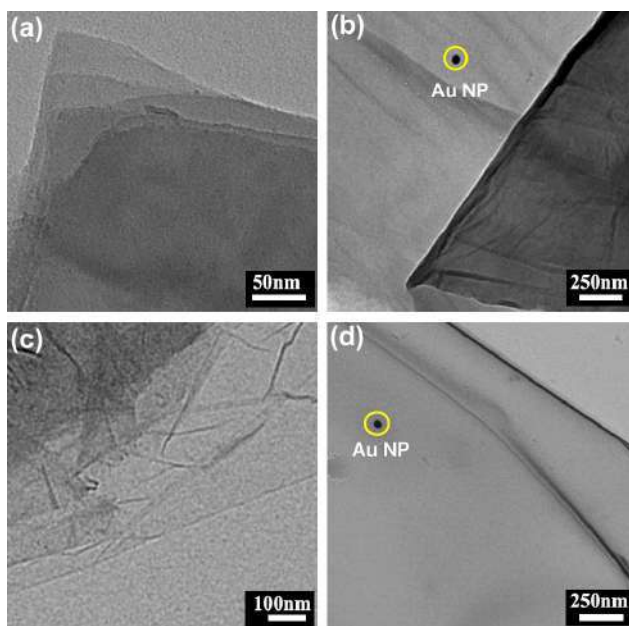


Fig 2. TEM Images of (a) Few layered GO, (b) GO-Au NPs (c) Few layered RGO, (d) RGO-Au NPs

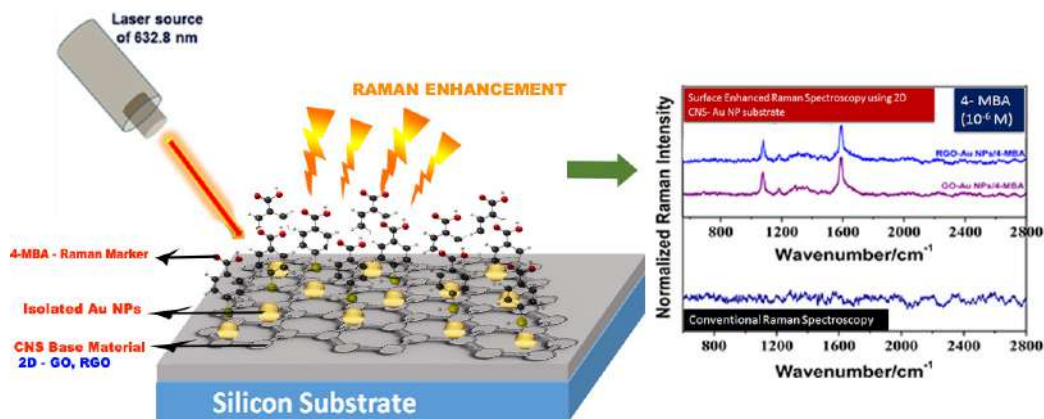


Fig 3. Schematic illustrating the SERS substrate and the Raman enhancement obtained

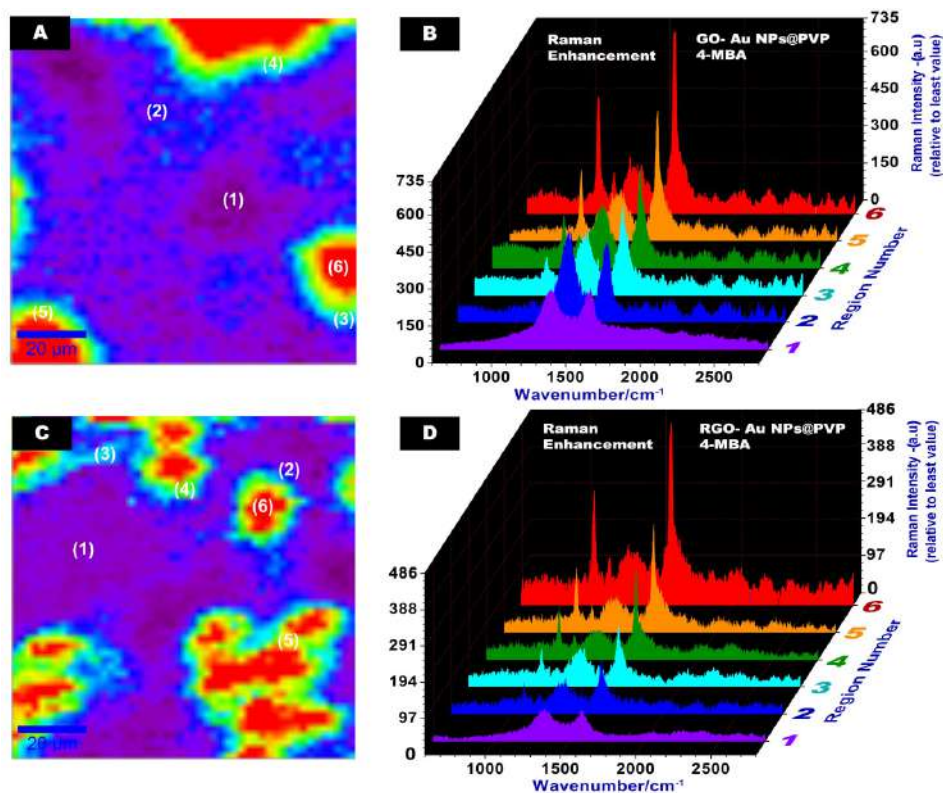


Fig 4. (a) Raman mapping image of GO-Au NPs-4-MBA; (b) Corresponding six point's 3D-SERS spectra. (c) The Raman mapping image RGO-Au NPs-4-MBA, (d) 3D- SERS spectra of RGO-Au NPs-4-MBA.

Raman imaging of GO-Au NPs- 4-MBA defined for the peak centered at 1585 cm^{-1} through the intensity color profile is shown in Fig 4 (a). The well-defined colored region is a profile for the prominent 4-MBA band centered $\sim 1585\text{ cm}^{-1}$ ($\nu(\text{CC})$ ring stretching). In the color profile, the intensity increases from violet to red. Evidently, the center part of the substrate is more or less occupied with violet and blue color, indicating its more GO nature rather than GO-Au NPs. So the maximum intensity (red color) region

indicates the maximum probable place where Au NPs were decorated and are bonded towards 4-MBA. This findings can be confirmed by the corresponding Raman spectrum of the six different regions (violet to red) (Fig 4 (b)). From the cyan to red color (marked 3 to 6), the corresponding Raman spectrum gives well defined peaks of the Raman marker 4-MBA at 1585, 1175, 1070 and 1340 cm^{-1} even for the low concentration (1 μM) and amount of Raman reporter molecule, attesting substantial Raman enhancement. Also a low profile D ($\sim 1350 \text{ cm}^{-1}$) and G-Band ($\sim 1580 \text{ cm}^{-1}$) of GO can be observed on the same spectrum. But in region 1 and 2, the D and G-Band are more prominent due to the CNS base material contribution. Figure 4 (c) represents the Raman mapping image of RGO-Au NPs-4-MBA and the 4-MBA field is more nicely distributed here (red region). In the corresponding Raman spectra (Fig 4(d)), a more defined 4-MBA characteristics peak can be observed throughout the region 2 to 5. So, both SERS substrates are observed to be good base materials utilizing both the EM and synergistically enhanced CM, to detect effectively and quickly even the very low concentration of Raman reporter molecule (1 μM), which is impossible to detect using normal RS [17].

4 Conclusions

The present work introduces a simple and quick chemical method to fabricate highly efficient SERS substrates based on Au NPs and 2D-CNS (graphene derivatives) combination. The proposed substrates have commendable Raman enhancement, taking the advantage of both; i.e. EM from the Au NPs and synergistically enhanced CM from Au NP decorated GO/RGO matrix. The tailored Au NPs have a size of 50 nm to ensure maximum enhancement at the used excitation source (632.5 nm). Further, their distribution is such that the distance between the nanoparticles is greater than the spectral resolution of the excitation source. These factors enable enhancement which is enough to detect 10^{-6} M concentrations of analyte with appreciable sensitivity. Further, the uniform distribution and isolated particle dependence for enhancement, cuts down the ambiguity of variations in hot spot regions, thereby powering these substrates with great reproducibility; suggesting great potential for standardization in future.

Acknowledgments

SA and SKS is thankful to Alexander von Humboldt for supporting this research work through AvH Research Group Linkage Program. AS acknowledges CAS program sponsored by UGC at Department of Physics, B. H. U and DST project (No.:DST/TSG/PT/2012/68), New Delhi, India for financial assistance.

References

1. Campion A, Kambhampati P, *Chem Soc Rev*, 27(1998)241-250.
2. Schlücker S, *Angew Chemie Int Ed*, 53(2014)4756-4795.
3. Nie S, Emory S R, *Science*, 275(1997)1102-1106.
4. Lin C -C, Yang Y -M, Chen Y -F, Yang T -S, Chang H -C, *Biosens Bioelectron*, 24(2008)178-183.
5. Talley C E, Jackson J B, Oubre C, Grady N K, Hollars C W, Lane S M, Huser T R, Nordlander P, Halas N J, *Nano Lett*, 5(2005)1569-1574.
6. Song J, Cheng S, Li H, Guo H, Xu S, Xu W, *Mater Lett*, 135(2014)214-217.
7. Le Ru E, Etchegoin P, *Principles of Surface-Enhanced Raman Spectroscopy: And Related Plasmonic Effects*, (Elsevier), 2008.
8. Li J F, Huang Y F, Ding Y, Yang Z L, Li S B, Zhou X S, Fan F R, Zhang W, Zhou Z Y, Wu D Y, *Nature*, 464 (2010)392-395.
9. Otto A, *J Raman Spectrosc*, 36(2005)497-509.
10. Bruna M, Borini S, *Appl Phys Lett*, 94(2009)31901; doi:org/10.1063/1.3073717.
11. Rana F, *Nanotechnology; IEEE Trans*, 7(2008)91-99.
12. Ling X, Wu J, Xie L, Zhang J, *J Phys Chem C*, 117(2013)2369-2376.

13. Khorasaninejad M, Raeis-Zadeh S M, Jafarlou S, Wesolowski M J, Daley C R, Flannery J B, Forrest J, Safavi-Naeini S, Saini S S, *Sci Rep*, 3(2013) 02936;doi: 10.1038/srep02936.
14. Marcano D C, Kosynkin D V, Berlin J M, Sinitskii A, Sun Z, Slesarev A, Alemany L B, Lu W, Tour J M, *ACS Nano*, 4 (2010)4806-4814.
15. Li D, Müller M B, Gilje S, Kaner R B, Wallace G G, *Nat Nanotechnol*, 3(2008)101-105.
16. Perrault S D, Chan W C W, *J Am Chem Soc*, 131(2009)17042-17043.
17. Hsieh C -W, Lin P -Y, Hsieh S, *J Nanophotonics*, 6 (2012)63501-63506.

[Received: 30.9.2015; accepted: 15.10.2015]

Supplementary Materials

Two dimensional graphene derivatives supported isolated gold nanoparticles as an efficient SERS substrate

Shiju Abraham^{a,b}, Matthias König^b, Shobhit Pandey^c, Sunil K Srivastava^d,
Bernd Walkenfort^b and Anchal Srivastava^a

^aDepartment of Physics, Banaras Hindu University, Varanasi, 221005, India

^bFaculty of Chemistry, University of Duisburg, 45141 Essen, Germany

^cMetallurgical Engineering Department, Indian Institute of Technology – (BHU), Varanasi-221 005, India

^dDepartment of Pure and Applied Physics, Guru Ghasidas University, Bilaspur- 495 009, India

1 Experimental

1.1 Materials

Graphite flakes (NGS Naturgraphit GmbH, Germany), tetrachloroauric acid (HAuCl₄), polyvinylpyrrolidone (PVP), Sodium Citrate, hydroquinone, 4-MBA, H₂SO₄, H₃PO₄, KMnO₄, H₂O₂, hydrazine hydrate, Ammonia solution, ethanol, etc. used were of technical grade and were procured from Sigma-Aldrich.

1.2 Preparation of Graphene Oxide (GO)

The protocol proposed by Marcano *et al* [1] has been applied for the synthesis of GO. Briefly, a 9: 1 combination of concentrated H₂SO₄: H₃PO₄ was added to 2g of graphite flakes and 12g of KMnO₄. At a temperature of 50° C, the mixture was stirred for 12 h. The reaction was quenched after the mixture was cooled to room temperature (RT) by adding ~260 mL of ice with 2 mL of 30% H₂O₂. This mixture was then shifted, filtered and was washed with distilled water and 30% HCl. The final product obtained (GO) was then dried at 70°C.

1.3 Preparation of Reduced Graphene Oxide (RGO)

Chemical conversion of GO to RGO is achieved by following the method proposed by Dan Li *et al* [2]. Briefly, a 500 mL (0.25mg/mL) GO dispersion in distilled water was kept for ultra-sonication for 20 minutes to obtain a light yellowish dispersion. A pH ≈ 10 is achieved for this GO dispersion by adding ~2 mL of ammonia solution (25%). Further, 400 μL of hydrazine hydrate solution (H₂N₂O) was added and the solution was kept under ultra-sonication at a temperature of 80°C for two hours. Successively, the solution stirred at 95°C for 12 hrs to continue the reduction reaction process and the solution turns black in color. This solution is then filtered, washed and dried at 80°C to collect the RGO.

1. 4 Preparation of Gold Nanoparticles (Au NPs) and the stabilization with PVP

Gold nanoparticles (Au NPs) were synthesized following seeded-growth method by Perrault *et al* [3]. Briefly 50 ml ultrapure water was heated under reflux. While boiling 300 μL gold(III) chloride solution (1 wt. %) was added followed by 900 μL sodium citrate solution (1 wt. %) after 2 min of stirring. The solution is boiled for additional 2 min and cooled at room temperature. The color changed to red during the reaction.

The obtained seed Au NPs have a diameter of 20 nm. In a second step these seed particles were grown bigger to Au NPs stabilized by polyvinylpyrrolidone (PVP). Therefore 250 mL ultrapure water, 10 mL of the before prepared seed solution, 2.5 mL gold(III) chloride solution (1 wt. %) and 2.5 g PVP were mixed in a Erlenmeyer flask. After the addition of 5 mL 0.03 M hydroquinone solution, the colloid is stirred for one day at room temperature. The obtained Au NPs have a diameter of 50nm.

1.5 Preparation of 2D-CNS-Au NPs composites

Both 2-Dimensional CNS materials (graphene derivatives GO and RGO) were taken at a concentration of 2 mg/mL in DW in separate vials. These dispersions were sonicated for 30 minutes to make a homogeneous dispersion. From the well dispersed CNS solution, 700 μL taken out in a 2 mL Eppendorf and added 300 μL of diluted spherical Au NPs of ~ 50 nm size. This was further sonicated for 10 minutes and kept in a vibrating stand until the thin film formation.

1.6 Fabrication of CNS, CNS-4-MBA and CNS-Au NPs-4-MBA thin film electrodes on Si-substrate

For fabricating a thin film of CNS and CNS-Au NPs on silicon (Si) substrate, all the silicon substrates were well cleaned by the standard protocol. On this Si substrate of $5\text{ mm} \times 5\text{ mm}$ dimensions, the CNS/ CNS-Au NPs were spin coated separately using 10 μL of hybrid solution. These substrates were dried at a temperature of $70\text{ }^\circ\text{C}$. On these CNS/ CNS-Au NPs substrates, 5 μL of Raman marker solution of 4-MBA (1 μM) were incubated for overnight at room temperature. These CNS-4-MBA and CNS-Au NPs- 4-MBA were further used for to conduct the SERS experiments.

2 Characterization of the materials

The structural characterization of GO and RGO, were characterized by X-ray diffraction (XRD) technique (Rigaku miniflex-II diffractometer at 30 kV, 15mA). The wavelength of Cu-K α 1 radiation of $\lambda = 1.5405\text{ \AA}$ was used for obtaining the XRD pattern. TEM images were obtained using a Zeiss EM 902 instrument. The SERS measurements through Raman mapping experiments were conducted with a confocal Raman microscope (WITec Alpha 300R, 30 cm focal length and 600 grooves per mm grating spectrometer) equipped with an EM-CCD. A 632.8 nm line from a He-Ne laser was focused onto the sample using a 40 \times objective (Olympus) with a numerical aperture of 0.6 (5 mW laser power at the sample). For the Raman mapping, an area of $(100 \times 100)\text{ }\mu\text{m}^2$ is scanned with an interval of $2\text{ }\mu\text{m}$ with an integration time of 1s.

3 UV-V is absorption studies

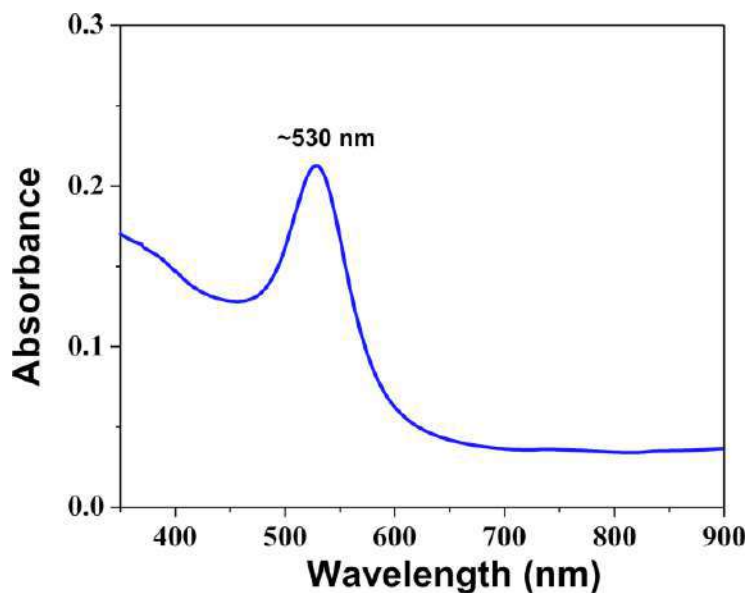


Fig S1. UV-vis absorption spectra of PVP stabilized Au NPs

Figure S1 shows the typical absorption UV-V is spectrum of the PVP stabilized Au NPs in distilled water. The absorption peak due to the surface plasmon resonance of Au NPs is centered on 530 nm which is more red shifted in nature comparing to nanoparticles of lesser particle size.

4 XRD studies of 2D-CNS base materials

The XRD pattern of the as-synthesized 2D CNS base materials, namely GO and RGO are presented in Fig S2. GO shows a strong diffraction peak at $\sim 11^\circ$ (Fig S2a), which corresponds to the (002) reflection plane with a d-spacing of 8.0 Å [1].

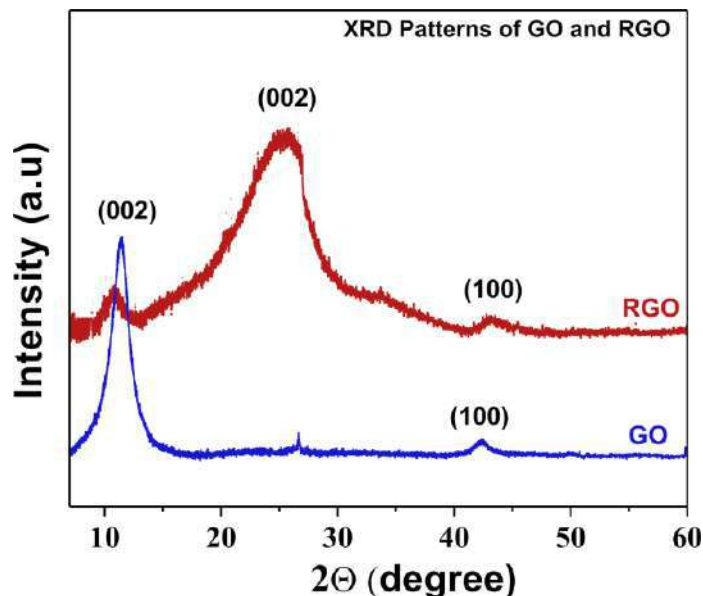


Fig S2. XRD Patterns of GO and RGO

The weak and broad band around 42° corresponding to the (100) reflection is due to the turbo static band of disordered carbon material. The most prominent diffraction peak of RGO is observed at $\sim 24.5^\circ$ (002) attesting the characteristic band of RGO (Fig S2b) with an interlayer spacing of 3.4 Å. This value matches with the well-known XRD peak of RGO [4].

5 Raman Spectra of 2D-CNS Base Materials and 2D-CNS+4-MBA

Figure S3 displays the Raman spectrum of 2D- CNS base materials (GO and RGO) which were spin coated on the Si-substrate. In Fig S3 (a) and (c), clearly shown the characteristic D and G bands centered around 1340 and 1580 cm^{-1} can be observed. The broad nature of D-band (disorder band) observed for both GO and RGO is due to their different functional groups and sp^3 hybridization present in these materials. Figure S3 (b) and (d) represent individual Raman spectrum of 2D CNS base materials, GO and RGO, respectively, which were immobilized with $1\ \mu\text{M}$ of 4-MBA. The results attest GO and RGO both as SERS substrates due to the CM effect (as in GERS) these graphene derivatives can offer; although the enhancement as expected (due to only CM contribution) is not substantial. Clearly, the G- band becomes sharper in nature due to the main Raman peak of 4-MBA centered around 1585 cm^{-1} , which is due to the $\nu(\text{CC})$ ring stretching coinciding at the same position. The same sharp peak profiles for the spectra can be noticed in case of the D-bands.

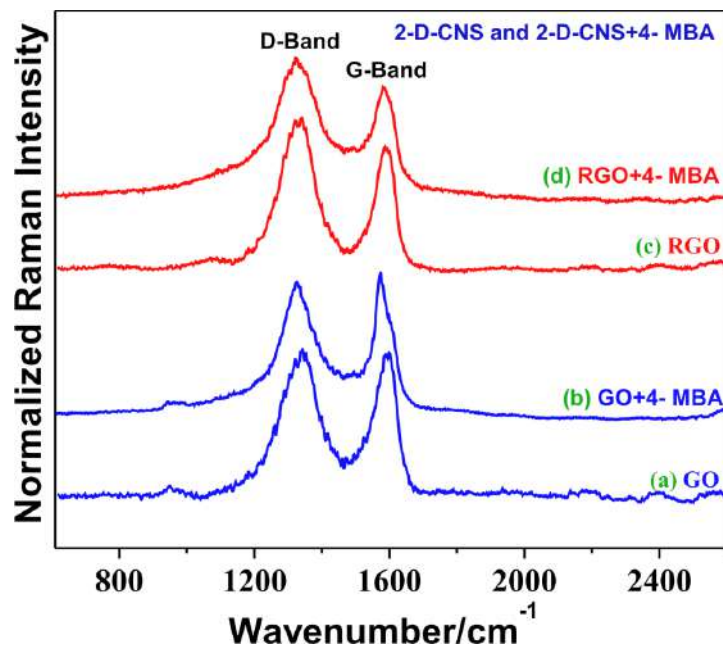
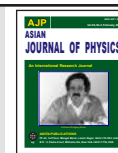


Fig S3. Normalized Raman spectra of (a) GO on Si-substrate where prominent D, G bands of CNS are marked; (b) GO base materials immobilized with Raman marker 4-MBA (5 μ L, 1 μ M); (c) RGO on Si-substrate, (d) RGO base materials immobilized with Raman marker 4-MBA (5 μ L, 1 μ M)

References

1. Marcano D C, Kosynkin D V, Berlin J M, Sinitskii A, Sun Z, Slesarev A, Alemany L B, Lu W, Tour J M, *ACS Nano*, 4(2010)4806-4814.
2. Li D, Müller M B, Gilje S, Kaner R B, Wallace G G, *Nat Nanotechnol*, 3(2008)101-105.
3. Perrault S D, Chan W C W, *J Am Chem Soc*, 131(2009)17042-1743.
4. Park S, An J, Potts J R, Velamakanni A, Murali S, Ruoff R S, *Carbon*, 49(2011)3019-3023.



Encapsulation of optical gratings using nanoporous alumina layers

Lilit Ghazaryan, Ernst-Bernhard Kley, and Adriana Szeghalmi

*Institute of Applied Physics, Abbe Center of Photonics, Friedrich-Schiller University Jena,
Max-Wien-Platz 1, 07743 Jena, Germany*

(Dedicated to Professor Wolfgang Kiefer on the occasion of his 75th birthday)

In this work, we describe a method to encapsulate optical gratings with nanoporous Al_2O_3 . The encapsulation process consists of covering a grating, filled with a sacrificial material, by an organic-inorganic thin alucone layer. The element is then heated up to 400°C to remove the organic component from the alucone film. The nanoporous Al_2O_3 film, formed after the removal of the organic component acts as a diffusion layer for the decomposition products of the sacrificial material. The complete removal of the sacrificial material was confirmed by energy dispersive x-ray spectroscopy (EDX).

© Anita Publications. All rights reserved.

Keywords: Optical gratings, Energy dispersive x-ray spectroscopy (EDX).

1 Introduction

Diffraction gratings are essential components in optical systems to manipulate the propagation of light. Generally, periodically nanostructured elements are used to diffract the light. The function of the gratings is highly dependent on the material of the element, on the period, the width and the depth of the nanostructures as well as on the wavelength of the incident light [1]. Depending on the mentioned parameters, the diffraction gratings are widely used in monochromators, spectrometers, laser systems, etc. [2-5].

Even though optical gratings highly enhance the performance of optical systems, they have a main drawback of being mechanically not as stable as unstructured optical elements. Moreover, the grating structures are sensitive to contaminations (such as organic rests or particles), which in contrary to e.g. thin film coatings cannot be cleaned or removed due to the high aspect ratio of the surface. The contamination or damage of the nanostructures strongly deteriorates the optical function of the optical elements with time.

To protect the nanostructures against environmental influences, different encapsulation methods were proposed. Nishii *et al* covered binary gratings with thin SiO_2 layers by plasma enhanced chemical vapor deposition (PECVD) at 400°C substrate temperature [6]. However, the PECVD deposition partially fills the upper part of the grooves, which in turn can highly reduce the efficiency of the element. Direct bonding is another method which was applied to protect nanostructures [7,8]. In this case, the structured wafer and an unstructured wafer of the same material are directly bonded under compressive pressure. In order the encapsulation through direct bonding to be successful, both surfaces must be highly clean and very smooth. The bonding process is very challenging and time consuming, since any small defect, contamination or differences in the height profile of the structures will strongly disturb the optical function.

Recently, Ratzsch *et al* proposed a new encapsulation process based on the selective removal of a sacrificial material by wet chemical etching [9]. The encapsulation was realized by first filling the gratings with a sacrificial material. Afterwards, the excess material on top of the grating was removed and a thin SiO_2 cover layer was deposited using atomic layer deposition (ALD). Narrow grooves were created in the cover

Corresponding author :

e-mail: a.szeghalmi@uni-jena.de; Fax/phone: ++49 3641 947 802/859 (Adriana Szeghalmi)

layer to remove the sacrificial material. At the last stage, the sacrificial material was removed by selective chemical etching in phosphoric acid solution. The drawback of this method is the necessity to pattern the top SiO_2 layer by complex etching techniques even though the period of the upper grooves is several hundreds of nanometer.

In this work, we have deposited hybrid organic/inorganic alucone alloys using atomic layer deposition (ALD) and molecular layer deposition (MLD). Calcination of these alloys at elevated temperatures leads to the formation of nanoporous Al_2O_3 . The nanoporous Al_2O_3 was used as diffusion layer to encapsulate optical gratings. The gratings were first filled with a sacrificial material (polymer resist) and covered by a thin alucone layer. Afterwards, the sacrificial material was completely removed by heating up to 400°C . Hence, the grating structure is finally protected by a thin capping layer of Al_2O_3 that can be further reinforced by standard physical vapor deposition techniques.

2 Experimental methods

2.1 Atomic layer deposition (ALD) and molecular layer deposition (MLD)

Atomic layer deposition (ALD) is a powerful thin film coating technique allowing to precisely control the film thickness of inorganic coatings based on sequential self-limiting surface reactions [10,11]. Similar to ALD, molecular layer deposition (MLD) enables growing completely organic or organic-inorganic hybrid polymer thin films typically using bi- or multifunctional monomers [12,13]. One class of such hybrid polymers are alucones which are grown with MLD using trimethylaluminium (TMA) as inorganic and ethylene glycol (EG) as organic constituent (Fig 1) [14]. By changing the number of MLD cycles, alucone thin films with desired film thickness can be deposited.

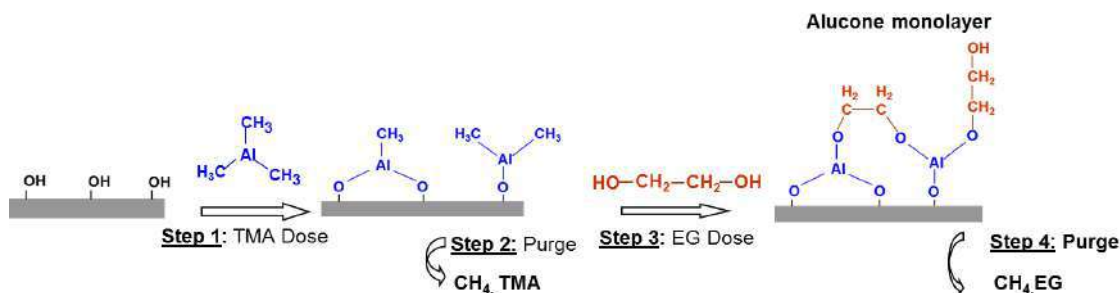


Fig 1. Schematic view of 1

The Oxford Instruments Opal ALD open load system equipped with three precursors and a separate H_2O input was used for these experiments. The alucone alloy films were deposited using alternating sequences of TMA/ H_2O for ALD Al_2O_3 and TMA/EG for MLD alucone. The Al_2O_3 was deposited using 10 ms TMA dose and 30 ms H_2O with 7s purge times between each precursor dose. The alucone MLD films were deposited with 10 ms dose and 7 s of purge times for TMA and 2s EG dose with subsequent purge of 15s. After the EG purge, 10s of the chamber purge was done to make sure that the whole unreacted EG molecules get out of the reaction chamber before the next TMA dose entry. All depositions were done at 150°C substrate temperature.

2.2 Characterization techniques

The thickness and the refractive index of the films were obtained by *ex situ* spectroscopic ellipsometry (J A Woollam Co., Inc.) in the spectral range of 250–1700 nm. The experimental data were analyzed with Complete EASE software provided with the equipment. The measured data of the dense film was fitted to a Cauchy function and of the nanoporous films to effective medium approximation (EMA). For the nanoporous samples the fit was done from 400 nm to get an improved fit.

Scanning electron microscopy (SEM) images and energy dispersive X-ray analysis (EDX) for chemical characterization were recorded with ultra-high resolution Hitachi High-Technologies (Hitachi S-4800) scanning electron microscope. The scanning time of the sample during EDX analysis was 5 minutes.

Neon 60 Cross Beam focused ion beam scanning electron microscopy (FIB-SEM) was used to get the cross-sectional micrographs of the encapsulated grating.

2.3 Encapsulation process

To encapsulate optical gratings with nanoporous Al_2O_3 , a manufacturing process was developed consisting of 4 steps. The schematic view of the encapsulation of the gratings using MLD/ALD alucone alloy layers is shown in Fig 2.

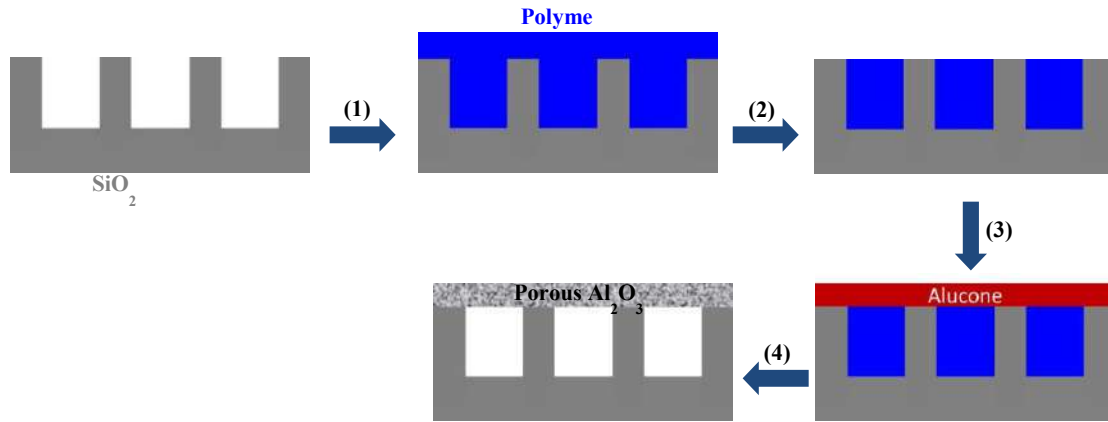


Fig 2. Schematics of the encapsulation process. (1) Spin coating of a polymer sacrificial layer, (2) planarization, (3) deposition of MLD/ALD alucone alloy layer, (4) removal of the sacrificial layer by annealing.

In the first step (1) the grating was filled with a sacrificial material by spin coating. As a sacrificial material, an organic polymer material was chosen (resist AZ1505), which is unstable at high temperatures. This ensures that during heating the sacrificial material will completely decompose and will be easily removed from the grooves. The spin coated polymer does not only fill the grooves but also covers the grating bars. Therefore, in the step (2) the excess amount of the material from the top of the grating is removed. This was done by reactive ion beam etching (RIBE) using Ar^+ ions. Afterwards, (step (3)) the deposition of thin alucone alloy layer on the planarized surface by MLD/ALD was carried out. To ensure a better stability of the cover layer, 1 cycles of ALD Al_2O_3 was inserted after every 5 cycles of MLD alucone deposition. In the last step, the element is heated up to $400\text{ }^\circ\text{C}$ to remove the organic constituents from the alucone layer and the sacrificial material from the grooves.

3 Results and Discussion

In recent years, nanoporous Al_2O_3 was produced by heating MLD alucone layers at elevated temperatures [15,16]. These layers were used as diffusion layers to develop highly efficient composite membranes for H_2 separation [17] and for producing Cu oxide nanoparticles [18,19]. Moreover, due to the porosity, the layers were shown to have much lower refractive index than the refractive index of the compact layers [20]. Nanoporous Al_2O_3 layers with a refractive index of 1.34 were realized. Here, we apply these nanoporous thin films as diffusion layers to encapsulate conventional binary gratings.

Following the scheme shown in Fig 2, we encapsulated binary SiO₂ grating with a period, groove width and groove depth of 400 nm, 300 nm and 850 nm, respectively. After spin coating of the sacrificial polymer and subsequent removal of the excess material, 85 nm alucone/Al₂O₃ layer was deposited by MLD/ALD. Afterwards, the element was heated from room temperature up to 400 °C at the rate of 10 °C/min and left at this temperature for 45 h. Figures 3(a) and (b) show a top and cross-sectional view of the encapsulated grating, respectively.

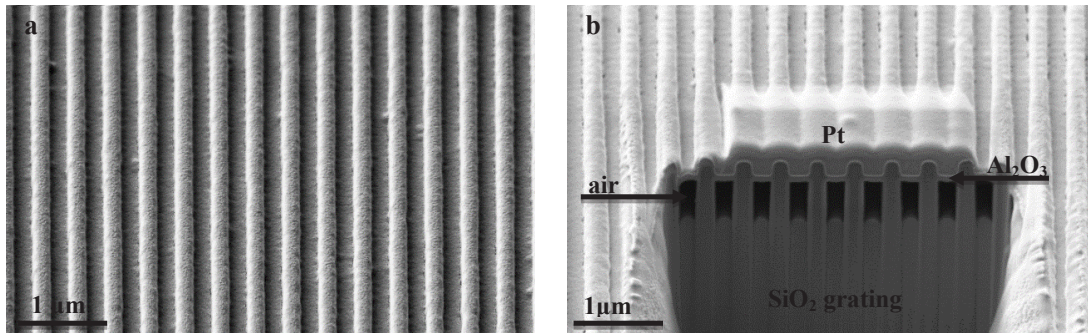


Fig 3. Focused ion beam scanning electron microscopy (FIB-SEM) micrographs of the binary SiO₂ grating encapsulated with nanoporous Al₂O₃, (a) top and (b) cross-sectional view.

As a result of the heat treatment, the organic part of the alucone layer was decomposed and removed leaving nanoporous Al₂O₃ thin layer as a cover layer. Simultaneously, the sacrificial polymer material also decomposes to volatile gasses (CO₂ and H₂O mainly), which then diffuse through the porous Al₂O₃ layer. As it can be seen from the top view image in Fig 3a, the removal of the organic components does not destroy the cover Al₂O₃ layer, if the alucone film is thick enough. If the capping layer was deposited with 36 nm alloy thickness, instead of 85 nm, the cover layer was not stable any more but showed cracks all over the surface. The encapsulation was also not possible, if the alucone deposition was carried out directly on top of the sacrificial layer, before removing the excess material. This could be caused by a very high pressure which arises due to the decomposition of the excess polymer amount compared to the amount of the polymer in the grooves. The sinking on the top is due to the shrinkage or partial removal of the sacrificial AZ layer during ALD/MLD deposition. This can be improved by choosing another polymer material as sacrificial layer, which is insensitive to the ALD/MLD processes.

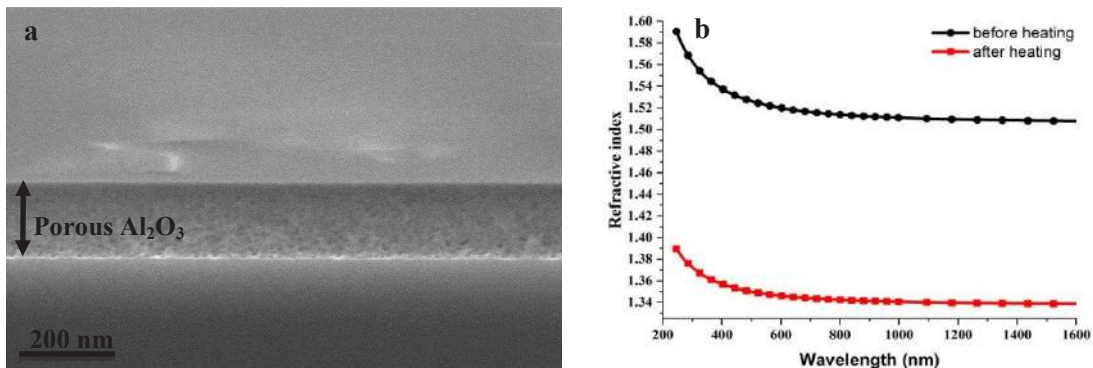


Fig 4(a). The SEM cross-sectional view of the alucone layer after heat treatment, (b). the effective refractive index spectra of alucone alloy layer before and after heat treatment.

To record a good cross-sectional image by focused ion beam scanning electron microscopy (FIB-SEM) and to protect the sample, deposition of Au (as conducting layer) and locally Pt (as protection layer) was necessary on the encapsulated grating. Under the burden of these layers, the nanoporous Al_2O_3 layer is compressed so that the porous nature of the cover layer cannot be observed in Fig 3b. The nanoporous nature of the Al_2O_3 layer after heating the alucone layer is revealed in Fig 4a. In this case, the MLD/ALD deposition was done on Si(100) substrate, and the micrograph was taken with scanning electron microscopy (SEM) without any further deposition. Moreover, the decrease of the refractive index of the film after heat treatment from 1.52 to 1.34 at the wavelength of 632.8 nm confirmed the porous nature of the Al_2O_3 film (Fig 4b).

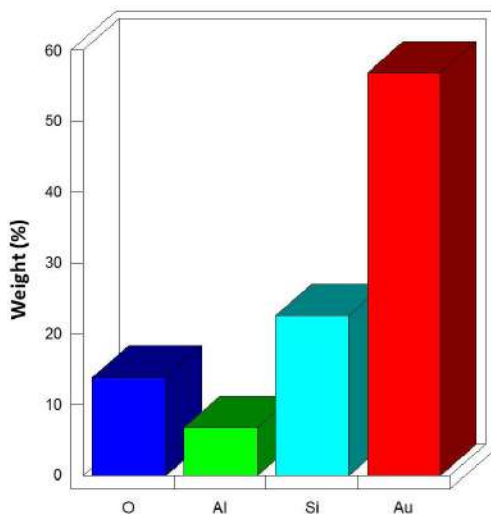


Fig 5. Energy dispersive x-ray spectroscopy (EDX) of the SiO_2 grating encapsulated with Al_2O_3 .

Energy dispersive x-ray spectroscopy analysis (EDX) confirmed that the sacrificial polymer material was completely removed from the grating grooves. Figure 5 shows that only 4 elements could be detected: O, Al, Si and Au. The Au signal comes from the conducting layer deposited to obtain the FIB-SEM micrograph. The Si signal is caused by the substrate (SiO_2 grating), whereas the cover Al_2O_3 gives rise to the Al and partially to the oxygen (O) signal. The carbon (C) signal that might arise from remaining organic component in the alucone layer or from the resist material could not be detected after thermal treatment.

4 Conclusions

In summary, we have developed a versatile route to encapsulate optical gratings by heat treatment of the nanostructured elements covered by MLD/ALD deposited alucone/ Al_2O_3 alloy layer. One cycle of ALD Al_2O_3 was inserted after every 5 cycles of MLD alucone, to avoid excessive collapse of the film after the removal of the organic constituents. The evolution of the porosity in the cover layer and the removal of the sacrificial polymer material could be achieved by simple heat treatment up to 400 °C in air. The EDX measurements showed no signal from carbon (C) after heating, indicating the complete removal of the sacrificial polymer material from the grooves. Further experiments will be carried out to improve the quality of encapsulation by preventing the sinking of the cover layer and to apply this encapsulation method to functional optical elements.

Acknowledgement

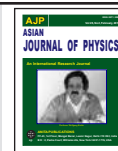
This research was supported by the German Research Foundation within the Emmy Noether Program (SZ253/1-1 grant) and partially by the FhG Internal Programs under Grant No. Attract 066-601020.

This Communication is dedicated to Professor Wolfgang Kiefer on the occasion of his 75th birthday.

References

1. Gupta M C, Peng S T, Diffraction characteristics of surface-relief gratings, *Appl Opt*, 32(1993)2911-2917.
2. Cao H C, Zhou C, Feng J, Lv Peng, Ma J, Polarization-independent triangular-groove fused-silica gratings with high efficiency at a wavelength of 1550 nm, *Opt Commun*, 283(2010)4271-4273.
3. Clausnitzer T, Limpert J, Zöllner K, Zellmer H, Fuchs Hans-Joerg, Kley E-B, Tünnermann A, Jupé M, Ristau D, Highly efficient transmission gratings in fused silica for chirped-pulse amplification systems, *Appl Opt*, 42(2003)6934-6938.
4. Clausnitzer T, Kämpfe T, Kley E-B, Tünnermann A, Tishchenko A V, Parriaux O, Highly-dispersive dielectric transmission gratings with 100% diffraction efficiency, *Opt Express*, 16(2008)5577-5584.
5. Szeghalmi A, Helgert M, Brunner R, Heyroth F, Gösele U, Knez M, Tunable Guided-Mode Resonance Grating Filter, *Advanced Functional Materials*, 20(2010)2053-2062.
6. Nishii J, Kintaka K, Nakazawa T, High-efficiency transmission gratings buried in a fused-SiO₂ glass plate, *Appl Opt*, 43(2004)1327-1330.
7. Clausnitzer T, Kämpfe T, Brückner F, Heinze R, Kley E-B, Tünnermann A, Reflection-reduced encapsulated transmission grating, *Opt Lett*, 33(2008)1972-1974.
8. Kalkowski G, Zeitner U, Benkenstein T, Fuchs J, Rothhardt C, Eberhardt R, Direct wafer bonding for encapsulation of fused silica optical gratings, *Microelectronic Engineering*, 97(2012)177-180.
9. Ratzsch S, Kley E-B, Tünnermann A, Szeghalmi A, Encapsulation process for diffraction gratings, *Opt Express*, 23(2015)17955-17965.
10. Suntola T, Atomic layer epitaxy, *Thin Solid Films*, 216(1992)84-89.
11. George S M, Atomic Layer Deposition: An Overview, *Chem Rev*, 110(2010)111-131.
12. Sundberg P, Karppinen M, Organic and inorganic-organic thin film structures by molecular layer deposition: A review, *Beilstein J Nanotechnol*, 5(2014)1104-1136.
13. Lee B H, Yoon B, Abdulagatov A L, Hall R A, Growth and Properties of Hybrid Organic-Inorganic Metalcone Films Using Molecular Layer Deposition Techniques, *Advanced Functional Materials*, 23(2013)532-546.
14. Dameron, A A, Seghete D, Burton B B, Davidson S D, Cavanagh A S, Bertrand J A, George S M, *Molecular layer deposition of alucone polymer films using trimethylaluminum and ethylene glycol*, *Chemistry of Materials*, 20(2008)3315-3326.
15. Liang X H, Yu Miao, Li J, Jiang Y-B, Weimer A W, Ultra-thin microporous-mesoporous metal oxide films prepared by molecular layer deposition (MLD), *Chem Commun*, 46(2009)7140-7142.
16. Liang X H, Evanko B W, Izar A, King D M, Jiang B Y, Weimer A W, Ultrathin highly porous alumina films prepared by alucone ABC molecular layer deposition (MLD), *Microporous and Mesoporous Materials*, 168(2013)178-182.
17. Yu M A, Funke H, Noble R D, Falconer J L, H₂ Separation Using Defect-Free, Inorganic Composite Membranes, *J Am Chem Soc*, 133(2011)1748-1750.
18. Qin Y, Yang Y, Scholz R, Pippel E, Lu X, Knez M, Unexpected Oxidation Behavior of Cu Nanoparticles Embedded in Porous Alumina Films Produced by Molecular Layer Deposition, *Nano Letters*, 11(2011)2503-2509.
19. Qin Y, Liu L, Yang R, Gösele U, Knez M, General Assembly Method for Linear Metal Nanoparticle Chains Embedded in Nanotubes, *Nano Letters*, 8(2008)3221-3225.
20. Ghazaryan, L, Kley E-B, Tünnermann A, Szeghalmi A V, *Stability and annealing of alucones and alucone alloys*, *Journal of Vacuum Science & Technology A*, 31(2013)01A149; doi.org/10.1116/1.4773296

[Received : 30.09.2015; revised recd: 16.10.2015; accepted: 01.11.2015]



Mechanism of intramolecular multi-electron photochemistry in a 4H-imidazole ruthenium dye

Linda Zedler^{1,2}, Stephan Kupfer², Sven Kriek³, Rainer Beckert⁴, Sven Rau⁵, Michael Schmitt²,
Jürgen Popp^{1,2} and Benjamin Dietzek^{1,2}

¹*Institute of Photonic Technology Jena (IPHT), Albert-Einstein-Straße 9, 07745 Jena, Germany*

²*Institute of Physical Chemistry and Abbe Center of Photonics, Friedrich-Schiller-University Jena, Helmholtzweg 4, 07743 Jena, Germany*

³*Institute of Inorganic and Analytical Chemistry, Friedrich-Schiller-University Jena, Humboldtstraße 8, 07743 Jena, Germany*

⁴*Institute of Organic Chemistry and Macromolecular Chemistry, Friedrich-Schiller-University Jena, Humboldtstraße 10, 07743 Jena, Germany*

⁵*Institute of Inorganic Chemistry I, University Ulm, Albert-Einstein-Allee 11, 89081 Ulm, Germany*

(Dedicated to Professor Wolfgang Kiefer on the occasion of his 75th birthday)

Ruthenium complexes containing a 4H-imidazole chromophore feature a spectrally extremely broad absorption in the UV-Vis and near IR spectral range. In addition, these complexes show a notable redox activity and high chemical stability. These important characteristics render these systems promising for electron storage and inter-molecular electron transfer. But in order to improve the function of electron transfer or storage by modifying the structure, photo-induced structural changes and charge transfer processes with the molecular functionality need to be correlated. This includes also a fundamental understanding of relevant photo-excited states, complex stability and reaction pathways, particularly for multiple electron transfer steps in order to identify parasitic processes, which delimitate the functionality. However, the reactivity and short lifetime of electronically excited complexes renders the detailed spectroscopic characterization cumbersome. In this contribution the combination of spectroscopic tools with the electrochemical preparation of single and double reduced states is used to model the long-time behavior of photo-activated complexes. Specifically, UV-Vis and resonance Raman spectroscopy are performed to investigate a four times quasi-reversible reducible ruthenium complex and the results are analyzed using computational methods. © Anita Publications. All rights reserved.

Keywords: Ruthenium complexes, 4H-imidazole, Chromophore, Redox activity, Life time, UV-Vis and Resonance Raman spectroscopy.

1 Introduction

The unlimited hunger for energy in combination with standard energy production from fossil fuels is a major threat for the future of our societies. While a significant reduction in the total energy consumption is not in sight, the most promising strategy is to substitute fossil fuels by renewable energy sources. Here, solar energy represents the most reliable source for billions of years and green plants demonstrate fruitful strategies for efficient energy collection, conversion and storage. One promising strategy for the conversion of solar to chemical energy is the process of photo-catalytic hydrogen generation [1-3]. Key of the process is a stable photocatalyst, which efficiently collects multiple photoelectrons to catalyze the hydrogen generation. Promising catalytic structures need to be highly stable and efficient, which results in a large turn over number (TON) per molecule and time interval. Hence, the catalysts absorption spectrum needs to match the solar emission spectrum in order to efficiently absorb light. Furthermore, photocatalysts should

Corresponding author :

e-mail: benjamin.dietzek@uni-jena.de; phone: 49-3641-948360 (Benjamin Dietzek)

possess relatively long-lived photo-excited states, such that in comparison to the photoactivation process slow diffusion controlled rereduction of the oxidized photocenter by an electron donor generates a stable charge separated intermediate state [4-6]. These characteristics apply essentially similarly for intramolecular systems composed of antenna, primary electron donor, electron-relay structure and reaction center in a single molecule as well as intermolecular catalysts, where these structures represent separate molecules [7].

To date ruthenium^{II}-polypyridyl complexes which can simultaneously accumulate and store multiple electrons are the best artificial structures for photo-induced energy conversion [8,9]. However, the amount of two electron accepting structures, which feature an absorption spectrum spanning the visible spectral range is marginal [5,10]. Only recently the anion of 2-Phenyl-*N,N'*-substituted-5-*p*-amino-4-*p*-iminoimidazole (*4H*-imidazole) [11] depicted in Fig 1A has been reported to exhibit two-electron-storage capability in combination with a strong absorption covering a substantial portion of the visible spectrum. Hence, further improvements can be expected by fine tuning the electronic configuration via functionalization of the dyes' core structure. By two electron reduction of *4H*-imidazole an aromatic trianion is formed which spatially localizes two electrons [12,13]. Due to this particular property in combination with the small dimension of the molecule, the *4H*-imidazole chromophore represents an excellent candidate as electron acceptor for inclusion in larger inter- or intramolecular electron transfer systems. Ruthenium^{II}-polypyridyl complexes binding the *4H*-imidazole structure feature a broad absorption covering the visible to NIR spectral range. The broadening of the absorption upon complexation of the ligand with a d⁶ metal is due to additional metal to ligand charge transfer (MLCT) excitations in the complex in addition to ligand centered states [14-16]. Furthermore, by substitution of the *4H*-imidazole moiety the light-driven charge transfer kinetics upon excitation of an MLCT state can be tailored to fit a specific application [14].

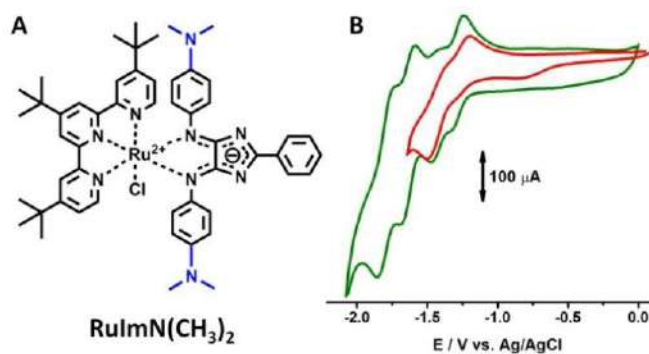


Fig 1. Molecular structure of the complex $\text{RuImN}(\text{CH}_3)_2$ (A) and cyclic voltammogram (B) for the first (red curve) and continuing (green curve) reductions of $\text{RuImN}(\text{CH}_3)_2$ acquired in 0.1 M tetrabutyl ammonium tetrafluoroborate (TBABF₄)/ACN (acetonitrile) at a glassy carbon working electrode at a scan rate of 100 mVs⁻¹.

Nevertheless, while ruthenium complexes incorporating *4H*-imidazole are promising, so far the photo-physical properties of these structures have been only rarely studied in detail in dependence of the redox-state by advanced spectroscopic methods [10]. Time-resolved spectroscopic tools, e.g., transient absorption, help to identify the temporal evolution of excited states [17] and reveal the time constants of the decay processes on timescales between less than 10 fs up to ns [18]. While slower processes are also accessible by time-resolved methods, e.g., on the μs timescale, the formation of long-lived catalytically active intermediate states during photo-induced charge transfer reactions is still difficult to observe. Interestingly, the electronic configuration after photooxidation and subsequent reduction of the photocenter by an electron donor is equal to a reduction product. Thus, electrochemical methods can be employed to prepare the aromatic anion of Ruthenium^{II}-*4H*-imidazoles, which is identical to an intermediate in the photo-catalytic reaction pathway

[19]. The combination of resonance Raman (RR) with spectro-electrochemistry (SEC) enables (i) the identification of structural changes upon reduction, (ii) the localization of the charges and (iii) contribute to the understanding of the excited state dynamics on long timescales. RR-SEC is ideally suited to characterize long-lived intermediate states. In this contribution the complex $\text{RuImN}(\text{CH}_3)_2$ (Chloro- η^3 -4,4',4''-tri-*tert*-butyl-2,2':6',2''-terpyridin- η^2 -phenyl-4,5-*p*-p-dimethylaminophenyl-imino-imidazolate-Ru^{II}) (Fig 1A) and its anions are for the first time studied by combining electrochemistry coupled to UV-Vis and resonance Raman spectroscopy in order to optimize the structures for applications in light-induced catalysis, e.g., for hydrogen generation. For interpretation, the results from RR-SEC have been modeled at the (time-dependent) density functional theory (TDDFT) level.

2 Experimental

The ruthenium^{II} complex $\text{RuImN}(\text{CH}_3)_2$ was synthesized according to literature [15]. The investigated analyte solutions were prepared by dissolving the analyte in acetonitrile (ACN, Aldrich). The solvent was thoroughly degassed and dehydrated using calcium hydride and twice drawn by distillation. The electrochemical measurements, i.e., cyclic voltammetry and UV-Vis-spectro-electrochemical measurements, were performed using either a standard electrochemical cell or a thin-layer quartz spectro-electrochemical cell (Bioanalytical Systems, Inc). To the degassed analyte solution (50 μM) 0.1 M TBABF₄ was added as electrolyte. The analyte solution was investigated by cyclovoltammetry between the open circuit potential (ocp) and the reduction potential of the solvent (Fig 1B). During cyclovoltammetry UV-Vis absorption spectra of the solution were acquired in a three-electrode configuration. For all electrochemical measurements a Pt-counter and a Ag/AgCl-pseudo reference electrode were employed. For SEC measurements in a special SEC cell (Bioanalytical Systems, Inc) a Pt-gauze working electrode was used, while a glassy-carbon working electrode was employed in a standard electrochemical cell. The solutions were completely degassed with Argon just before the measurements were performed. UV-Vis absorption spectroscopy was conducted using a two-beam UV-Vis spectrometer (Cary 5000, Varian) at 1 nm spectral resolution and at room temperature. For acquiring RR spectra an Argon-ion laser (Innova 300C, Coherent) was used as excitation source. RR-SEC measurements were performed in transmission mode. The laser was filtered using a laser clean up filter (Semrock) and focused into the SEC cell at the working electrode using a 10 \times microscope objective (Olympus). The scattered light was collimated using an achromatic lens. The Rayleigh scattered light was filtered by a long pass filter (Semrock) and the remaining signal focused into a fiber by an achromatic lens. The fiber was coupled to the entrance slit of a 750 mm focal length spectrograph (Acton SpectraPro 2758i). The Raman spectra were recorded at 100 μm entrance slit width using a grating with 600 lines/mm using a liquid nitrogen cooled CCD (SPEC-10, Roper Scientific). All spectra were normalized to the 1373 cm^{-1} Raman band of acetonitrile. The spectra were preprocessed in order to calibrate the wavenumber axes equally and to achieve background-corrected spectra. Reproducibility of the measurements was ensured by acquiring RR spectra at the open circuit potential (ocp) before and after each spectroelectrochemical data acquisition (Fig S1).

3 Computational Details

In order to reduce the computational cost of the simulations without affecting the spectroscopic properties of the complex, the three *tert*-butyl groups of the terpyridine ligand have been approximated in the calculations by methyl groups. The structural and electronic data for $\text{RuImN}(\text{CH}_3)_2$ were obtained from quantum chemical simulations performed using the Gaussian 09 program [20]. The complex has been investigated in its non-reduced singlet form as well as in its single reduced doublet and its double reduced singlet and triplet forms. The geometries, vibrational frequencies and normal coordinates of the electronic ground state (non-reduced: singlet, single reduced: doublet, double reduced: singlet and triplet) were calculated at the DFT level of theory using the B3LYP [21] exchange-correlation functional and employing the 6-31G(d)

double- ζ basis set [22] for all main group elements. For the ruthenium atom the 28-electron relativistic core potential MWB [23] was applied with its basis set describing the valence electrons (4s, 4p, 4d and 5s) explicitly and the inner shells by means of a core potential. In order to correct for the lack of anharmonicity and the approximate treatment of electron correlation the harmonic vibrational frequencies were scaled by a factor of 0.97 [24]. Vertical excitation energies, oscillator strengths and analytic Cartesian energy derivatives of the excited states were obtained by TDDFT within the adiabatic approximation and by utilizing the same exchange-correlation functional, basis set and pseudopotential. As shown in Refs [14] and [15], B3LYP provides the most balanced description of the absorption features for this class of complexes.

The simulated absorption spectra have been determined based on the excitation energies and oscillator strengths of the 80 lowest excited states of the respective ground state multiplicity. The integral equation formalism of the polarizable continuum model [25] was applied to take interactions with a solvent (ACN: $\epsilon = 35.688$, $n = 1.344$) into account with respect to the equilibrium geometry, vibrational frequencies, excitation energies, transition dipole moments and excited state gradients. For the calculations of the excitation energies and excited state gradients, where only the fast reorganization of the solvent is important, the non-equilibrium procedure of solvation was used.

The RR spectra have been calculated within the independent mode displaced harmonic oscillator model (IMDHOM) assuming that the electronic ground and excited states potentials are harmonic oscillators and merely displaced in the equilibrium position and, hence, share the same set of vibrational modes [26]. Detailed information with respect to the computational method can be found in Refs [27] and [28] and the references therein.

In order to calculate the RR intensities of the present ruthenium complexes upon excitation at 514 nm a dumping factor of $\Gamma = 1500 \text{ cm}^{-1}$ describing homogeneous broadening was assumed in the simulation to reproduce the experimental broadening.

The RR intensity pattern for the non-reduced form has been simulated by taking into account contributions from the S_6 , S_7 , S_8 , S_9 and S_{12} , while all excitation energies have been shifted by -1600 cm^{-1} . The respective RR spectrum of the single reduced form was obtained based on the unshifted excited doublet states D_{21} , D_{22} and D_{26} . For the RR intensity pattern of the double reduced complex singlet as well as triplet multiplicity was taken into account. In case of the double reduced singlet contributions from the excited states S_{11} , S_{13} , S_{14} and S_{15} have been considered, while for the corresponding triplet the states T_6 , T_{18} and T_{23} have been investigated.

4 Results and Discussion

The chemical structure of $\text{RuImN}(\text{CH}_3)_2$ is displayed in Fig 1A. In Fig 1B the cyclic voltammogram (CV) acquired in the reductive potential range of the ruthenium complex $\text{RuImN}(\text{CH}_3)_2$ is depicted. The CV is characterized by four quasi-reversible reductions at -1.20 , -1.35 , -1.64 and -1.80 V . The first and second reduction steps are close together, hence, the respective peaks are not well resolved in the CV. The first reduction is localized at the 4*H*-imidazole ligand [29]. However, cyclic voltammetry alone does neither allow for identifying reduction products, nor does it enable to retrieve information on the location of the negative charge and accompanying structural changes. To determine structural alterations upon reduction, the neutral as well as the electrochemically reduced complex $\text{RuImN}(\text{CH}_3)_2$ were spectroscopically investigated utilizing UV-Vis and RR spectroscopy. Therefore, first results from UV-Vis spectroscopy of the neutral and the reduced complex are presented, followed by data from RR spectroscopy. In Fig 2 measured UV-Vis spectra of the neutral and reduced complex $\text{RuImN}(\text{CH}_3)_2$ are compared with TDDFT calculations. Photoexcitation of $\text{RuImN}(\text{CH}_3)_2$ in the UV-Vis ($> 400 \text{ nm}$) (Fig 2A) leads to the population of several bright MLCT states towards the 4*H*-imidazole such as S_2 , S_6 and S_9 , see acceptor orbital in Fig 2C, but also towards the terpyridine ligand (S_7 , S_8 and S_{12}) [14]. The first reduction of $\text{RuImN}(\text{CH}_3)_2$ at -1.20 V is localized at the 4*H*-imidazole ligand as derived from DFT (single reduced doublet). During reduction, the peak of

the energetically lowest absorption declines, whereas the MLCT band at 500 nm shifts bathochromically to 520 nm. The computational results, illustrated in Fig 2B, unravel the electronic excited states underlying this bathochromic shift, which is related to three bright MLCT states associated with the terpyridine ligand (see D_{21} , D_{22} and D_{26} ; detailed information are summarized in table S1 and S2 of the supporting information) of the single reduced doublet species at 547, 542 and 512 nm, respectively. However, due to the vicinity of the first and the second reduction potential a (partial) contribution originating from the double reduced species to the observed absorption spectrum cannot be excluded. Here, two potential spin states - singlet and triplet - are conceivable, while both spin states feature with the S_{14} and S_{15} (520 and 512 nm) as well as with the T_{16} , T_{18} and T_{23} (602, 587 552 nm) bright excited states in the region of the newly formed absorption feature (520 nm) upon reduction, see Fig 2E and F as well as table S1 and S2 for detailed information. Thus, a (partial) contribution of the double reduced complex to the rising absorption feature in Fig 2A cannot be excluded.

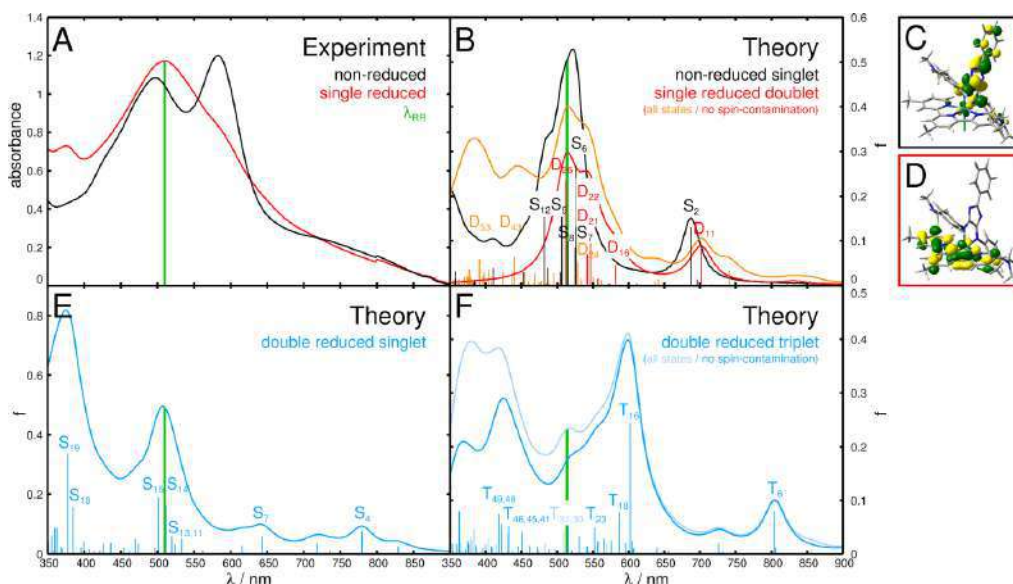


Fig 2 A. In situ UV-Vis absorption spectro-electrochemical analysis of intermediate reduction states of $\text{RuImN}(\text{CH}_3)_2$. The RR excitation wavelength is displayed as a green line in the spectra. (B) Calculated spectra of $\text{RuImN}(\text{CH}_3)_2$ (black: non-reduced singlet, red: single reduced doublet). (C) Photoexcitation of the non-reduced complex at 514 nm results in transfer of excess charge density into the LUMO localized at the 4H-imidazole ligand. (D) Main acceptor molecular orbitals of single reduced $\text{RuImN}(\text{CH}_3)_2$ upon photoexcitation at 514 nm. Calculated absorption spectra of double reduced singlet, (E), and triplet, (F) of $\text{RuImN}(\text{CH}_3)_2$ (blue).

As can be seen based on the quantum chemical investigation on the single reduced species, all bright excited states in the visible region are of MLCT character towards the terpyridine ligand (Fig 2D). Hence, in contrast to the isolated reduced 4H-imidazole upon incorporation into a complex the 4H-imidazole ligand does not accept an additional excess charge upon photoexcitation. To obtain further insight into structural changes upon photoactivation and single reduction, $\text{RuImN}(\text{CH}_3)_2$ was investigated during reduction by RR-SEC. RR spectroscopy is the ideal tool to determine key structure changes and changes in the electronic configuration during photoactivation. This is due to the fact, that normal modes become selectively enhanced in RR spectra, which are strongly affected by the molecular rearrangement upon absorption. These modes are so-called Franck-Condon active modes [27,30]. In agreement with results from UV-Vis SEC, the first reduction is localized on the 4H-imidazole fragment, assuming, that reduction and photoexcitation populate the same electronic state. Raman marker bands of the 4H-imidazole are enhanced in the RR spectrum of the non-reduced complex (Fig 3 black traces and Table S3). In order to investigate the nature of the MLCT

states underlying the newly formed absorption feature of the reduced $\text{RuImN}(\text{CH}_3)_2$ at 520 nm RR-SEC was performed. The RR-SEC spectrum measured upon excitation at 514 nm is depicted in Fig 3A (blue traces); it is dominated by intense Raman features at 1476 and 1504 cm^{-1} . The simulated RR intensity pattern obtained for the single reduced (doublet) complex is in fair agreement with the experimental pattern and features almost exclusively intense vibrational normal modes localized on the terpyridine ligand. In order to investigate a possible double reduction caused by the close lying first and second reduction potentials, RR spectra have been calculated not only for the single reduced doublet but also for the double reduced singlet and triplet form, while DFT predicts the double reduced triplet to be 0.06 eV more stable than the singlet. In line with this result the simulated RR spectrum of the double reduced triplet is in very good agreement with the experimental spectrum (Fig 3, Table S3), while no appreciable agreement was found for the respective singlet species. Thus, the experimental data indicate a (partial) double reduction at the given experimental conditions, and the Raman features observed upon reduction (1476 and 1504 cm^{-1}) can be assigned to terpyridine centered vibrational modes at 1482.0 and 1503.0 cm^{-1} . Detailed information with respect to the calculated RR spectra as well as to the computational protocol are presented in the supporting information. The population of the triplet state agrees also (i) with the calculated LUMO-orbitals of the neutral and the single reduced complex as depicted in Fig 3C and D and (ii) with the RR-SEC data, which point to localization of the photoelectron of the single reduced $\text{RuImN}(\text{CH}_3)_2$ on the terpyridine ligand. This is a notable difference to the non-reduced species $\text{RuImN}(\text{CH}_3)_2$, in which photoinduced metal-to-ligand charge transfer is directed towards the 4H-imidazole ligand (Fig 3C, S5). Therefore, confinement of a (photo)electron at the reduced 4H-imidazole ligand is energetically not favored for the $\text{RuImN}(\text{CH}_3)_2$ complex due to Coulomb repulsion, even though the free 4H-imidazole ligand can accept a second electron as shown by electrochemistry.

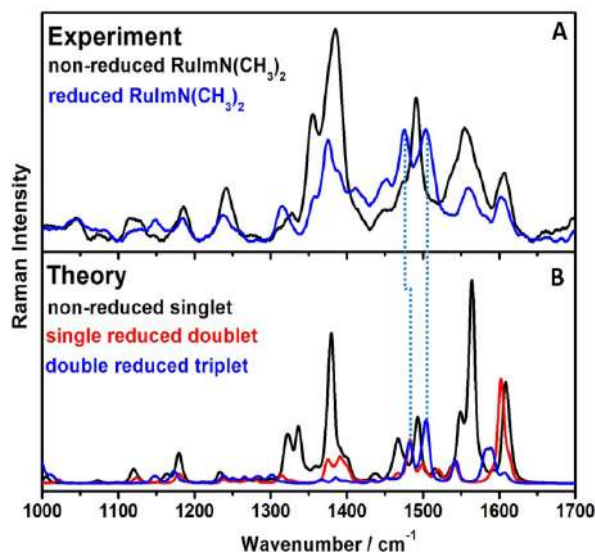
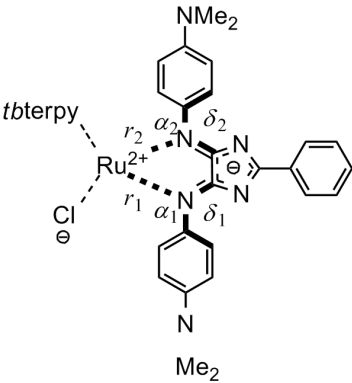


Fig 3. (A) Experimental RR spectra of non-reduced (black) and electro-chemically reduced (blue) $\text{RuImN}(\text{CH}_3)_2$, excited at 514 nm. B) TDDFT-calculated RR spectra of non-reduced singlet (black), single reduced doublet (red) and double reduced triplet (blue) of $\text{RuImN}(\text{CH}_3)_2$. The good agreement of the double reduced pattern with the experimental results points the presence of the double reduced species during electrolysis. The labeled vibrations are assigned by means of quantum-chemical calculations.

This phenomenon can be understood based on the computational results as summarized in Table 1, where the main structural parameters and relative ground state energies are given for the non-reduced, the

single reduced and double reduced species. In line with the first photoexcitation of the non-reduced complex being (mainly) directed towards the 4H-imidazole, the first electrochemical reduction of RuImN(CH₃)₂ is localized on the 4H-imidazole. The two-electron storage capacity of the 4H-imidazole is governed by the population of two competitive states, the double reduced singlet and the double reduced triplet. As can be seen in Table 1, the equilibrium structure of the complex is hardly affected upon single reduction. Introduction of yet an additional electron to the system can lead to a double reduced singlet, where both electrochemically introduced electrons are located on the 4H-imidazole and a double reduced triplet, where both ligand spheres (4H-imidazole and terpyridine) comprise each one electron. Here the equilibrium structure of the triplet shows again at best marginal alternations from the non-reduced and the single-reduced forms.

Table 1. Electronic ground state energies (E) and structural parameters (bond lengths: r_1 and r_2 , pyramidalization: α_1 and α_2 , torsion of the terminal anilyl moieties with respect to central 4H-imidazole plane: δ_1 and δ_2) for the non-reduced (singlet), the single reduced (doublet) and double reduced species (singlet and triplet).

	E / eV	$r_1 / \text{\AA}$	$r_2 / \text{\AA}$	$\alpha_1 / ^\circ$	$\alpha_2 / ^\circ$	$\delta_1 / ^\circ$	$\delta_2 / ^\circ$	
	Non-reduced singlet	0.00	2.194	2.111	179	177	-42	54
	Single reduced doublet	-2.49	2.211	2.120	174	176	-29	41
	Double reduced singlet	-4.51	2.169	2.113	154	171	-2	15
	Double reduced triplet	-4.57	2.243	2.118	171	179	-22	41

However, in the double-reduced singlet state the 4H-imidazole undergoes considerable structural changes. In order to stabilize two charges the terminal anilyl moieties planarize with respect to the central fragment as reflected in the changes of the dihedral angles δ_1 and δ_2 (Table 1). This planarization is accompanied by a slight pyramidalization of the anilyl moieties as reflected in the values of α_1 and α_2 . These structural alterations enable a distribution of the two additional charges along the entire π -system of the ligand. However, comparison of the ground state energies of both double reduced forms yields that the triplet, distributing both electrons on both ligand spheres is by approximately 0.06 eV more stable than the singlet state. Hence, the electron donating character of the terminal dimethylamino groups of the 4H-imidazole fragment provide additional charge density to the ligand hindering the stabilization of the double reduced singlet state.

5 Conclusion

The investigation of long-lived photointermediates and their photo-physical properties is of vital importance for any photo-activated process, this is in particular the case for light-harvesting molecular devices. In order to determine the (multi-) electron storage capacity of such molecules, spectro-electrochemical methods, i.e., UV-Vis-spectro-electrochemistry and resonance Raman (RR)-spectro-electrochemistry coupled with quantum chemical calculations are the method of choice. The joint spectroscopic-theoretical investigation on the two-electron storage capacity of a ruthenium complex containing a 4H-imidazole black dye presented here reveals that the primary photoexcitation shift charge density from the central ruthenium^{II} ion to the 4H-imidazole ligand. To investigate the charge density shifts associated with a second photoexcitation UV-Vis- and RR-SEC measurements have been performed. Based on quantum chemical calculations the newly

formed absorption features of the reduced complex were assigned to terpyridine centered MLCT states. In line with this finding also the RR signals of the (single and double) reduced RuImN(CH₃)₂ point to a charge transfer towards the terpyridine sphere. The keystone in transferring two (photo) electrons on the 4H-imidazole was found to be correlated to the competitive population of the double reduced singlet and triplet. Exclusively, the double reduced singlet is able to stabilize two additional charges on the 4H-imidazole caused by a planarization of the entire ligand and, thus, enabling an effective charge distribution. However, the electron-donating dimethylamino groups in the periphery of the 4H-imidazole destabilize the double-reduced singlet state by donating additional charge-density to the 4H-imidazole. In consequence, double reduced triplet state is populated featuring one (photo)electron on each ligand sphere.

References

1. Zeitler K, *Angew Chem Int Ed*, 48(2009)9785-9789.
2. Balzani V, Juris A, Venturi M, Campagna S, Serroni S, *Chem Rev*, 96(1996)759-834.
3. Elvington M, Brown J, Arachchige S M, Brewer K J, *J Am Chem Soc*, 129(2007)10644-10645.
4. Gray H B, Maverick A W, *Science*, 214(1981)1201-1205.
5. Esswein A J, Nocera D G, *Chem Rev*, 107(2007)4022-4047.
6. Zedler L, Guthmuller J, Rabelo de Moraes I, Kupfer S, Kriek S, Schmitt M, Popp J, Rau S, Dietzek B, *Chem Commun*, 50(2014)5227-5229; doi: 10.1039/C3CC47487A
7. Mourtzis N, Carballada P C, Felici M, Nolte R J M, Williams R M, Cola L, de Feiters M C, *Phys Chem Chem Phys*, 13(2011)7903-7909.
8. Rosenthal J, Bachman J, Dempsey J L, Esswein A J, Gray T G, Hodgkiss J M, Manke D R, Luckett T D, Pistorio B J, Veige A S, Nocera D G, *Coord Chem Rev*, 249(2005)1316-1326.
9. Chiorboli C, Fracasso S, Scandola F, Campagna S, Serroni S, Konduri R, MacDonnell F M, *Chem Commun*, (2003) 1658-1659; doi: 10.1039/B302962J
10. Zedler L, Kupfer S, Rabelo de Moraes I, Wächtler M, Beckert R, Schmitt M, Popp J, Rau S, Dietzek B, *Chem – Eur J*, 20(2014)3793-3799
11. Sammes M P, Katritzky A R, *The 4H-Imidazoles. Advances in Heterocyclic Chemistry*, (Academic Press), 1984, pp 413-450,
12. Gebauer T, Beckert R, Weiss D, Knop K, Käßlinger C, Görls H, *Chem Commun*, (2004)1860-1861; doi: 10.1039/B403480E
13. Beckert R, Atzrodt J, Görls H, *Heterocycles*, 51(1999)763-783
14. Wächtler M, Kupfer S, Guthmuller J, Rau S, González L, Dietzek B, *J Phys Chem C*, 116(2012)25664-25676
15. Kupfer S, Guthmuller J, Wächtler M, Losse S, Rau S, Dietzek B, Popp J, González L, *Phys Chem Chem Phys*, 13(2011)15580-15588
16. Blumhoff J, Beckert R, Rau S, Losse S, Matschke M, Günther W, Görls H, *Eur J Inorg Chem*, (2009)2162-2169; doi.org/10.1002/ejic.200800914
17. Kukura P, McCamant D W, Mathies R A, *Annu Rev Phys Chem*, 58(2007)461-488.
18. Sun Y, Liu Y, Turro C, *J Am Chem Soc*, 132(2010)5594-5595.
19. Kaim W, Fiedler J, *Chem Soc Rev*, 38(2009)3373-3382.
20. Frisch M J, Trucks G W, Schlegel H B, Scuseria G E, Robb M A, Cheeseman J R, Scalmani G, Barone V, Mennucci B, Petersson G A, Nakatsuji H, Caricato M, Li X, Hratchian H P, Izmaylov A F, J, Bloino G Z, Sonnenberg J L, Hada M, Ehara M, Toyota K, Fukuda R, Hasegawa J, Ishida M, Nakajima T, Honda Y, Kitao O, Nakai H, Vreven T, Montgomery J J A, Peralta J E, Ogliaro F, Bearpark M, Heyd J J, Brothers E, Kudin K N, Staroverov V N, Kobayashi R, Normand J, Raghavachari K, Rendell A, Burant J C, Iyengar S S, Tomasi J, Cossi M, Rega N, Millam J M, Klene M, Knox J E, Cross J B, Bakken V, Adamo C, Jaramillo J, Gomperts R, Stratmann R E O, Yazyev A J A R, Cammi C P, Ochterski J W, Martin R L, Morokuma K, Zakrzewski V G, Voth G A, Salvador P, Dannenberg J J, Dapprich S, Daniels A D, Farkas O, Foresman J B, Ortiz J V, Cioslowski J, Fox D J, *Gaussian 09 Revision A.1* (Gaussian Inc, Wallingford CT), 2009

21. Becke A D, *J Chem Phys*, 98(1993)5648-5652.
22. Hariharan P C, Pople J A, *Theor Chim Acta*, 28(1973)213-222.
23. Andrae D, Häusermann U, Dolg M, Stoll H, Preuß H, *Theor Chim Acta*, 77(1990)123-141.
24. Merrick J P, Moran D, Radom L, *J Phys Chem A*, 111(2007)11683-11700.
25. Mennucci B, Cappelli C, Guido C A, Cammi R, Tomasi J, *J Phys Chem A*, 113(2009)3009-3020.
26. Page J B, Tonks D L, *J Chem Phys*, 75(1981)5694-5708.
27. Wächtler M, Guthmüller J, González L, Dietzek B, *Coord Chem Rev*, 256(2012)1479-1508
28. Guthmüller J, González L, *Phys Chem Chem Phys*, 12(2010)14812-14821.
29. Losse S, Redoxaktive metallorganische Farbstoffkomplexe zur Verwendung in Photovoltaik und Photokatalyse. (Thesis, Friedrich-Schiller-Universität Jena), 2010.
30. Tschierlei S, Karnahl M, Presselt M, Dietzek B, Guthmüller J, González L, Schmitt M, Rau S, Popp J, *Angew Chem Int Ed*, 49(2010)3981-3984.

[Received: 30.09.2015; accepted: 07.02.2016]

Supporting Information

Mechanism of intramolecular multi-electron photochemistry in a 4H-imidazole Ruthenium dye

Linda Zedler^{1,2}, Stephan Kupfer², Sven Krieck³, Rainer Beckert⁴, Sven Rau⁵, Michael Schmitt², Jürgen Popp^{1,2} and Benjamin Dietzek^{1,2}

¹Institute of Photonic Technology Jena (IPHT), Albert-Einstein-Straße 9, 07745 Jena, Germany

²Institute of Physical Chemistry and Abbe Center of Photonics, Friedrich-Schiller-University Jena, Helmholtzweg 4, 07743 Jena, Germany

³Institute of Inorganic and Analytical Chemistry, Friedrich-Schiller-University Jena, Humboldtstraße 8, 07743 Jena, Germany

⁴Institute of Organic Chemistry and Macromolecular Chemistry, Friedrich-Schiller-University Jena, Humboldtstraße 10, 07743 Jena, Germany

⁵Institute of Inorganic Chemistry I, University Ulm, Albert-Einstein-Allee 11, 89081 Ulm, Germany

Table S1. Calculated bright electronic excited states for the non-reduced (singlet) and single (doublet) reduced species of RuImN(CH₃)₂ with main contributing transitions, excitation energies E^e (in eV) and wavelengths λ (in nm), oscillator strengths f , and eigen values of

Non-reduced singlet							
State	Transition	Weight / %	E^e / eV	λ / nm	f		λ_{exp} / nm
S ₂	$d_{xz}(198) \rightarrow \pi_{\text{im}}^*(199)$ MLCT	86	1.81	687	0.1309	0.00	710
	$d_{xz} - d_{xy} + \pi_{\text{im}}(196) \rightarrow \pi_{\text{im}}^*(199)$ MLCT	53					
S ₆	$d_{xz} + d_{xy} + \pi_{\text{im}}(197) \rightarrow \pi_{\text{im}}^*(199)$ MLCT	13	2.35	527	0.2682	0.00	583
	$d_{xz}(198) \rightarrow \pi_{\text{im}}^*(199)$ MLCT	9					
	$d_{xy}(195) \rightarrow \pi_{\text{im}}^*(199)$ MLCT	9					
S ₇	$d_{xz} - d_{xy} + \pi_{\text{im}}(196) \rightarrow \pi_{\text{terpy}}^*(200)$ MLCT	46	2.36	525	0.0848	0.00	
	$d_{yz}(194) \rightarrow \pi_{\text{terpy}}^*(200)$ MLCT	11					
	$d_{xy}(195) \rightarrow \pi_{\text{terpy}}^*(200)$ MLCT	43					
S ₈	$d_{xz} + d_{xy} + \pi_{\text{im}}(197) \rightarrow \pi_{\text{terpy}}^*(200)$ MLCT	14	2.41	514	0.0991	0.00	
	$d_{xz} - d_{xy} + \pi_{\text{im}}(196) \rightarrow \pi_{\text{terpy}}^*(200)$ MLCT	11					
	$d_{xy}(195) \rightarrow \pi_{\text{im}}^*(199)$ MLCT	29					
	$d_{xz} - d_{xy} + \pi_{\text{im}}(196) \rightarrow \pi_{\text{terpy}}^*(201)$ MLCT	22					
S ₉	$d_{yz}(194) \rightarrow \pi_{\text{im}}^*(199)$ MLCT	15	2.45	507	0.1533	0.00	
	$d_{xy}(195) \rightarrow \pi_{\text{terpy}}^*(201)$ MLCT	13					
	$d_{xz} + d_{xy} + \pi_{\text{im}}(197) \rightarrow \pi_{\text{terpy}}^*(201)$ MLCT	9					
	$d_{xy}(195) \rightarrow \pi_{\text{terpy}}^*(201)$ MLCT	43					
S ₁₂	$d_{xz} + d_{xy} + \pi_{\text{im}}(197) \rightarrow \pi_{\text{im}}^*(199)$ MLCT	21	2.57	482	0.1527	0.00	499
	$d_{xy}(195) \rightarrow \pi_{\text{im}}^*(199)$ MLCT	10					
Single-reduced doublet							
State	Transition	Weight / %	E^e / eV	λ / nm	f		λ_{exp} / nm
D ₁₁	$d_{xz} + \pi_{\text{im}}(198\beta) \rightarrow \pi_{\text{im}}^*(201\beta)$ MLCT	71	1.77	701	0.0819	0.83	
	$d_{xz} + \pi_{\text{im}}(198\alpha) \rightarrow \pi_{\text{terpy}}^*(201\alpha)$ MLCT	18					

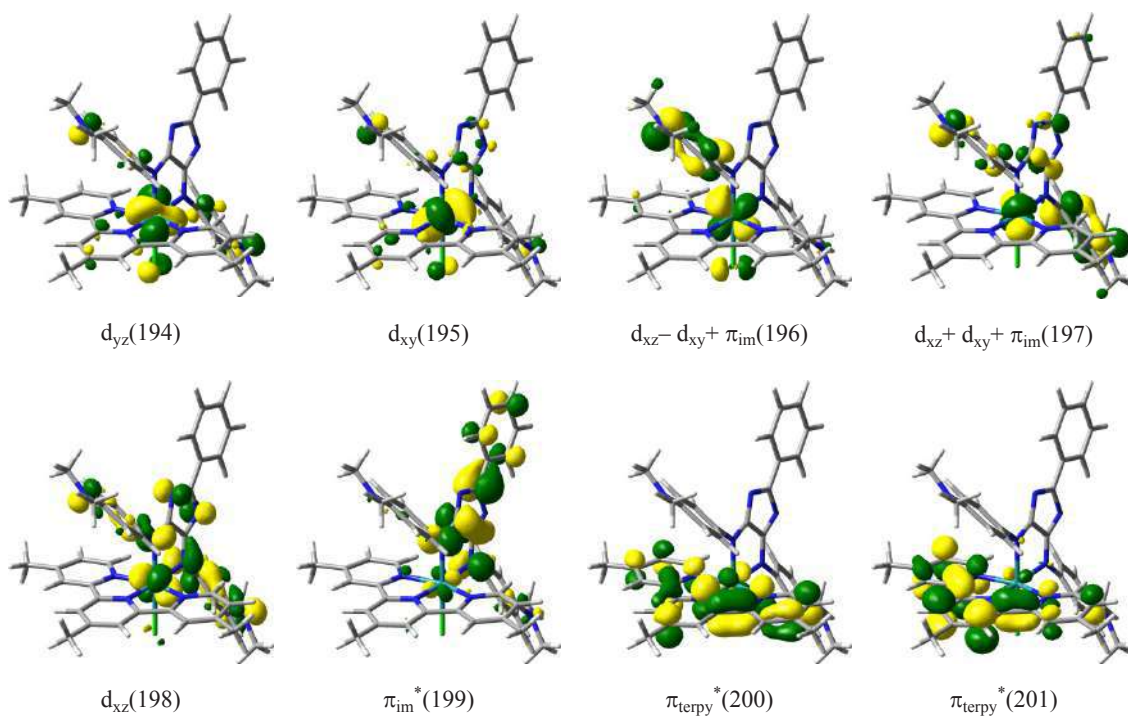
	$\pi_{im}^*(199\alpha) \rightarrow \pi_{im}^*(205\alpha)$ ILCT	34					
D ₁₆	$\pi_{im}^*(199\alpha) \rightarrow \pi_{terpy}^*(204\alpha)$ MLCT	21	2.13	582	0.0461	0.94	520
	$d_{xy} + \pi_{im}^*(197\beta) \rightarrow \pi_{im}^*(201\beta)$ MLCT	16					
	$\pi_{im}^*(199\alpha) \rightarrow \pi_{im}^*(205\alpha)$ ILCT	12					
	$d_{yz}(196\beta) \rightarrow \pi_{terpy}^*(200\beta)$ MLCT	23					
D ₂₁	$d_{yz}(196\beta) \rightarrow \pi_{terpy}^*(199\beta)$ MLCT	16					
	$d_{yz}(196\alpha) \rightarrow \pi_{terpy}^*(200\alpha)$ MLCT	14	2.27	547	0.0947	0.87	520
	$d_{yz}(196\alpha) \rightarrow \pi_{terpy}^*(201\alpha)$ MLCT	13					
	$d_{xz}(195\beta) \rightarrow \pi_{terpy}^*(200\beta)$ MLCT	12					
	$d_{xz}(195\alpha) \rightarrow \pi_{terpy}^*(200\alpha)$ MLCT	29					
D ₂₂	$d_{xz}(195\beta) \rightarrow \pi_{terpy}^*(199\beta)$ MLCT	15	2.29	542	0.0697	0.90	520
	$d_{yz}(196\alpha) \rightarrow \pi_{terpy}^*(201\alpha)$ MLCT	7					
	$d_{xy} + \pi_{im}^*(197\beta) \rightarrow \pi_{terpy}^*(201\beta)$ MLCT	6					
	$d_{xz}(195\beta) \rightarrow \pi_{terpy}^*(200\beta)$ MLCT	32					
D ₂₄	$d_{xz}(195\alpha) \rightarrow \pi_{terpy}^*(201\alpha)$ MLCT	30	2.35	528	0.0526	2.45	-
	$d_{xy} + \pi_{im}^*(197\beta) \rightarrow \pi_{terpy}^*(201\beta)$ MLCT	32					
D ₂₆	$d_{xz}(195\alpha) \rightarrow \pi_{terpy}^*(201\alpha)$ MLCT	31	2.42	512	0.2338	0.92	520
	$d_{xz}(195\beta) \rightarrow \pi_{terpy}^*(200\beta)$ MLCT	8					
	$\pi_{im}^*(199\alpha) \rightarrow d_{z^2}(206\alpha)$ LMCT	6					
	$d_{xz} + \pi_{im}(198\alpha) \rightarrow \pi_{terpy}^*(203\alpha)$ MLCT	18					
D ₄₃	$\pi_{im}^*(199\alpha) \rightarrow \pi_{im}^*(205\alpha)$ ILCT	12					
	$d_{xy}(194\beta) \rightarrow \pi_{terpy}^*(201\beta)$ MLCT	12	2.84	437	0.0316	1.18	520
	$d_{xz} + \pi_{im}(198\beta) \rightarrow \pi_{terpy}^*(203\beta)$ MLCT	7					
	$d_{xz}(195\beta) \rightarrow \pi_{terpy}^*(201\beta)$ MLCT	6					
	$\pi_{im}^*(199\alpha) \rightarrow d_{x^2-y^2}(213\alpha)$ LMCT	6					
	$\pi_{im}(193\alpha) \rightarrow d_{x^2-y^2}(213\alpha)$ LMCT	54	3.17	391	0.0594	1.43	375
D ₅₃	$\pi_{im}^*(199\alpha) \rightarrow d_{z^2}(214\alpha)$ LMCT	12					
Double reduced singlet							
S ₄	$\pi_{im}(198) \rightarrow \pi_{terpy}^*(200)$	46	1.59	779	0.0756		-
	$\pi_{im}(198) \rightarrow \pi_{terpy}^*(201)$	40					
S ₇	$d_{xy}(197) \rightarrow \pi_{terpy}^*(200)$	58	1.93	644	0.0606		-
	$d_{xy}(197) \rightarrow \pi_{terpy}^*(201)$	22					
S ₁₁	$d_{yz}(196) \rightarrow \pi_{terpy}^*(200)$	38	2.32	534	0.0523		-
	$d_{xz}(195) \rightarrow \pi_{terpy}^*(200)$	37					
S ₁₃	$\pi_{im}^*(199) \rightarrow d_{z^2}(205)$	40					
	$d_{yz}(196) \rightarrow \pi_{terpy}^*(201)$	21	2.39	520	0.0582		-
	$\pi_{im}^*(199) \rightarrow \pi_{im}^*(204)$	13					
	$d_{yz}(196) \rightarrow \pi_{terpy}^*(200)$	10					

	$d_{xz}(195) \rightarrow \pi_{\text{terpy}}^*(201)$	35					
S ₁₄	$\pi_{\text{im}}^*(199) \rightarrow \pi_{\text{terpy}}^*(206)$	22	2.42	512	0.1651		-
	$d_{yz}(196) \rightarrow \pi_{\text{terpy}}^*(200)$	10					
	$\pi_{\text{im}}^*(199) \rightarrow d_z(205)$	9					
	$d_{yz}(196) \rightarrow \pi_{\text{terpy}}^*(201)$	25					
S ₁₅	$d_{xz}(195) \rightarrow \pi_{\text{terpy}}^*(201)$	17	2.47	501	0.1913		-
	$\pi_{\text{im}}^*(199) \rightarrow \pi_{\text{terpy}}^*(206)$	10					
S ₁₈	$\pi_{\text{im}}(198) \rightarrow \pi_{\text{terpy}}^*(202)$	66	2.62	474	0.0333		-
	$d_{xz}(195) \rightarrow \pi_{\text{terpy}}^*(201)$	14					
S ₁₉	$\pi_{\text{im}}^*(199) \rightarrow \pi_{\text{terpy}}^*(210)$	92	2.64	470	0.0503		-
Double reduced triplet							
T ₆	$\pi_{\text{im}}(198\beta) \rightarrow \pi_{\text{im}}^*(199\beta)$	86	1.54	805	0.0798	2.13	
	$\pi_{\text{terpy}}^*(200\alpha) \rightarrow \pi_{\text{im}}^*(203\alpha)$	19					
	$\pi_{\text{im}}^*(199\alpha) \rightarrow \pi_{\text{im}}^*(203\alpha)$	17					
T ₁₆	$d_{xy}(197\beta) \rightarrow \pi_{\text{im}}^*(199\beta)$	13	2.06	602	0.2451	2.22	520
	$\pi_{\text{terpy}}^*(200\alpha) \rightarrow \pi_{\text{terpy}}^*(204\alpha)$	10					
	$\pi_{\text{terpy}}^*(200\alpha) \rightarrow \pi_{\text{im}}^*(206\alpha)$	7					
	$d_{yz}(196\beta) \rightarrow \pi_{\text{im}}^*(199\beta)$	6					
	$\pi_{\text{terpy}}^*(200\alpha) \rightarrow \pi_{\text{im}}^*(205\alpha)$	35					
T ₁₈	$\pi_{\text{im}}^*(199\alpha) \rightarrow \pi_{\text{im}}^*(206\alpha)$	9	2.11	587	0.0782	2.33	520
	$d_{xy}(197\alpha) \rightarrow \pi_{\text{terpy}}^*(201\alpha)$	9					
	$d_{yz}(196\alpha) \rightarrow \pi_{\text{terpy}}^*(201\alpha)$	32					
T ₂₃	$d_{xy}(197\beta) \rightarrow \pi_{\text{terpy}}^*(201\beta)$	25	2.24	552	0.0496	2.17	520
	$\pi_{\text{im}}^*(199\alpha) \rightarrow \pi_{\text{terpy}}^*(204\alpha)$	15					
	$d_{xy}(197\alpha) \rightarrow \pi_{\text{terpy}}^*(201\alpha)$	7					
	$d_{xz}(195\beta) \rightarrow \pi_{\text{im}}^*(199\beta)$	46					
T ₃₀	$\pi_{\text{im}}(198\beta) \rightarrow \pi_{\text{terpy}}^*(202\beta)$	18	2.41	515	0.0644	2.88	
	$d_{xz}(198\alpha) \rightarrow \pi_{\text{terpy}}^*(202\alpha)$	11					
	$d_{xz}(195\beta) \rightarrow \pi_{\text{im}}^*(199\beta)$	33					
T ₃₁	$\pi_{\text{im}}(198\beta) \rightarrow \pi_{\text{terpy}}^*(202\beta)$	24	2.44	509	0.0446	3.16	
	$d_{xz}(198\alpha) \rightarrow \pi_{\text{terpy}}^*(202\alpha)$	20					
	$\pi_{\text{terpy}}^*(200\alpha) \rightarrow d_{x^2-y^2}(217\alpha)$	9					
T ₄₁	$\pi_{\text{im}}^*(199\alpha) \rightarrow \pi_{\text{im}}^*(210\alpha)$	9	2.75	450	0.0410	2.26	
	$\pi_{\text{terpy}}^*(200\alpha) \rightarrow \pi_{\text{delocal}}^*(212\alpha)$	6					
	$\pi_{\text{im}}(194\beta) \rightarrow \pi_{\text{im}}^*(199\beta)$	46					
T ₄₅	$\pi_{\text{terpy}}^*(200\alpha) \rightarrow \pi_{\text{delocal}}^*(211\alpha)$	29	2.87	432	0.0524	2.17	
	$\pi_{\text{terpy}}^*(200\alpha) \rightarrow \pi_{\text{delocal}}^*(212\alpha)$	6					
	$\pi_{\text{terpy}}^*(200\alpha) \rightarrow \pi_{\text{delocal}}^*(211\alpha)$	27					
T ₄₆	$\pi_{\text{im}}(194\beta) \rightarrow \pi_{\text{im}}^*(199\beta)$	26	2.87	432	0.0376	2.22	
	$\pi_{\text{terpy}}^*(200\alpha) \rightarrow \pi_{\text{delocal}}^*(212\alpha)$	21					

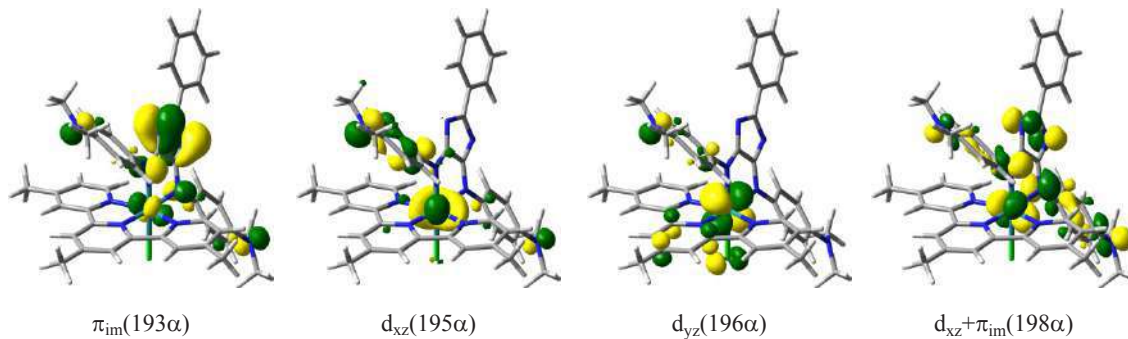
T ₄₈	$\pi_{\text{terpy}}^*(200\alpha) \rightarrow d_{z^2}(213\alpha)$	29	2.94	422	0.0562	2.24
	$\pi_{\text{terpy}}^*(200\alpha) \rightarrow \pi_{\text{terpy}}^*(215\alpha)$	8				
T ₄₉	$\pi_{\text{terpy}}^*(200\alpha) \rightarrow \pi_{\text{terpy}}^*(215\alpha)$	29	2.96	419	0.0746	2.44
	$\pi_{\text{terpy}}^*(200\alpha) \rightarrow \pi_{\text{delocal}}^*(212\alpha)$	13				

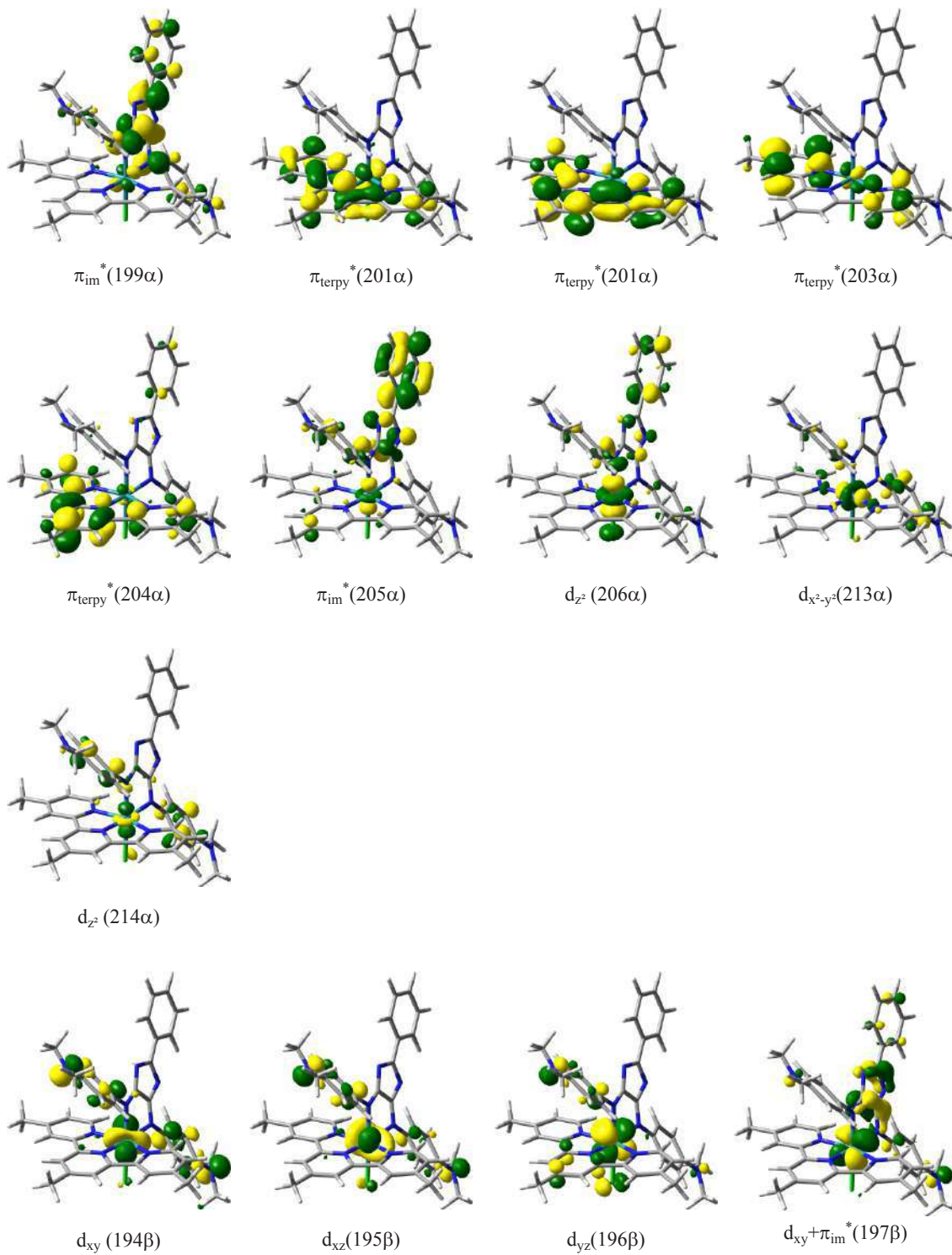
Table S2. Molecular orbitals involved in the main transitions of the bright electronic excited states of the non-reduced (singlet) and the single reduced (doublet) species of RuImN(CH₃)₂.

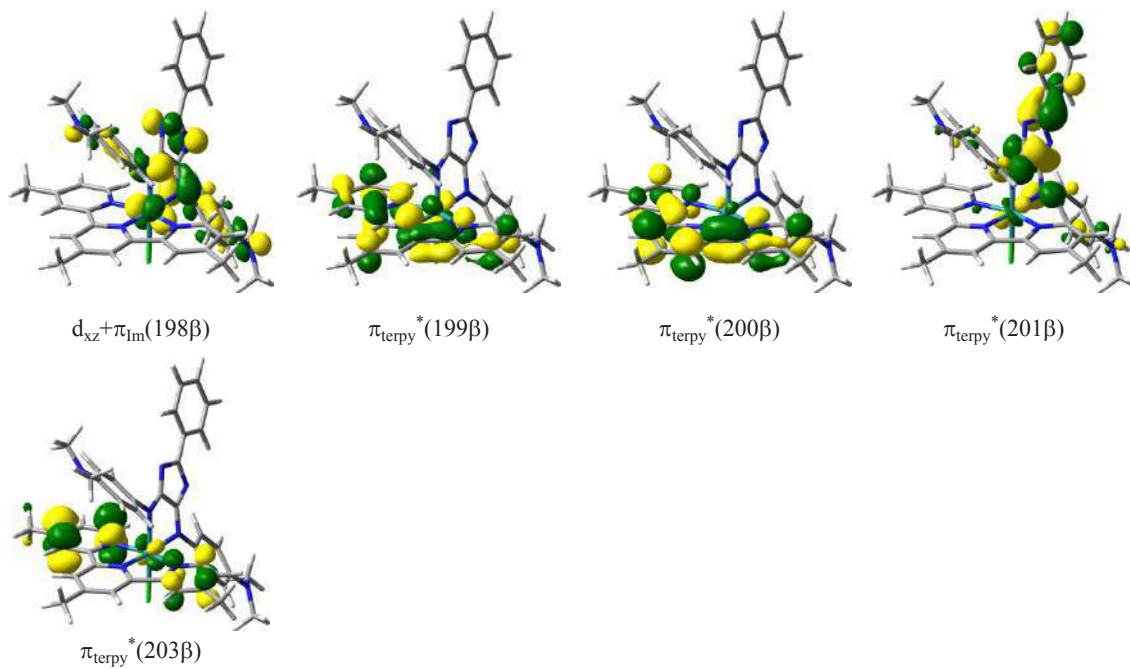
Non-reduced singlet



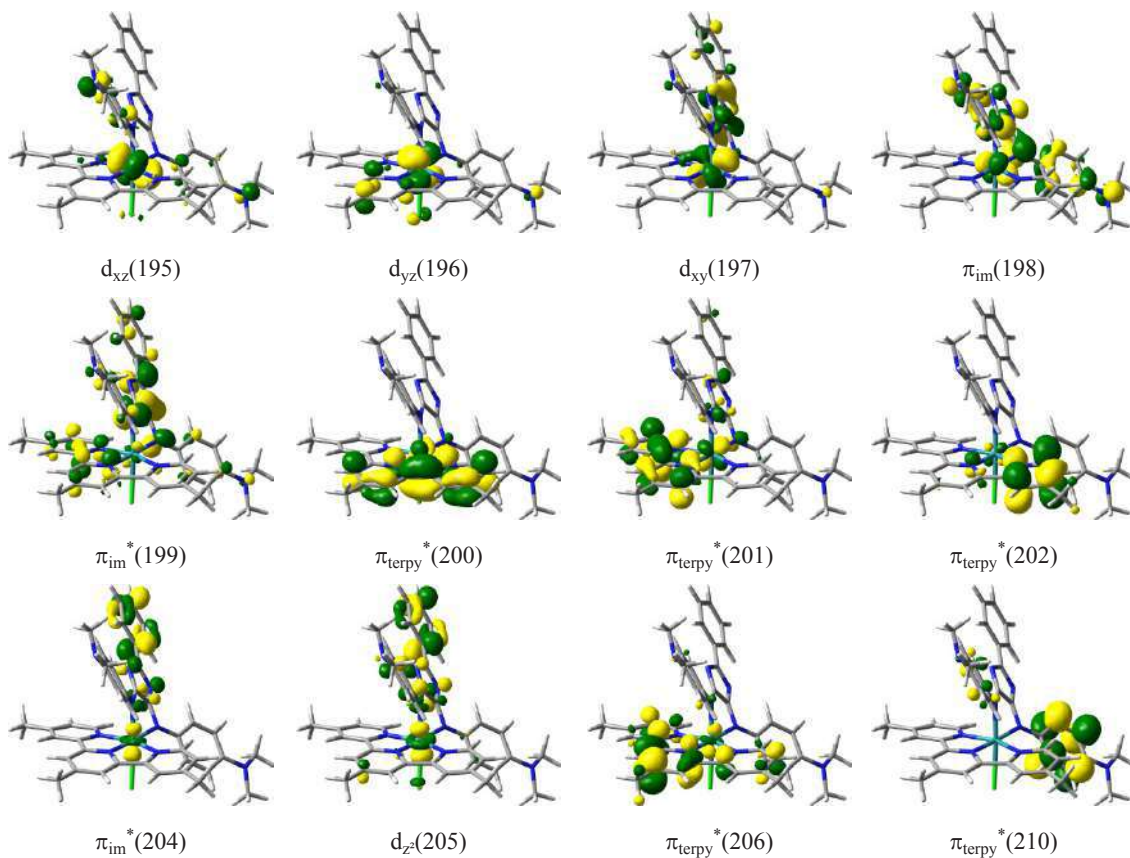
Single reduced doublet



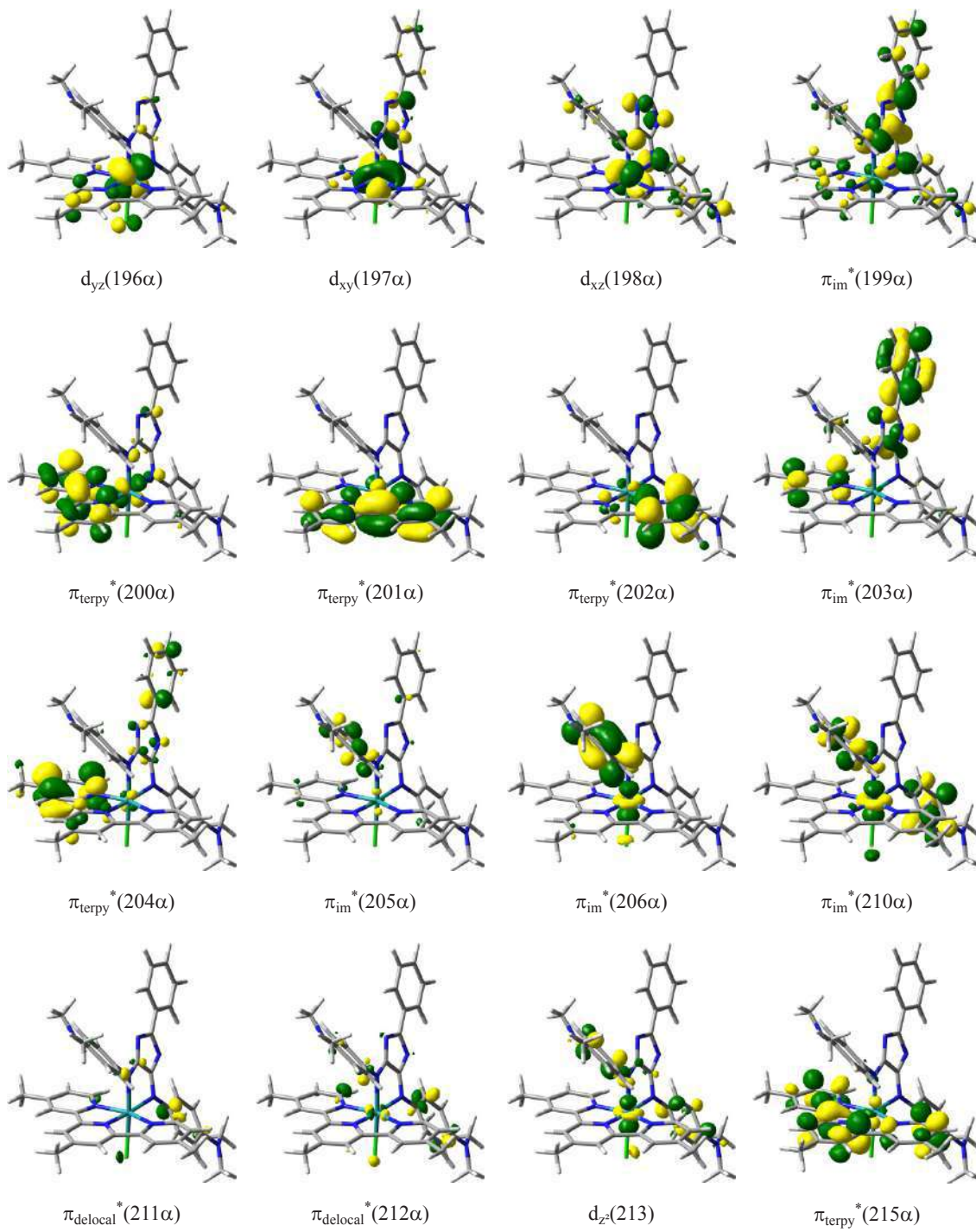


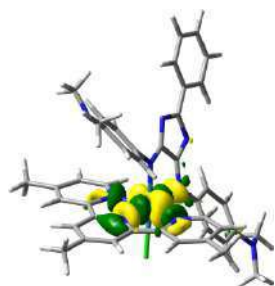


Double reduced singlet

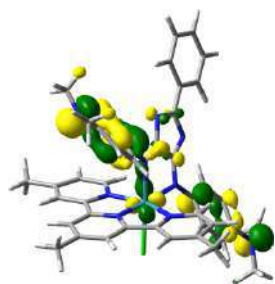


Double reduced triplet

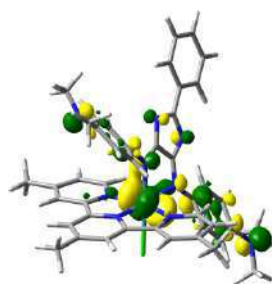




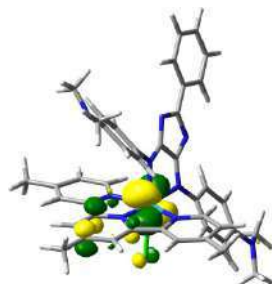
$d_{x^2-y^2}(217)$



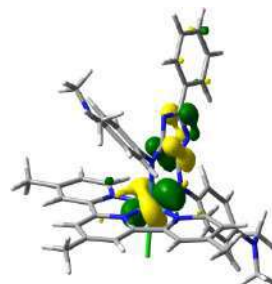
$\pi_{im}(194\beta)$



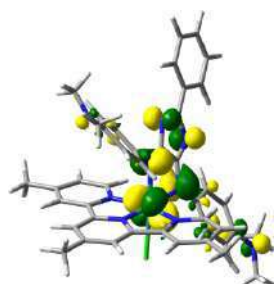
$d_{xz}(195\beta)$



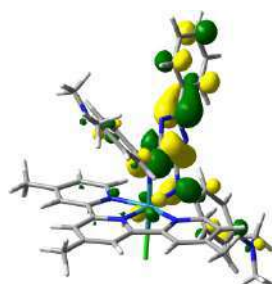
$d_{yz}(196\beta)$



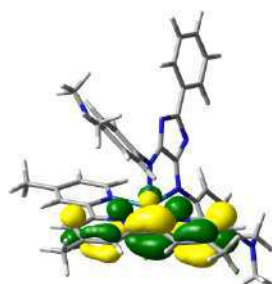
$d_{xy}(197\beta)$



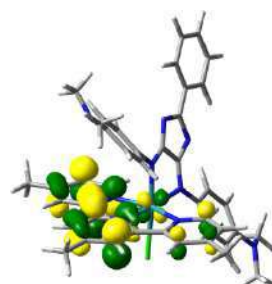
$\pi_{im}(198\beta)$



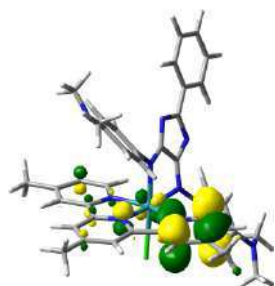
$\pi_{im}^*(199\beta)$



$\pi_{terpy}^*(200\beta)$



$\pi_{terpy}^*(201\beta)$



$\pi_{terpy}^*(202\beta)$

Table S3. Assignment of the vibrational frequencies (cm^{-1}) and calculated relative RR intensities (I_{rel}) for the non-reduced, the single reduced and double reduced (triplet) complex.

Non-reduced singlet

mode	$\tilde{\nu}_{scal} / \text{cm}^{-1}$	$\tilde{\nu}_{exp} / \text{cm}^{-1}$	I_{rel}
157(im)	1119.3		0.06
167(im)	1179.6		0.07
168(terpy)	1180.2	1185.1	0.09
172(im)	1234.0	1241.8	0.06
186(terpy)	1322.5	1310.8	0.32
189(im)	1336.5	1327.7	0.26
191(im)	1349.3		0.05
192(im)	1360.1	1355.6	0.07
193(im)	1378.5		0.91
194(terpy)	1391.0		0.07
197(terpy)	1399.5		0.12
204(terpy)	1437.1		0.06
217(terpy)	1467.1		0.13
218(terpy)	1473.4	1473.5	0.07
222(im)	1492.4	1491.3	0.39
228(terpy)	1548.9	1542.1	0.24
232(im)	1563.7	1554.3	1.00
233(im)	1577.1		0.08
236(terpy)	1609.3	1607.3	0.50

Single reduced doublet

mode	$\tilde{\nu}_{scal} / \text{cm}^{-1}$	$\tilde{\nu}_{exp} / \text{cm}^{-1}$	I_{rel}
144(terpy)	1022.4		0.05
168(im)	1180.1		0.10
181(terpy)	1277.5		0.06
186(terpy)	1313.9		0.12
193(im)	1376.2		0.26
194(terpy)	1389.0		0.31
197(terpy)	1398.9		0.27
206(terpy)	1451.2		0.12
218(terpy)	1467.2		0.06

220(im)	1482.3		0.42
224(im)	1498.1		0.14
226(im)	1503.3		0.05
229(terpy)	1519.3		0.27
230(terpy)	1540.4		0.32
235(im)	1590.3		0.07
236(terpy)	1602.5		1.00
239(terpy)	1611.8		0.10
240(im)	1612.3		0.09
Double reduced triplet			
mode			
142	1001.0		0.20
143	1009.9		0.06
144(terpy)	1014.7		0.06
164(im)	1146.4		0.05
165(terpy)	1150.0		0.07
168(terpy)	1172.1		0.19
175(im)	1275.7		0.11
177(terpy+im)	1251.7		0.05
179(im)	1265.9		0.06
181(im)	1280.3		0.06
182(terpy)	1285.6		0.07
184(terpy)	1300.7		0.05
185(terpy+im)	1301.7	1315.1	0.10
193(terpy)	1366.3		0.06
194(im)	1385.0		0.05
206(terpy)	1451.5		0.05
220(terpy)	1479.0		0.08
221(terpy)	1482.0	1476.2	0.46
228(terpy)	1503.0	1503.7	1.00
233(terpy)	1542.9		0.27
236(terpy)	1580.4		0.28
237(im)	1589.1		0.61
238(terpy)	1606.0		0.14

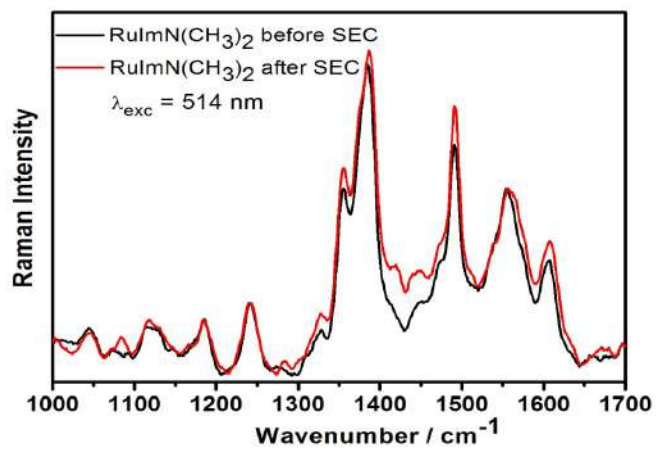
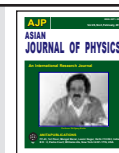


Fig S1. RR spectra of **RuImN(CH₃)₂** excited at 514 nm before applying potential (black curve) and after recovery upon reoxidation of the reduced species (red curve). Only minor alterations in the spectra prove the general reversibility and recovery upon reoxidation of the reduced **RuImN(CH₃)₂**.



Dehydration of 3-octanol studied by 2D Raman, IR and NMR hetero correlation spectroscopy

Robby Fritzscha, Robert Geitnera, Thomas W Bocklitza, Benjamin Dietzek^{a,c},

Micheal Schmitt^a and Jürgen Popp^{a,b,c}

^a*Institute for Physical Chemistry and Abbe Center of Photonics,*

Friedrich Schiller University Jena, Helmholtzweg 4, 07743, Jena, Germany.

^b*Jena Center of Soft Matter (JCSM), Friedrich Schiller University Jena, Philosophenweg 7, 07743, Jena, Germany*

^c*Leibniz Institute for Photonic Technology (IPHT) Jena, Albert-Einstein-Str. 9, 07745, Jena, Germany.*

(Dedicated to Professor Wolfgang Kiefer on the occasion of his 75th birthday)

2D correlation spectroscopy is a useful technique for analyzing chemical reactions. We studied the acid catalyzed dehydration of 3-octanol at 150 °C with FT Raman, FT-ATR-IR and ¹H NMR and evaluated the use of 2D correlation spectroscopy in particular the correlation of spectroscopic data from different methods with one another. This 2D hetero correlation approach proved to be useful in validating the signal assignment but otherwise limited in use. We could also show that all four possible octene isomers are forming over the course of the reaction. © Anita Publications. All rights reserved.

Keywords: 2D correlation spectroscopy, FT-Raman, FT-ATR-IR and ¹H NMR

1 Introduction

Modern chemistry relies to a great extent on spectroscopic methods like e.g. infrared absorption (IR), Raman or nuclear magnetic resonance (NMR) spectroscopy to study complex molecules or chemical reactions. Every spectroscopic method has its own advantages and disadvantages, thus it is often advantageous to combine the results of different spectroscopic approaches. Nevertheless, the exact identification of molecules and the correct assignment of all spectroscopic signals is very often rather difficult. One problem in this context is the finite bandwidth of spectroscopic signals and that is why it is difficult to separate strongly overlapping signals.

One approach to overcome this difficulty and to combine different spectroscopic methods effectively represents two-dimensional (2D) correlation spectroscopy invented by Noda in 1986 [1] and later generalized in 1993 [2]. In general 2D correlation spectroscopy allows the correlation of an external perturbation with the spectroscopic information. In this way it is possible to follow even small changes introduced for example through a chemical reaction or an elevated temperature.

2D correlation is based on the Fourier- or Hilbert-Noda transformation of a perturbation-dependent dataset [2-6]. This correlation analysis emphasizes changes from a predefined reference state. The results of the 2D correlation analysis are the so called synchronous and asynchronous correlation spectra, which can be interpreted using the Noda rules [7].

While 2D correlation spectroscopy started with the homo correlation of the same dataset with itself [3, 8], today it is possible to correlate different spectroscopic methods with each other [9,10]. By the application of hetero 2D correlation spectroscopy it becomes possible to follow chemical processes, which otherwise cannot be studied in such detail [11,12]. For example Yamasaki and Morita studied the epoxy

Corresponding author :

e-mail: juergen.popp@uni-jena.de (Juergen Popp)

curing reaction between diglycidyl ether bisphenol A and 1,6-diaminohexane combining MIR and NIR spectroscopy [13]. It is important to note that the perturbation must be the same, if different spectroscopic techniques are correlated with each other [14].

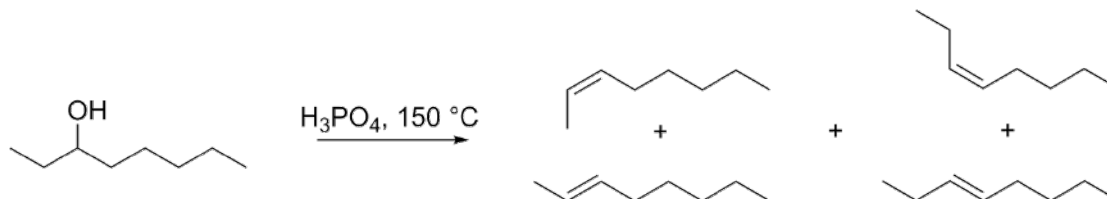


Fig 1. Reaction scheme of the acid catalyzed dehydration of 3-octanol with phosphoric acid. The products are (Z) 2-octene (top left), (E) 2-octene (bottom left), (Z) 3-octene (top right) and (E) 3-octene (bottom right).

Here, we were interested in using a 2D hetero correlation approach to transfer the information derived from one spectroscopic method to another one in order to be able to interpret the spectroscopic results of the different spectroscopic methods unambiguously. We have chosen the acid catalyzed dehydration of 3-octanol as an example reaction. The products of this chemical reaction are 2- and 3-octenes in their *E* and *Z* configurations (see Fig 1). Thus, this example reaction offers the possibility to address three questions:

1. Is it possible to monitor the reaction from octanol to octene ?
2. Is it possible to differentiate between the two resulting regioisomers of octene?
3. Is it possible to distinguish between the *E* and *Z* configurations ?

We used Raman, IR and NMR spectroscopy to answer these three questions, because these are spectroscopic techniques, which are commonly used in chemistry to study chemical reactions. Furthermore, all three methods can be used without requiring special sample preparation steps, which is necessary for 2D hetero correlation spectroscopy. In the following, we will present the results of 2D Raman, IR and NMR homo and hetero correlation on the acid catalyzed dehydration of 3-octanol with the reaction time as the perturbation variable.

2 Experimental

2.1 Dehydration of 3-octanol

All chemicals were purchased from commercial suppliers (Alfa Aesar, Fluka and Sigma Aldrich) and used without further purification.

3-octanol (10 mL, 8.18 g, 62.8 mmol) was heated with phosphoric acid (85 %, 2.39 mL, 4.09 g, 41.7 mmol) to 150 °C for 145 minutes. After 10 minutes and every 15 minutes thereafter 1 mL of the reaction solution was removed, neutralized with sodium carbonate and cooled to 5 °C to inhibit the acid catalyzed water addition. Ten samples were generated by this way. The overall conversion after 145 minutes was 36 % as determined by ¹H NMR spectroscopy.

2.2 Spectroscopic methods

FT-Raman spectra were recorded using a commercial MultiRam RFS27 spectrometer equipped with a RAM-II Raman module (Bruker, Germany). A Nd:YAG-Laser (KLAASSTECH Laser, DENICAFC LC-3/40, Karpushko Laser Technologies GmbH, Germany) operated at 1064 nm was used as excitation source with a power of 1000 mW. The resolution was 4 cm⁻¹. FT-ATR-IR spectra were recorded on a Varian 670 -IR spectrometer (Varian, now Agilent Technologies, USA) equipped with a ZnSe crystal (PIKE MIRacle, USA). The resolution was 4 cm⁻¹. A background spectrum consisting of 160 single scans was recorded beforehand.

For the FT-Raman measurements 750 μL of the reaction solution was mixed with 50 μL of deuterated chloroform and measured in a cuvette. For every sample 16 FT-Raman spectra consisting of 50

single scans were collected. The same samples were used for FT ATR-IR measurements. For every sample 8 FT-IR spectra consisting of 20 single scans were recorded.

A 400 MHz Avance III NMR spectrometer (Bruker, Germany) was used to record the ^1H - NMR spectra. For the NMR measurements 30 μL reaction solution and 570 μL deuterated chloroform were mixed and for every sample 8 ^1H - NMR spectra each consisting of 4 single scans were recorded. The different measurement concentrations became necessary due to the high solvent signal in the vibrational spectra, while the small content of DCCl_3 was not sufficient for the calibration of the NMR spectrometer, which is based on the residual solvent signal from DCCl_3 . While the samples are not strictly the same, hetero correlation can still be applied because the reaction time (i.e. the external perturbation) is still the same for every sample and the changes induced from the different concentrations should be much smaller than those induced by the chemical reaction itself.

2.3 Data preprocessing

The data preprocessing was done using R (3.1.2) [15] and the software packages sfsmisc, KernSmooth, Peaks, Hmisc, doSNOW, doParallel, rgl, fields and mmand. In addition the ^1H - NMR spectra were frequency calibrated using the RAFFT algorithm of SpecAlign (v2.4.1) [16].

First, the data were restricted to the regions of interest (180-1800 cm^{-1} for FT-Raman, 600-1800 cm^{-1} for FT-IR and 0-5.5 ppm for ^1H NMR). The data were background corrected using a SNIP algorithm (iterations = 100 for Raman and NMR, iterations = 10 for IR). The strong background correction for the IR data also removes the broad water bands, which would otherwise dominate the correlation spectra. Furthermore, all spectra were area normalized to the CH deformation vibration bands at 1443 cm^{-1} for FT-Raman and 1462 cm^{-1} for FT-IR as well as to the CH_3 and CH_2 signals between 0.75 and 2 ppm for ^1H - NMR spectra. These signals remain almost constant in intensity throughout the dehydration reaction because they mostly stem from alkyl chains that do not take part in the reaction. To increase the signal to noise ratio all spectra were summed up for each reaction time after preprocessing. The spectra were 2D correlated using a self-written R-script based on the Fourier-transform approach. The mean spectra were used as references. The 2D correlation spectra were created by an arbitrary selection of the contour levels. The contour levels around 0 were omitted because they only contain noise contributions, thus only the highest peaks in the selected spectral regions are shown.

3 Results and Discussion

3.1 FT-Raman, ^1H - NMR and FT- IR spectra

The FT-Raman spectra during the dehydration of 3-octanol are displayed in Fig 2a. The spectra exhibit big and small changes throughout the course of the reaction. The biggest change is the formation of two C=C stretching vibrations at 1658 and 1671 cm^{-1} (*Z* and *E* configurations, respectively) while the band at 895 cm^{-1} (C-C-O vibration) is decreasing in intensity [17]. It can be concluded that the dehydration of 3-octanol is taking place and that (*E*)- and (*Z*) octenes are formed.

The corresponding ^1H - NMR spectra are shown in Fig 2c. An intensity decrease at 1.4 and 3.43 ppm coupled with an intensity increase at 1.9 and 5.32 ppm can be observed. These signals stem from the methylene groups close to the HCOH fragment (1.4 ppm), the hydrogen atom bound to the chiral carbon atom in 3-octanol (3.43 ppm), the methylene groups close to the newly formed double bond in 2 and 3 positions (1.9 ppm), the methyl group close to the newly formed double bond in 2 position (1.51 ppm) and the hydrogen atoms directly located at the new C=C bond (5.32 ppm) [18,19]. The ^1H - NMR signal of the OH group is shifting between 2 and 3 ppm because 3-octanol and water form hydrogen bonds depending on the concentration. *Z* and *E* configurations can usually be studied by the coupling constant $3J$ between the two alkenyl hydrogen atoms [20], but in our case the signals overlap, thus it is impossible to extract

a coupling constant. 2- and 3- octenes can be distinguished by the methyl and methylene groups close to the double bond, because these groups are slightly shifted downfield due to their proximity to the alkene functionality. From the emerging signals at 1.51 and 1.9 ppm it can be concluded that in addition to the two configuration isomers both regioisomers of octene are forming.

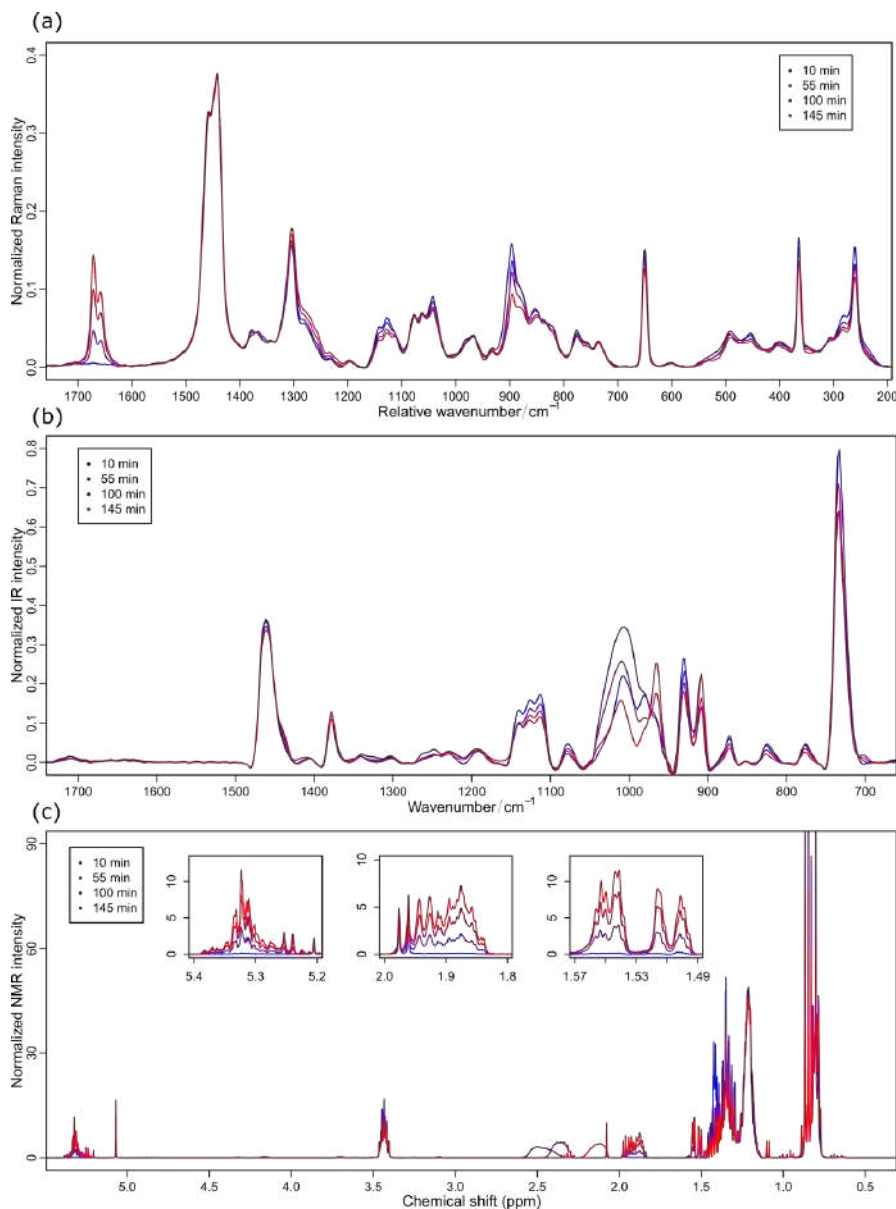


Fig 2. Spectroscopic data for the dehydration of 3-octanol at four selected reaction times (10, 55, 100 and 145 minutes): (a) FT-Raman spectra in the wavenumber region from 200-1750 cm⁻¹. The Raman spectra area normalized to the band at 1443 cm⁻¹, (b) FT-ATR-IR spectra in the wavenumber region from 700-1700 cm⁻¹. (area normalized to the band at 1462 cm⁻¹), (c) ¹H-NMR spectra in the region of 0.5-5.5 ppm (area normalized to the hydrogen signals between 0.75 and 2.0 ppm). For details see text.

The FT-IR spectra from the reaction solution (see Fig 2b) show large contributions from water, which is formed during the dehydration reaction. Thus, a background correction to remove the otherwise dominating influence of water was necessary. A comparison between FT-IR spectra with weak and strong background corrections can be found in Fig 3. The two C=C stretching vibrations cannot be seen in the FT-IR spectra. The strongest changes in the FT-IR spectra are observed in the wavenumber region around 1000 cm^{-1} , which contains contributions from water. The decreasing band at 1005 cm^{-1} may stem from the CO stretching vibration, while the band at 982 cm^{-1} is due to a CH deformation vibration of (*E*) alkenes [17]. The FT-IR spectra are difficult to interpret due to the contribution of water.

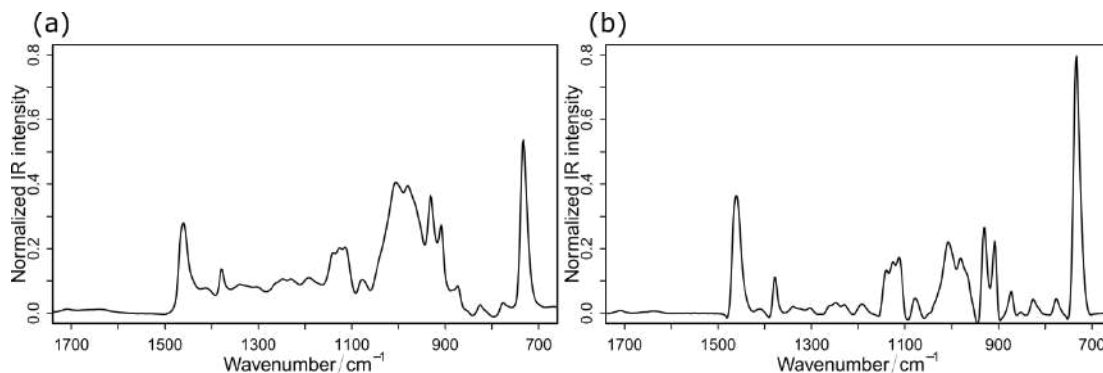


Fig 3. Comparison between FT-ATR-IR spectra of the dehydration of 3-octanol after 10 minutes reaction time with weak (a, iterations = 100) and strong (b, iterations = 10) background correction. The SNIP algorithm removes the dominating contribution from water at around 1000 cm^{-1} in case of the strong background correction.

3.2 Two-dimensional homo correlation spectra

A first step to obtain more information about the dehydration of 3-octanol are the 2D Raman, IR and NMR homo correlation spectra where one dataset is correlated with itself. In Fig 4a the 2D Raman homo correlation spectrum is shown. The negative crosspeaks in the synchronous spectrum at $\Phi(1671,895)$ and $\Phi(1658,895)$ reveal that the bands at 1671 and 1658 cm^{-1} are increasing with time while the band at 895 cm^{-1} is decreasing in intensity. The examination of all crosspeaks shows that the bands at 895 , 1040 , 1127 and 1466 cm^{-1} are decreasing in intensity with time while the Raman bands at 1223 , 1263 , 1295 , 1379 , 1434 , 1658 and 1671 cm^{-1} are increasing in intensity. The two C-H deformation vibration bands at 1434 and 1466 cm^{-1} can now be assigned to octene and 3-octanol, respectively. The correlation pattern proves that the dehydration of 3-octanol forms octene. The synchronous 2D IR and NMR homo correlation spectra (see Figs 4c and 4d) show the same behavior as the 2D Raman homo correlation spectra and do not contain any new information.

The asynchronous 2D Raman homo correlation spectrum on the other hand reveals with its two crosspeaks at $\Psi(1658,1671)$ and $\Psi(1671,1658)$ (see Fig 4b) that the band at 1658 cm^{-1} is formed before the band at 1671 cm^{-1} . Because these two bands correspond to the *Z* and *E* configurations of octene it can be concluded that (*Z*) octene is formed predominantly at the start of the reaction while (*E*) octene emerges more towards the end. This observation is in line with what would be expected that the kinetic product (in this case (*Z*) octene) is forming at the start of the reaction while the thermodynamic product (in this case (*E*) octene) develops after longer periods of reaction time.

3.3 Two-dimensional hetero correlation spectra

The normal one-dimensional FT-Raman, FT-IR and ^1H -NMR spectra and the corresponding 2D homo correlation spectra could already prove that the dehydration of 3-octanol to octene is taking place, that all four isomers of octene are formed and that (*Z*) octene emerges before (*E*) octene. In the following we will have a look at the 2D hetero correlation spectra.

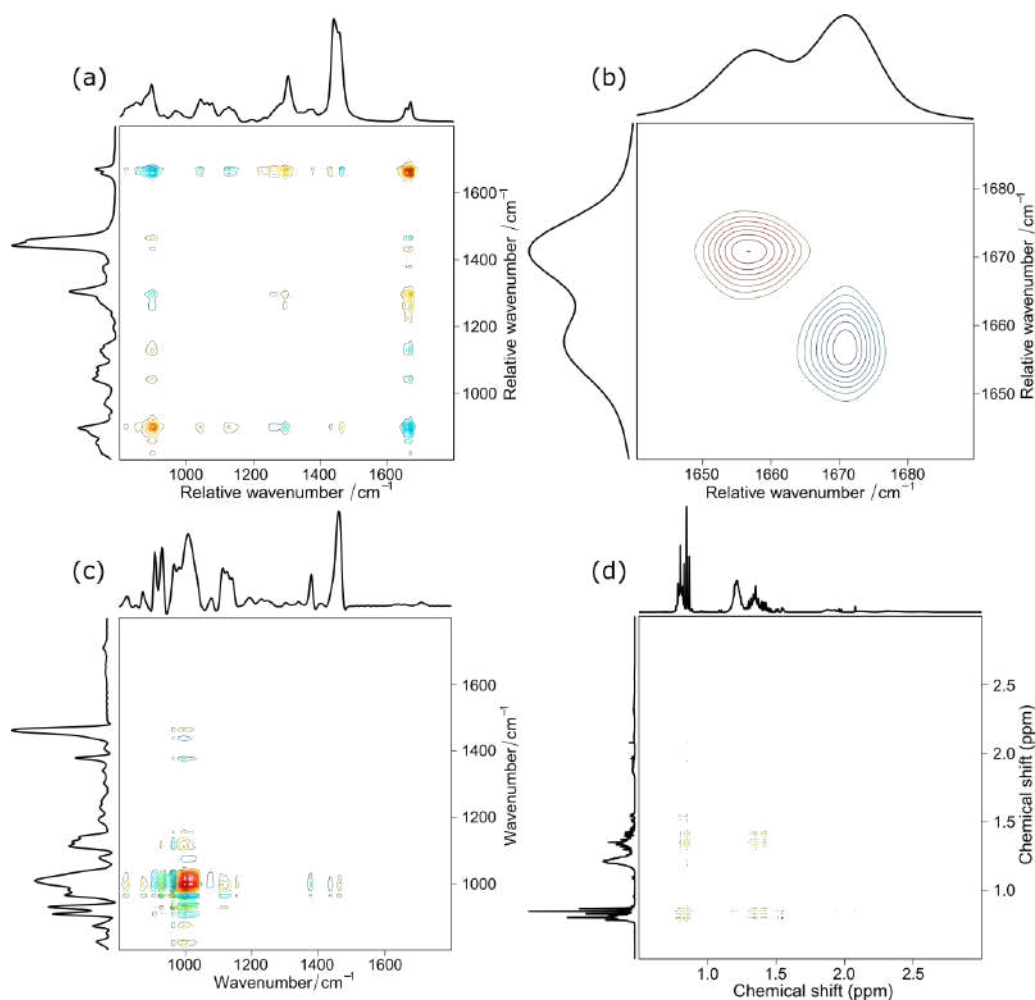


Fig 4. 2D homo correlation spectra of the dehydration of 3-octanol with the reaction time as perturbation from 10 to 145 minutes in steps of 15 minutes. The mean spectra were used as reference spectra. Red color indicates positive peaks, while blue color shows negative ones. (a) Synchronous 2D FT- Raman homo correlation spectrum in the wavenumber region from 800-1800 cm^{-1} . (b) Asynchronous 2D FT- Raman homo correlation spectrum in the wavenumber region from 1640-1690 cm^{-1} . (c) Synchronous 2D FT- IR homo correlation spectrum in the wavenumber region from 800-1800 cm^{-1} . (d) Synchronous 2D ^1H NMR homo correlation spectrum in the ppm region from 0.5-3 ppm. For details see text.

The synchronous 2D Raman-IR correlation spectrum is shown in Fig 5a. As expected from the 2D homo correlation the crosspeaks from the IR bands at 1000 cm^{-1} dominate the spectrum. The negative crosspeak at $\Phi(1660,1005)$ and the positive crosspeak at $\Phi(1660,982)$ indicate once again that the alcohol is consumed and the alkene is formed. From the crosspeaks at $\Phi(1660,1464)$ and $\Phi(1660,1437)$ (Fig 5b) it is possible to deduce that the C-H deformation vibrations in the IR spectra consist of two bands stemming from 3-octanol (1464 cm^{-1}) and octene (1437 cm^{-1}). This is in line with the assignments made previously from the synchronous 2D Raman homo correlation spectrum. Unfortunately the 2D Raman-IR correlation spectrum does not reveal any new details on the isomerisation of octene.

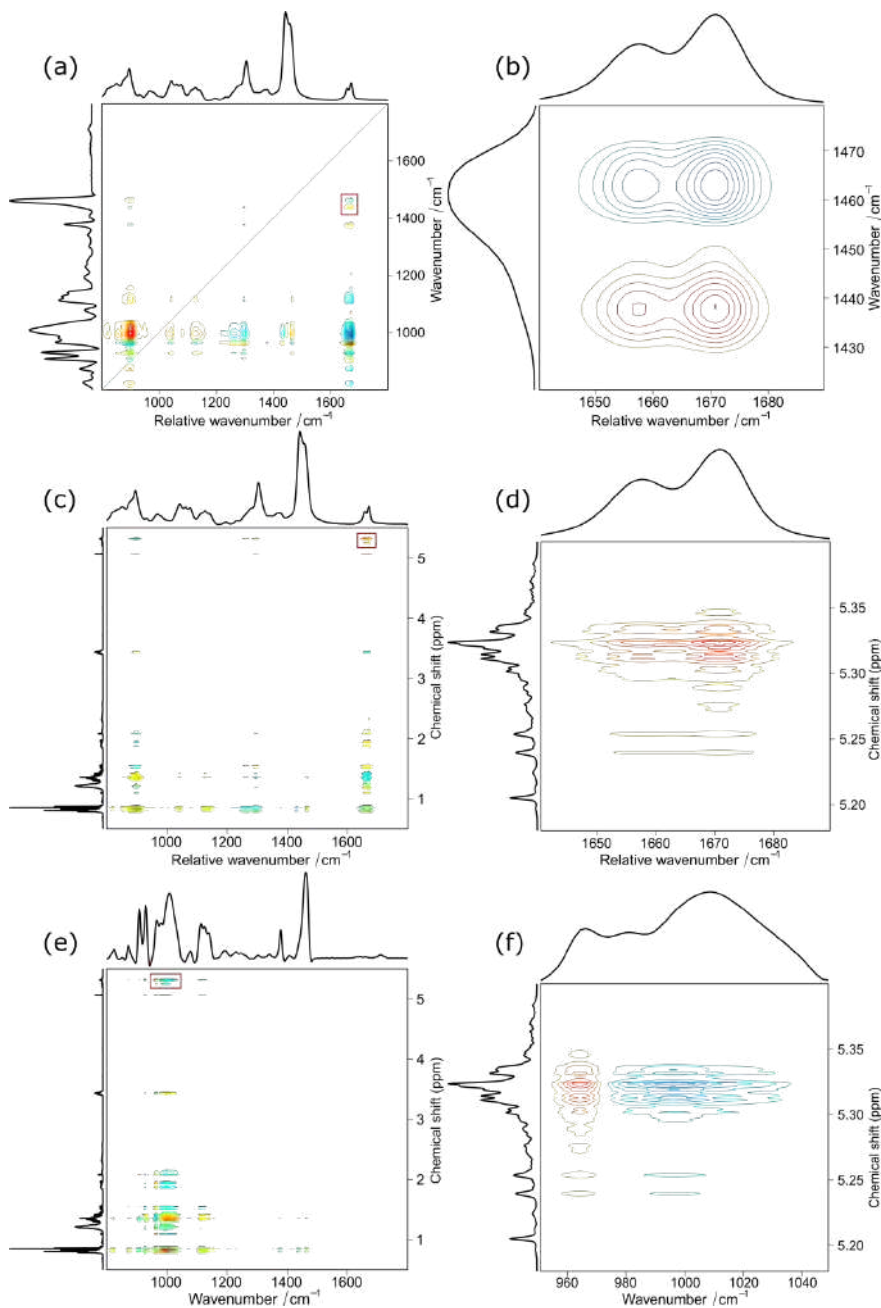


Fig 5. 2D hetero correlation spectra of the dehydration of 3- octanol with the reaction time as perturbation from 10 to 145 minutes in steps of 15 minutes. The mean spectra were used as reference spectra. Red color indicates positive peaks, while blue color shows negative ones. (a) Synchronous 2D Raman IR correlation spectrum. (b) Inset from (a) showing the correlation between $\nu(\text{C}=\text{C})$ and $\delta(\text{CH})$. (c) Synchronous 2D Raman 1H NMR correlation spectrum. (d) Inset from (c) showing the correlation between $\nu(\text{C}=\text{C})$ and $\text{H}-\text{C}=\text{C}-\text{H}$. (e) Synchronous 2D IR 1H NMR correlation spectrum. (f) Inset from (e) showing the correlation between $\delta(\text{C}=\text{C H})$ and $\text{H}-\text{C}=\text{C}-\text{H}$. For details see text.

The synchronous 2D Raman NMR and the synchronous 2D IR- NMR correlation spectra (see Figs 5c and 5e) confirm the previously made signal assignment. Especially the positive crosspeaks at $\Phi(1667,1.51)$, $\Phi(1667,1.54)$, $\Phi(1667,1.88)$, $\Phi(1667,1.93)$, $\Phi(1667,5.25)$ and $\Phi(1667,5.32)$ (Raman-NMR) confirm that the corresponding NMR signals belong to octene. A close look at the crosspeak at $\Phi(1667,5.32)$ (see Fig 5d) shows that it is unfortunately not possible to disentangle the overlapping NMR signals by using the information obtained from the FT- Raman spectra. The same holds true for the synchronous IR-NMR correlation spectrum and the crosspeaks at $\Phi(995,5.32)$ and $\Phi(964,5.32)$ (see Fig 5f).

Taken together the 2D hetero correlation spectra can be used to validate the signal assignment for the different spectroscopic methods, but they do not grant any new insights that couldn't otherwise be acquired through normal one-dimensional spectra or two-dimensional homo correlation spectroscopy.

Based on the spectroscopic signal assignment a simple calculation of the isomer ratio of octene after 145 minutes reaction time can be performed. The ratio between the *Z* and *E* configurations can be calculated from the two Raman bands at 1658 and 1671 cm^{-1} with an integration of both bands assuming that both vibrations have an equal Raman scattering cross section:

$$\text{ratio}_{(E)-(Z)} = \frac{n_{(E)\text{-octene}}}{n_{(Z)\text{-octene}} + n_{(E)\text{-octene}}} = \frac{A_{1671}}{A_{1658} + A_{1671}}$$

Based on the Raman spectra after 145 minutes roughly 59 % (*E*) octene and 41 % (*Z*) octene is formed. By integrating the ^1H -NMR signals at 1.51, 1.54 and 1.9 ppm, which belong to the methyl and methylene groups close to the double bond the ratio between 2- and 3- octenes can be calculated as follows:

$$\text{ratio}_{2-3} = \frac{n_{2\text{-octene}}}{n_{3\text{-octene}} + n_{2\text{-octene}}} = \frac{\frac{n_{\text{CH}_3}}{3}}{\frac{n_{3\text{-CH}_2}}{4} \frac{n_{\text{CH}_3}}{3}} = \frac{(A_{1.51} + A_{1.54})}{0.75 \cdot A_{1.9} + 0.5 \cdot (A_{1.51} + A_{1.54})}$$

Thus, based on the ^1H - NMR spectrum, 60 % 2-octene and 40 % 3-octene arises. Combining both ratios derived from the Raman and ^1H -NMR spectra the dehydration of 3- octanol with phosphoric acid at 150 °C yields: 35 % (*E*) 2-octene, 24 % (*Z*) 2- octene, 24 % (*E*) 3-octene and 17 % (*Z*) 3-octene after 145 minutes.

4 Conclusion

With the presented 2D correlation approach it is possible to analyze the threefold analytical problem that the acidcatalyzed dehydration of 3octanol provides. We could identify the formation of all four octene isomers with a product ratio of 2.14 : 1.47 : 1.47 : 1 for (*E*)2-octene : (*Z*)2-octene : (*E*)3-octene : (*Z*)3-octene.

The use of 2D correlation spectroscopy proved to be useful in allowing for a deeper insight into the analytical question compared with the normal one dimensional approach would have provided. The 2D homo Raman correlation spectrum showed that (*Z*)-octene is forming before (*E*)-octene. The 2D hetero correlation spectra enabled us to validate the different signal assignments made within each method. In general it is possible to transfer information obtained from one spectroscopic method to another one, although the 2D hetero correlation could not answer unsolved problems like disentangling the strongly overlapping NMR signals. In general the information gained from 2D hetero correlation spectroscopy is limited when not applied to a specific analytical problem.

5 Acknowledgement

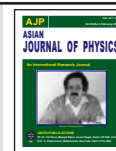
We would like to thank the Deutsche Forschungsgemeinschaft (DFG) for funding the priority program SPP 1568 "Design and Generic Principles of Self-healing Materials" and the project PO563/25-2,

and DI1517/9-1 therein. Furthermore, we would like to thank Dr. Peter Bellstedt and Bärbel Rambach for recording the ¹H-NMR spectra and Moritz Klein for assistance while measuring the FT-ATR-IR spectra.

References

1. Noda I, *Bull Am Phys Soc*, 31 (1986)520-524.
2. Noda I, *Appl Spectrosc*, 47(1993)1329-1336.
3. Noda I, *J Am Chem Soc*, 111(1989)8116-8118.
4. Noda I, *Appl Spectrosc*, 44(1990)550-561.
5. Noda I, *Appl. Spectrosc*, 54(2000)994-999.
6. Noda I, *Vib Spectrosc*, 60(2012)146-153.
7. Noda I, *J Mol Struct*, 799(2006)41-47.
8. Geitner R, Kötteritzsch J, Siegmann M, Bocklitz T, Hager M, Schubert U S, Graefe S, Dietzek B, Schmitt M, Popp J, *Phys Chem Chem Phys*, 17(2015)22587-22595.
9. Noda I, *Chemtracts: Macromolecular Chemistry*, 1(1990)89-105.
10. Barton F E, Himmelsbach D S, Duckworth J H, Smith M J, *Appl Spectrosc*, 46(1992)420-429.
11. Ryu S R, Bae W M, Hong W J, Ihn K J, Jung Y M, *Vib Spectrosc*, 60(2012)168-172.
12. Sovová Ž, Kopecký V, Pazderka T, Hofbauerová K, Rozbeský D, Vaněk O, Bezouška K, Ettrich R, *J Mol Model*, 17(2011)1353-1370.
13. Yamasaki H, Morita S, *J Appl Polym Sci*, 119(2011)871-881.
14. Noda I, *Chin Chem Lett*, 26(2014)167-172.
15. R Core team, R: A Language and Environment for Statistical Computing. (R Foundation for Statistical Computing, Wien, Austria), 2014.
16. Wong J W H, Cagney G, Cartwright H M, *Bioinformatics*, 21(2005)2088-2090.
17. Socrates G, *Infrared and Raman characteristic group frequencies*, (John Wiley & Sons, West Sussex), 2007.
18. Larsen C R, Erdogan G, Grotjahn D B, *J Am Chem Soc*, 136(2014)1226-1229.
19. SDBSWeb: Spectral Database for Organic Compounds. National Institute of Advanced Industrial Science and Technology (AIST), date of access: 13.10.2015.
20. Reichenbacher M, Popp J, *Strukturanalytik organischer und anorganischer Verbindungen*, (B G Teubner Verlag / GWV Fachverlage GmbH, Wiesbaden, Wiesbaden), 2007.

[Received: 30.09.2015; accepted : 12.02.2016]



Isotopic effects in (surface enhanced) Raman spectroscopy – Single molecule aspects

Stephan Kupfer¹, Volker Deckert^{1,2} and Stefanie Gräfe¹

¹*Institute of Physical Chemistry and Abbe Center of Photonics, Friedrich-Schiller-University Jena, Helmholtzweg 4, 07743 Jena, Germany*

²*Institute of Photonic Technology Jena (IPHT), Albert-Einstein-Straße 9, 07745 Jena, Germany*

Dedicated to Professor Wolfgang Kiefer on the occasion of his 75th birthday

Generally, isotopic effects are of minor importance in standard vibrational spectroscopy, this is in particular the case, if the signal originates from a macroscopic sample. Consequently, an average spectrum with respect to the natural isotopic redundancy is obtained. However, for *State-of-the-Art* high-resolution techniques, e.g. surface-enhanced Raman spectroscopy, where only a small number of molecules (or even merely a single molecule) are the focus of the exciting beam, isotopic effects can have a considerable influence on the spectral pattern. Here we present a computational study investigating such isotopic effects on the Raman spectrum for the ¹³C isotope in the thiophenol molecule. Therefore, the Raman spectra of all four possible singly ¹³C doped species are calculated at the density functional theory level of theory and compared to the undoped thiophenol reference spectrum. The impact of ¹³C substitution on the vibrational frequencies as well as on the Raman intensities is rationalized. In particular large effects are determined for the in-plane vibrational modes, while each of the five calculated species (one undoped and 4 singly doped) features a unique Raman intensity pattern. © Anita Publications. All rights reserved.

Keywords: Isotopic effects, Laser pulses, Thiophenol, Surface-enhanced Raman spectroscopy (SERS)

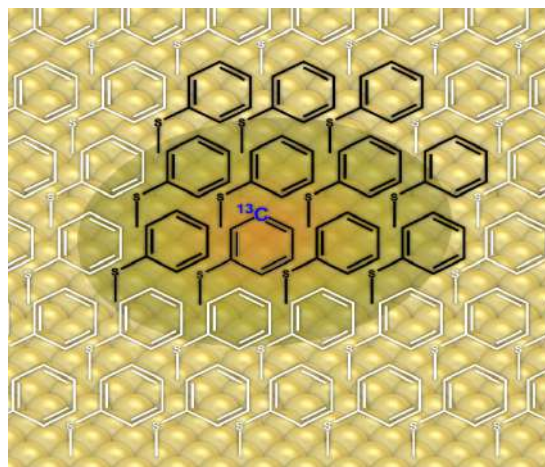
1 Introduction

In optical spectroscopy isotope effects are well known and often used in a directed way to obtain specific information about chemical bonds, structural conformations and chemical reactivity in general. Apart from those specific applications the isotopic ratios can be considered as constant, at least when working with natural abundant material. This is particularly true for organic substances as the natural abundance of the main constituents namely hydrogen and carbon. While it is clear, that mass isotopes result in a shift of spectroscopic bands, in optical spectroscopy this effect can be disregarded because the ratio of the isotopes is constant. As the specific site of the isotopic label in a natural compound or a compound synthesized with a natural isotope abundance must vary statistically, disregarding those effects can be only justified as long as the number of investigated molecules is large compared to the labeling sites. This condition is generally easily fulfilled in a spectroscopic experiment. Even in a microscope focus one finds roughly 10^{10} molecules and proper averaging can be safely assumed. Recent developments in technology, however, allow for a much higher spatial resolution even down to single molecule sensitivity. Prominent examples are single molecule surface enhanced Raman spectroscopy [1-4] (SERS) where specific hot spots are considered to play an important role or tip-enhanced Raman spectroscopy [5-7] where also hot spots are involved, however, in a very directed way. In such cases a statistical averaging cannot be expected anymore. Consequently, the spectra will show intrinsic features due to a specific isotopic labeling. In contrast to the above mentioned

Corresponding author :

e-mail: volker.deckert@uni-jena.de; phone: 49-3641-948347 (Volker Deckert);
s.graefe@uni-jena.de; phone: 49-3641-948330 (Stefanie Gräfe)

“controlled” experiments the labeling is statistically distributed over all atoms of the molecule and uniform spectra cannot be expected. While this effect is a direct consequence of the natural abundance of isotopes it is an unfamiliar concept in spectroscopy to have different band positions and intensities for the “same” chemical structure even without considering specific molecular orientations. We will discuss specifically the effect of ^{13}C labeling on a thiophenol. As a relatively simple molecule the number of distinct positions are limited, further it was already extensively studied by SERS and more importantly this molecule forms self-assembled monolayers,[8-12] see Fig 1, that provide a basis for dedicated experiments to also experimentally investigate such effects in addition to the theoretical investigation presented here.



F

Fig 1. SERS setup with thiophenol anchored on Gold surface, molecules excited by laser beam in black with the ^{13}C doped Carbon atom in blue.

From a computational point of view several studies investigated isotopic effects in chemical reactions, i.e. thermodynamic and kinetic properties with respect to transition states [1,13-15] as well as the kinetic isotopic effect in competitive $\text{S}_{\text{N}}2$ (bimolecular nucleophilic substitution) and E_2 (bimolecular elimination) reaction pathways [16-19]. Further combined experimental-theoretical studies focused on isotopic effects in vibrational spectroscopy, while density functional theory (DFT) proved to yield good agreements with respect to experimentally observed frequency shifts [20-24]. However, much less is known concerning the influence of isotopic effects on intensities in vibrational spectroscopy, in particular with respect to Raman spectroscopy [25].

Here we present a combined experimental-theoretical investigation on the influence of ^{13}C on the Raman spectrum of thiophenol. Therefore, DFT calculations are applied to determine effects on the vibrational frequencies as well as on the Raman intensities.

2 Computational Details

All quantum chemical calculations were performed using the program package Gaussian 09 [26]. The fully optimized equilibrium structure of thiophenol was obtained at the DFT level of theory by means of the B3LYP [27,28] XC functional and the 6-31G(d) double- ζ basis set [29] in gas phase. A subsequently performed vibrational analysis yielded the vibrational normal modes, frequencies and Raman activities. Gaussian 09 uses by default the mass of the most abundant isotopes that is ^1H with 1.00783 amu for Hydrogen, ^{12}C with 12.00000 amu for Carbon and ^{32}S with 31.97207 amu for Sulphur [30,31]. In order to investigate

the impact of isotopic effects on the Raman pattern, further vibrational calculations were performed by substituting a single ^{12}C atom with ^{13}C . This was done for the Carbon atoms C1-C4 as depicted in Fig 2.

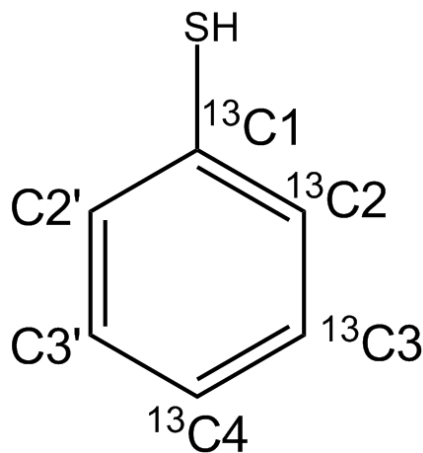


Fig 2. Molecular structure of thiophenol with labeled single ^{13}C substitution sites that is $^{13}\text{C1}$ at the thiol group, in *ortho* $^{13}\text{C2}$, *meta* $^{13}\text{C3}$ and in *para* position $^{13}\text{C4}$.

Based on the natural abundances of the Carbon isotopes of approximately 98.93% ^{12}C and 1.07% ^{13}C [32], the proportions of the singly doped thiophenol species are 0.18% C1, 0.36% C2, 0.36% C3 and 0.18% C4. The vibrational frequencies of the undoped thiophenol (^{12}C only) and of the four single doped forms (^{12}C only) were scaled by a factor of 0.97 in order to correct for the lack of anharmonicity and the approximate treatment of electron correlation; the vibrational modes were broadened by Lorentzian functions with a full-width at half maximum of 20 cm^{-1} to generate a typical Raman band structure.

3 Results and Discussion

The ground state structure of thiophenol optimized at the B3LYP/6-31G(d) level of theory is of C_s symmetry, thus, the SH fragment is oriented perpendicular to the aromatic plane of the phenyl fragment. Carbon-Carbon bond lengths of 1.3996 Å for C1-C2 and 1.3960 Å for C2-C3 and C3-C4 are obtained, while for the Carbon-Sulphur bond a value of 1.8068 Å is found (see Fig 2). For the Carbon-Hydrogen bond lengths values of 1.0857, 1.0868 and 1.0687 Å are obtained in *ortho*-, *meta*- and *para*-position, respectively, while the Sulphur-Hydrogen bond features an equilibrium length of 1.3530 Å. The phenyl moiety is almost perfectly planar as rationalized by means of the dihedral angle spanned by the Carbon atoms C2-C3-C3'-C2' of 0.01° . However, the Sulphur atom is slightly displaced with respect to the aromatic plane, which is evident from the C4-C1-S angle of 178.20° .

The focus of the vibrational analysis is set on the vibrational normal modes that feature the most pronounced impact on the Raman intensity pattern with respect to single ^{13}C substitution, thus, the further discussion is confined to the frequency range between 500 and 1700 cm^{-1} represented by the vibrational modes 7 to 27. The thiophenol Raman spectrum obtained for the natural isotope redundancy of Carbon that is 98.93% ^{12}C and 1.07% ^{13}C , depicted in Fig (3a). Therefore, such spectrum is correlated to a macroscopic average of Raman signals originating from the collective amount of undoped and doped thiophenol species (in different orientations). Thus, it is obtained by summation over the Raman signals of the five species (see Fig 3b) weighted by the respective probability.

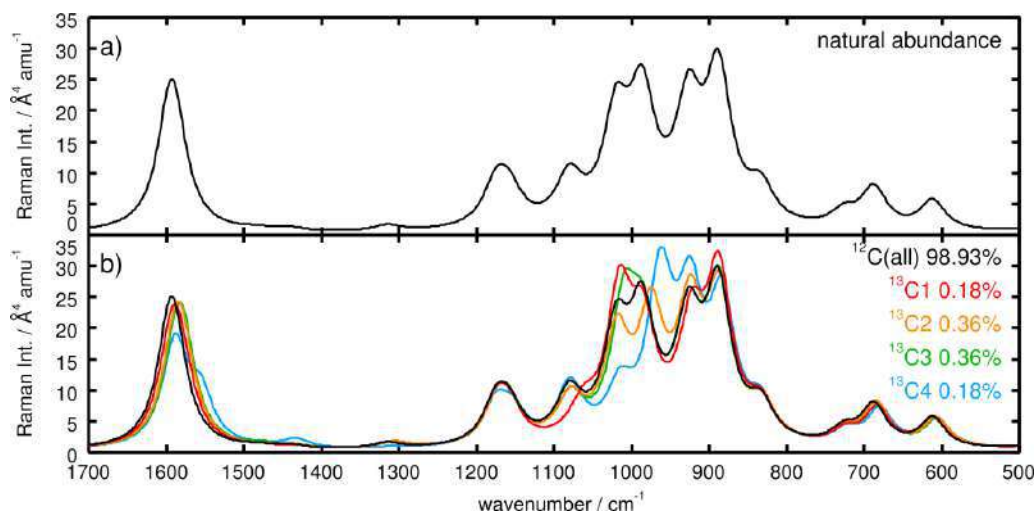


Fig 3. Simulated Raman spectrum obtained for, (a), the natural Carbon isotope abundance (98.93% ^{12}C and 1.07% ^{13}C) and, (b), the undoped thiophenol (in black) and the single doped ^{13}C spectra $^{13}\text{C1}$ (red), $^{13}\text{C2}$ (orange), $^{13}\text{C3}$ (green) and $^{13}\text{C4}$ (blue).

These species are the undoped form with exclusively ^{12}C , and the four singly doped forms $^{13}\text{C1}$ - $^{13}\text{C4}$, while $^{13}\text{C2}$ and $^{13}\text{C3}$ feature the double weight (0.36%) with respect to $^{13}\text{C1}$ and $^{13}\text{C4}$ (0.18%) due to the C_s symmetry of thiophenol.

The Raman spectrum of the undoped thiophenol ($^{12}\text{C}(\text{all})$ in Fig (3b)) features weak bands and shoulders at approximately 723, 834, 1314 and 1446 cm^{-1} , medium intense Raman features at 612, 688, 1078 and 1167 cm^{-1} and intense bands at 890, 924, 988, 1016 and 1592 cm^{-1} . The respective spectra obtained for the single doped form, see $^{13}\text{C1}$, $^{13}\text{C2}$, $^{13}\text{C3}$ and $^{13}\text{C4}$ in Fig (3b), feature partially considerable deviations from the undoped Raman spectrum. Predominate alterations are found in the spectral range between 800 and 1100 cm^{-1} as well as for the band structure at approximately 1600 cm^{-1} . The spectrum of $^{13}\text{C1}$ shows merely slight changes in the position of the intense bands (889, 919, 991, 1013 and 1589 cm^{-1}), however, the band at 1013 cm^{-1} holds an increased intensity. Similar alterations are observed for $^{13}\text{C2}$ with intense bands at 889, 923, 974, 1017 and 1584 cm^{-1} . Opposed to single ^{13}C doping in C1, the Raman band at 1017 cm^{-1} features a decreased intensity with respect to the reference spectrum of the undoped thiophenol. The intensity pattern of $^{13}\text{C3}$ (see Fig (3b)) resembles the pattern of $^{13}\text{C1}$. Here the intense bands are located at 890, 924, 990, 1005 and 1584 cm^{-1} , while the intensity of the band at 1005 cm^{-1} is once more increased with respect to the ^{12}C reference spectrum.

Summation over the five spectra in Fig (3b) namely the undoped ^{12}C spectrum, $^{12}\text{C}(\text{all})$, and the singly doped spectra $^{13}\text{C1}$, $^{13}\text{C2}$, $^{13}\text{C3}$ and $^{13}\text{C4}$ weighted by the factors of 0.9893, 0.0018, 0.0036, 0.0036 and 0.0018, respectively, yields the natural abundance spectrum displayed in Fig (3a). This averaged Raman spectrum is almost identical to the $^{12}\text{C}(\text{all})$ spectrum of Fig (3b), with the five intense bands being found at 890, 924, 988, 1016 and 1592 cm^{-1} . This way it is evident that isotopic effects originating by ^{13}C have no influence on the Raman spectrum on a macroscopic scale.

However, for *State-of-the-Art* spectroscopic techniques that are able to go below the diffraction limit postulated by Ernst Abbe, isotopic effects (e.g. by means of ^{13}C) are of increased significance. This is clearly the case for techniques, where only few or even only a single molecule is in the focus of the laser beam, see Fig 1. In such cases the obtained (Raman) spectrum is no longer an average of a manifold of molecular

orientations and isotopic redundancy. For thiophenol with six Carbon atoms, each Carbon atom is with a probability of 1.07% the ^{13}C isotope; in consequence, the probability to have one ^{13}C atom in thiophenol is 6.42%. Therefore, roughly every 16th thiophene molecule exhibits a ^{13}C atom. In order to investigate the impact of single ^{13}C doping in more detail, the single vibrational modes 7-27 within the spectral range of 500 and 1700 cm^{-1} are studied in more details. The individual Raman spectra of the undoped and the single doped species are depicted in Fig 4(a-e). The vibrational modes of all species are assigned with respect to the modes of the undoped thiophenol ($^{12}\text{C}(\text{all})$), however, the order of the vibrational modes may change upon ^{13}C doping.

The vibrational (Raman active) modes underlying the Raman features of $^{12}\text{C}(\text{all})$ in Fig (3b) at 612, 688, 723, 834, 890, 924, 988, 1016, 1078, 1167, 1314, 1446 and 1592 cm^{-1} are assigned in Fig (4a). The medium bright bands at 612 and 688 cm^{-1} as well as the shoulder at 723 cm^{-1} are correlated to the vibrational modes **7**, **9** and **10** at 611.7, 688.4 and 726.7 cm^{-1} , furthermore the low intensity mode **8** is found at 682.9 cm^{-1} . The band structure between 800 and 1200 cm^{-1} holds contributions from the modes **11-21**, while the shoulders at 834 and 1078 cm^{-1} originate from the modes **11** (1071.4 cm^{-1}) and **19** (1081.0 cm^{-1}), in addition the dark mode **18** is found at 1071.4 cm^{-1} . The vibrational modes **12**, **13**, **16** and **17** at 888.0, 926.5, 986.5 and 1019.9 cm^{-1} contribute to the bands at 890, 924, 988 and 1016, while two further dark modes (**14** and **15**) are localized at 944.7 and 971.8 cm^{-1} , respectively. The modes **20** and **21** (1157.6 and 1174.8 cm^{-1}) contribute to the band at 1167 cm^{-1} .

The frequency range between 1200 and 1500 cm^{-1} shows almost no signal, merely two weak modes at 1314.5 (**23**) and 1441.9 cm^{-1} (**24**) and two dark modes at 1289.1 (**22**) and 1482.1 cm^{-1} (**25**). The Raman band at 1592 cm^{-1} originates from a superposition of two bright modes (**26** and **27**) at 1587.8 and 1594.9 cm^{-1} . Detailed information regarding the displacement vectors or rather the character of the modes **7-27**, frequencies and Raman activities are collected for all five, one undoped and four doped, species in Table 1. Besides, the vibrational frequencies and Raman activities, Table 1 comprises the frequency shifts ($\Delta_{\text{ref}} \tilde{\nu}$ in cm^{-1}) and relative Raman activity deviations of the singly ^{13}C doped species with respect to the undoped ^{12}C reference data. Closer inspection of the spectra shown in Fig (4a-e) and the data in Table 1 reveals that the vibrational frequencies and intensities are partially significantly depending on the ^{13}C substitution pattern.

Evidently only bathochromic shifts of the vibrational frequencies of the doped species are expected with respect to the undoped reference. This follows directly from the increased reduced mass μ_l and the definition of vibrational energy levels ω_{n_l} within the harmonic approximation:

$$\omega_{n_l} = \hbar \sqrt{\frac{k_l}{\mu_l}} (n + 1/2) \quad (1)$$

and the respective transition energy for a fundamental transition from the vibrational ground state (of the electronic ground state) to the first vibrationally excited state:

$$\omega_{0 \rightarrow 1_l} = \hbar \sqrt{\frac{k_l}{\mu_l}} \quad (2)$$

where k_l is the force constant and μ_l the reduced mass for the l th vibrational mode. In accordance, all frequency shifts ($\Delta_{\text{ref}} \tilde{\nu}$) in Table 1 are negative. The most pronounced frequency shifts (see maximum deviations in Table 1) are found for the vibrational modes **16** for $^{13}\text{C}2$, **22** for $^{13}\text{C}1$ and **26** for $^{13}\text{C}3$ and $^{13}\text{C}4$. This phenomenon will be explained exemplarily for the ring breathing mode (**16**), where only very small shifts of -1.2 and 1.1 cm^{-1} are observed for $^{13}\text{C}1$ and $^{13}\text{C}3$ and large shifts of -11.7 and -23.8 cm^{-1} for $^{13}\text{C}2$ and $^{13}\text{C}4$. Taking a closer look into the displacement vector of mode **16** one clearly sees that the Carbon atoms C1 and C3 feature very small displacements, while the atoms C2 and C4 show large displacements.

Thus, an increased reduced mass (^{13}C vs. ^{12}C) has only marginal impact in the positions C1 and C3 on the vibrational frequency and significant influence in C2 and C4. Accordingly, the magnitude of the isotopic effect on all other vibrational modes can be estimated for each ^{13}C position. In general, mainly in-plane vibrational modes, i.e., the modes **16-19** and **22-27** feature substantial shifts. However, the (in-plane) modes **20** and **21** exhibit for all ^{13}C positions only marginal shifts from 0.0 up to merely 4.8 cm^{-1} , this reasoned by means of the small displacements of the Carbon atoms in these modes.

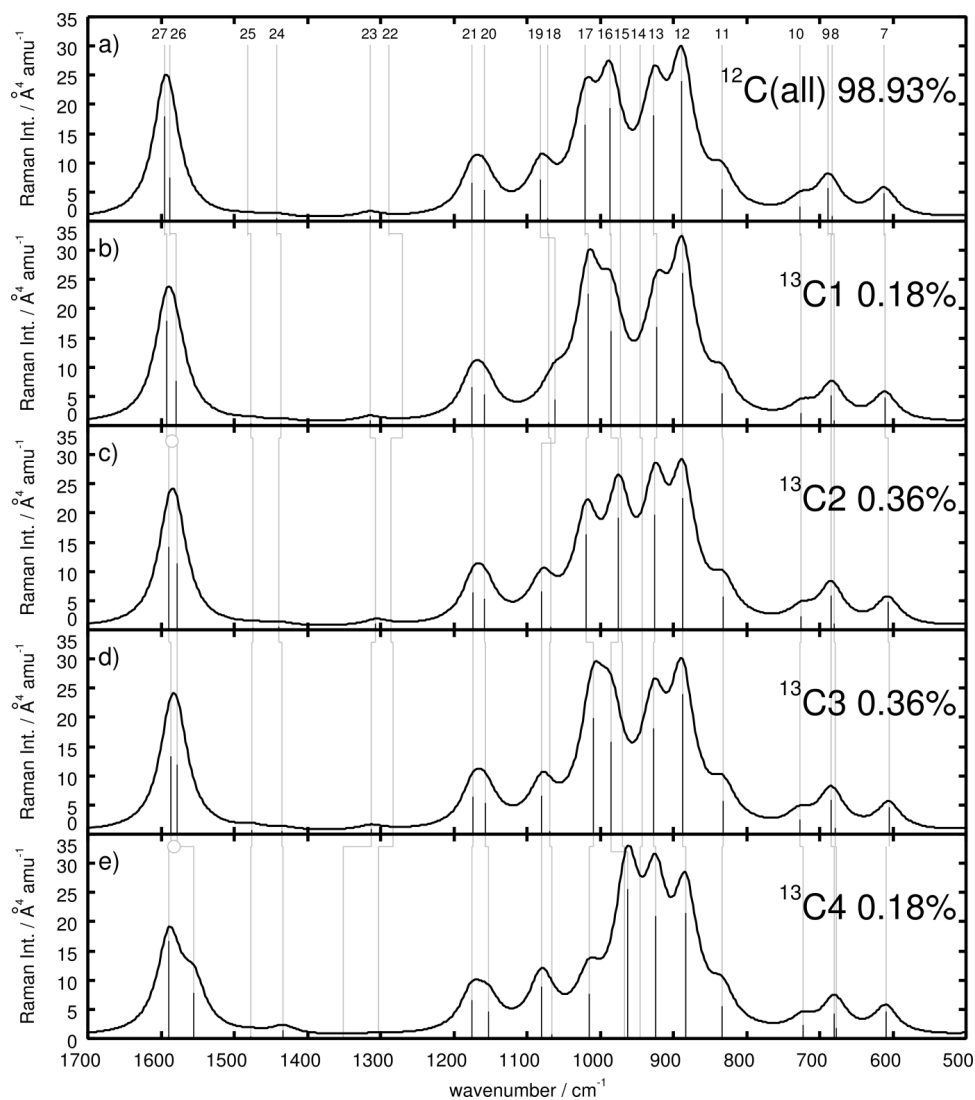
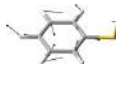
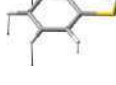
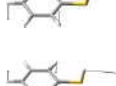
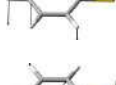
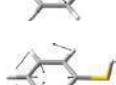


Fig 4. Assignment of the vibrational normal modes for the species, (a), $^{12}\text{C}(\text{all})$, (b), $^{13}\text{C}1$, (c), $^{13}\text{C}2$, (d), $^{13}\text{C}3$ and, (e), $^{13}\text{C}4$. The numbers of the vibrational modes of $^{12}\text{C}(\text{all})$ were used to label the modes of each respective species.

Comparison of the general impact of ^{13}C substitution in C1-C4 is rationalized based on the mean deviations (see [Table 1](#)). The smallest mean deviations are found in the positions C2 and C3 of -3.6 cm^{-1} , a slightly higher value of -4.0 cm^{-1} is observed in C1, while the highest value was found in C4 with -6.0

cm^{-1} . Notably, the induced vibrational shifts lead to alterations in the order of modes, this is in particular the case for the anti-symmetric and the symmetric scissoring modes **18** and **19**, which are inverted for ^{13}C . Also the modes **26** and **27** feature a pronounced mixing for ^{13}C substitution in *ortho*- and *para*- positions.

Table 1. Normal modes (undoped thiophenol) frequencies ($\tilde{\nu}$ in cm^{-1}) and Raman activities (I in $\text{\AA}^4 \text{amu}^{-1}$) for the undoped and the four singly ^{13}C doped species as well as frequency shifts ($\Delta_{\text{ref}} \tilde{\nu}$ in cm^{-1}) and relative Raman activity deviations with respect to the undoped thiophene. Mean deviations and maximum deviations are given for frequency shifts and relative Raman activity deviations

Mode		$\tilde{\nu}/\text{cm}^{-1}$ ($\Delta_{\text{ref}} \tilde{\nu}/\text{cm}^{-1}$)					$I / \text{\AA}^4 \text{amu}^{-1}$ ($(I/I_{\text{ref}}-1)$)				
		$^{12}\text{C}(\text{all})$	$^{13}\text{C1}$	$^{13}\text{C2}$	$^{13}\text{C3}$	$^{13}\text{C4}$	$^{12}\text{C}(\text{all})$	$^{13}\text{C1}$	$^{13}\text{C2}$	$^{13}\text{C3}$	$^{13}\text{C4}$
7		611.7 (0.0)	610.7 (-1.0)	606.9 (-4.8)	605.6 (-6.1)	609.8 (-1.9)	4.74 (0.00)	4.75 (0.00)	4.73 (0.00)	4.61 (-0.03)	4.70 (-0.01)
8		682.9 (0.0)	679.6 (-3.3)	680.3 (-2.6)	678.9 (-4.1)	676.9 (-6.0)	0.96 (0.00)	0.93 (-0.03)	1.09 (0.13)	1.01 (0.04)	1.70 (0.76)
9		688.4 (0.0)	683.8 (-4.6)	685.0 (-3.4)	684.7 (-3.6)	680.6 (-7.8)	5.66 (0.00)	5.22 (-0.08)	5.79 (0.02)	5.83 (0.03)	4.31 (-0.24)
10		726.7 (0.0)	724.9 (-1.8)	725.5 (-1.2)	726.6 (-0.1)	723.4 (-3.3)	2.50 (0.00)	2.21 (-0.11)	2.37 (-0.05)	2.50 (0.00)	2.32 (-0.07)
11		833.2 (0.0)	833.2 (0.0)	831.5 (-1.7)	831.5 (-1.7)	833.2 (0.0)	5.55 (0.00)	5.55 (0.00)	5.64 (0.02)	5.66 (0.02)	5.55 (0.00)
12		888.0 (0.0)	887.3 (-0.7)	886.8 (-1.2)	887.9 (-0.1)	883.1 (-4.9)	23.96 (0.00)	26.10 (0.09)	22.52 (-0.06)	24.05 (0.00)	21.55 (-0.10)
13		926.5 (0.0)	922.5 (-4.0)	924.9 (-1.6)	926.4 (-0.1)	924.5 (-2.0)	18.14 (0.00)	16.82 (-0.07)	19.66 (0.08)	18.07 (0.00)	20.99 (0.16)
14		944.7 (0.0)	944.7 (0.0)	942.5 (-2.3)	942.1 (-2.7)	944.7 (0.0)	0.02 (0.00)	0.02 (0.00)	0.11 (5.56)	0.02 (0.05)	0.02 (0.00)
15		971.8 (0.0)	971.8 (0.0)	971.3 (-0.4)	969.9 (-1.9)	967.1 (-4.7)	0.10 (0.00)	0.09 (-0.12)	0.12 (0.17)	0.11 (0.04)	0.06 (-0.40)
16		986.5 (0.0)	985.2 (-1.2)	974.8 (-11.7)	985.3 (-1.1)	962.7 (-23.8)	19.45 (0.00)	16.09 (-0.17)	19.12 (-0.02)	15.83 (-0.19)	25.57 (0.31)
17		1019.9 (0.0)	1015.6 (-4.2)	1018.8 (-1.0)	1009.9 (-10.0)	1015.1 (-4.8)	16.59 (0.00)	22.50 (0.36)	16.37 (-0.01)	19.96 (0.20)	7.70 (-0.54)
18		1071.4 (0.0)	1070.0 (-1.3)	1067.2 (-4.2)	1069.1 (-2.3)	1065.6 (-5.8)	0.59 (0.00)	0.60 (0.03)	0.55 (-0.07)	0.59 (0.01)	0.65 (0.12)

19		1081.0	1061.9	1079.7	1079.7	1080.2	7.16	4.48	6.49	6.53	8.90
		(0.0)	(-19.0)	(-1.3)	(-1.3)	(-0.8)	(0.00)	(-0.37)	(-0.09)	(-0.09)	(0.24)
20		1157.6	1157.6	1157.6	1156.5	1152.9	5.26	5.26	5.27	5.26	4.66
		(0.0)	(0.0)	(0.0)	(-1.2)	(-4.8)	(0.00)	(0.00)	(0.00)	(0.00)	(-0.11)
21		1174.8	1174.8	1173.1	1173.4	1174.8	6.51	6.52	6.35	6.33	6.53
		(0.0)	(0.0)	(-1.7)	(-1.4)	(0.0)	(0.00)	(0.00)	(-0.02)	(-0.03)	(0.00)
22		1289.1	1269.6	1285.7	1283.6	1282.7	0.01	0.01	0.09	0.05	0.02
		(0.0)	(-19.5)	(-3.4)	(-5.5)	(-6.4)	(0.00)	(0.44)	(9.44)	(4.43)	(1.31)
23		1314.5	1314.5	1306.5	1312.8	1302.7	0.91	0.91	1.04	0.85	0.26
		(0.0)	(0.0)	(-8.0)	(-1.7)	(-11.8)	(0.00)	(0.00)	(0.14)	(-0.06)	(-0.71)
24		1441.9	1435.5	1438.6	1434.2	1433.1	0.52	0.36	0.54	0.46	1.47
		(0.0)	(-6.4)	(-3.3)	(-7.7)	(-8.9)	(0.00)	(-0.31)	(0.05)	(-0.12)	(1.82)
25		1482.1	1477.3	1474.8	1476.5	1477.1	0.37	0.36	0.28	0.63	0.32
		(0.0)	(-4.8)	(-7.2)	(-5.6)	(-4.9)	(0.00)	(-0.02)	(-0.23)	(0.73)	(-0.11)
26		1587.8	1578.8	1578.5	1577.7	1555.7	7.51	7.59	11.31	11.91	7.77
		(0.0)	(-8.9)	(-9.3)	(-10.1)	(-32.0)	(0.00)	(0.01)	(0.51)	(0.59)	(0.03)
27		1594.9	1592.2	1588.7	1587.0	1588.8	18.00	17.97	14.13	13.30	16.69
		(0.0)	(-2.7)	(-6.3)	(-8.0)	(-6.1)	(0.00)	(0.00)	(-0.22)	(-0.26)	(-0.07)
Mean Deviation		0.0	-4.0	-3.6	-3.6	-6.7	0.00	-0.02	0.73	0.26	0.11
Maximum Deviation		0.0	-19.5	-11.7	-10.1	-32.0	0.00	0.44	9.44	4.43	1.82

Besides the influence of isotopic effects on the vibrational frequencies also considerable alterations with respect to the intensity pattern were calculated. In general the Raman intensity for a fundamental transition (Stokes) is given by:

$$I_{g0 \rightarrow g1_l} = \frac{4e^4}{16\pi^2 \epsilon_0^2 c^4} (\omega_L - \omega_l)^4 |(\alpha_{\alpha,\beta})_{g0 \rightarrow g1_l}|^2 \quad (3)$$

where ω_L is the frequency of the incident light and ω_l the frequency of the l^{th} normal mode. The transition polarizability $(\alpha_{\alpha,\beta})_{g0 \rightarrow g1_l}$ (with its compounds α and β) is universally defined for a transition between any initial state $|i\rangle$ and the final state $|f\rangle$ via the intermediate state $|n\rangle$ as:

$$(\alpha_{\alpha,\beta})_{i \rightarrow f} = \frac{1}{\hbar} \sum_n \left(\frac{\langle f | \hat{\mu}_\alpha | n \rangle \langle n | \hat{\mu}_\beta | i \rangle}{\omega_{n,i} - \omega_L - i\Gamma} + \frac{\langle f | \hat{\mu}_\beta | n \rangle \langle n | \hat{\mu}_\alpha | i \rangle}{\omega_{n,f} + \omega_L + i\Gamma} \right) \quad (4)$$

with the compounds of the dipole operators $\hat{\mu}_\alpha$ and $\hat{\mu}_\beta$ and the damping factor Γ describing homogeneous broadening. The damping factor can be neglected in off-resonant cases since it is small relative to $\omega_{(n,i)}$. As can be seen from Eq (3), the intensity is proportional to $(\omega_L - \omega_l)^4$, thus, an isotopically caused bathochromic shift of the frequency ω_l leads to an increase of its intensity. This is also evident by means of the mean

deviations of the intensity, where only for $^{13}\text{C}1$ a slight decrease (-2%) was observed. For $^{13}\text{C}2$, $^{13}\text{C}3$, and $^{13}\text{C}4$, the intensity increases by 73% , 26% and 11% , respectively. Maximum intensity deviations of 44% ($^{13}\text{C}1$ mode **22**), 944% ($^{13}\text{C}2$ mode **22**), 443% ($^{13}\text{C}3$ mode **22**) and 182% ($^{13}\text{C}4$ mode **24**) are computed, while (allowedly) the highest impact on the intensity was observed for very weakly Raman active modes such as the modes **8**, **14**, **22**, **23**, **24** and **25**. For the very bright modes **12**, **13**, **16** and **17**, moderate variation ranging from -54% to $+36\%$ are found. However, for certain modes the intensity also decreases (e.g. mode **17** with -54%). This is in particular the case for normal modes that show alterations upon substitution with ^{13}C . Examples for such modes are the previously mentioned modes **26** and **27** showing a pronounced mixing in $^{13}\text{C}2$ and $^{13}\text{C}3$, [Table 2](#) displays these modes for all five species. Thus, a direct comparison of the modes and their respective intensities is no longer possible.

Table 2. Vibrational normal modes for $^{12}\text{C}(\text{all})$, $^{13}\text{C}(1)$, $^{13}\text{C}(2)$, $^{13}\text{C}(3)$ and $^{13}\text{C}(4)$

Mode	$^{12}\text{C}(\text{all})$	$^{13}\text{C}(1)$	$^{13}\text{C}(2)$	$^{13}\text{C}(3)$	$^{13}\text{C}(4)$
26					
27					

Taking into account mean deviations and maximum deviations for all four ^{13}C species with respect to frequency and intensity it is notable that substitution in *ortho*- and *meta*-position induces the smallest frequency shifts (mean deviation: 3.6 cm^{-1} , maximum deviation: -11.7 and -10.1 cm^{-1}) but the most prominent intensity changes (mean deviation: $+73\%$ and $+26\%$, maximum deviation: 944% and 443%). This result is in particular interesting since these positions show the double probability for ^{13}C substitution than C1 and C4 based on the C_s symmetry of thiophenol. Therefore, an experimentally observed isotopic effect in highly spatial resolved Raman techniques is more likely to be verifiable by means of the alterations in the intensity pattern than by the frequencies, while certainly alterations in the intensity pattern are highly correlated to variations in the band positions due to line broadening.

4 Conclusions

In high-resolution vibrational spectroscopic techniques only a small number of molecules is in the focus of the Laser, e.g. in SERS. Thus, isotopic effects might be of enhanced importance for such techniques compared to low-resolution techniques, where a macroscopic average Raman signal is measured. In order to evaluate the magnitude of isotopic effects originating from ^{13}C (natural isotope redundancy: 98.93% ^{12}C and 1.07% ^{13}C) on both the vibrational frequencies as well as on the Raman intensities, quantum chemical calculations have been performed for the thiophenol molecule. DFT calculations using the B3LYP XC functional and the 6-31G(d) basis set yielded the fully optimized equilibrium structure of thiophenol (C_s symmetry). Subsequently, a vibrational analysis using the most abundant isotopes that is ^1H , ^{12}C and ^{32}S has been performed. Frequency calculations for the singly ^{13}C doped species in the positions C1, C2, C3 and C4 yielded the respective Raman spectra. Summation over weighted Raman spectra for the ^{12}C and the four singly ^{13}C doped species, yielded the natural redundancy Raman signal, which was found to be

almost identical to the ^{12}C reference spectrum. Hence, unsurprisingly, isotopic effects originating from ^{13}C are of marginal importance on a macroscopic scale. However, a considerable effect can be estimated with respect to high-resolution techniques. Since ^{13}C doping leads to an increased reduced mass, exclusively bathochromic shifts of the vibrational frequencies are estimated, which is confirmed by the calculations. The largest mean deviation of -6.7 cm^{-1} has been determined for the $^{13}\text{C}_4$ species, while substitution in C1, C2 and C3 leads to similar shifts of -4.0 and -3.6 cm^{-1} . The individual frequency shift of each vibrational mode was found to be strictly correlated to the displacement of the ^{13}C atom. Besides variations in the frequencies upon ^{13}C substitution, also effects with respect to the Raman intensity have been investigated. Since the Stokes intensity is proportional to $(\omega_L - \omega_I)^4$, a general increase of the intensity is estimated based on the observed bathochromic shifts. This was confirmed by the mean intensity deviations with respect to the ^{12}C reference system, where besides for $^{13}\text{C}_1$ only positive amplifications of 73% ($^{13}\text{C}_2$), 26% ($^{13}\text{C}_3$) and 11% ($^{13}\text{C}_4$) are computed. However, also intensity decrease was found for several normal modes, this is partially accounted for by mixing of normal modes upon ^{13}C substitution, which hinders a direct comparison of the specific normal modes.

The estimated influence of isotopic effects on the Raman spectrum of thiophenol can be expected to be of significant importance for single molecule detection, but also for small ensembles where due to the small numbers averaging effects cannot be expected. In both cases the isotopes will induce variations with respect to intensity and frequency.

References

1. Kneipp K, Wang Y, Kneipp H, Perelman L T, Itzkan I, Dasari R, Feld M S, *Phys Rev Lett*, 78(1997)1667-1670.
2. Ru E C Le, Meyer M, Etchegoin P G, *J Phys Chem B*, 110(2006)1944-1948.
3. Moyer P J, Schmidt J, Eng L M, Meixner A J, *J Am Chem Soc*, 122(2000)5409-5410.
4. Nie S M, Emery S R, *Science*, 275(1997)1102-1106.
5. Anderson M S, *Appl Phys Lett*, 76 (2000)3130-3132.
6. Hayazawa N, Inouye Y, Sekkat Z, Kawata S, *Opt Commun*, 183(2000)333-336.
7. Stockle R M, Suh Y D, Deckert V, Zenobi R, *Chem Phys Lett*, 318(2000)131-136.
8. Tripathi A, Emmons E D, Christesen S D, Fountain III A W, Guicheteau J A, *J Phys Chem C*, 117(2013)22834-22842.
9. Jung H Y, Park Y.-K, Park S, Kim S K, *Anal Chim Acta*, 602(2007)236-243.
10. Taylor C E, Pemberton J E, Goodman G G, Schoenfish M H, *Appl Spectrosc*, 53(1999)1212-1221.
11. Huang Y.-F, Wu D.-Y, Zhu H.-P, Zhao L.-B, Liu G.-K, Ren B, Tian Z.-Q, *Phys Chem Chem Phys*, 14(2012)8485-8497.
12. Biggs K B, Camden J P, Anker J N, Van Duyne R P, *J Phys Chem A*, 113(2009)4581-4586.
13. Smirnov V V, Lanci M P, Roth J P, *J Phys Chem A*, 113(2009)1934-1945.
14. Wiest O, Black K A, Houk K N, *J Am Chem Soc*, 116(1994)10336-10337.
15. Nicholson K M, Sholl D S, *Phys Rev B*, 86(2012)134113; doi.org/10.1103/PhysRevB.86.134113
16. Hu W P, Truhlar D G, *J Am Chem Soc*, 118(1996)860-869.
17. Pabis A, Paluch P, Szala J, Paneth P, *J Chem Theory Comput*, 5(2009)33-36.
18. Tsai W.-C, Hu W.-P, *Molecules*, 18(2013)4816-4843.
19. Villano S M, Kato S, Bierbaum V M, *J Am Chem Soc*, 128(2006)736-737.
20. Ashley D C, Brinkley D W, Roth J P, *Inorg Chem*, 49(2010)3661-3675.
21. Basova T V, Kiselev V G, Schuster B.-E, Peisert H, Chassé T, *J Raman Spectrosc*, 40(2009)2080-2087.
22. Leybold C F, Reiher M, Brehm G, Schmitt M O, Schneider S, Matousek P, Towrie M, *Phys Chem Chem Phys*, 5 (2003)1149-1157.
23. Singh D, Ojha A K, Kiefer W, Singh R K, *Vib Spectrosc*, 49(2009)242-250.

24. Palfi V K, Guillon T, Paulsen H, Molnar G, Bousseksou A, *CR Chim*, 8(2005)1317-1325.
25. Alparone A, *J Chem*, 2013(2013).
26. Frisch M J , Trucks G W, Schlegel H B, Scuseria G E, Robb M A, Cheeseman J R, Scalmani G, Barone V, Mennucci B, Petersson G A, Nakatsuji H, Caricato M, Li X, Hratchian H P, Izmaylov A F, Bloino J, Zheng G, Sonnenberg J L, Hada M, Ehara M, Toyota K, Fukuda R, Hasegawa J, Ishida M, Nakajima T, Honda Y, Kitao O, Nakai H, Vreven T, Montgomery J A (Jr), Peralta J E, Ogliaro F, Bearpark M, Heyd J J, Brothers E, Kudin K N, Staroverov V N, Kobayashi R, Normand J, Raghavachari K, Rendell A, Burant J C, Iyengar S S, Tomasi J, Cossi M, Rega N, Millam J M, Klene M, Knox J E, Cross J B, Bakken V, Adamo C, Jaramillo J, Gomperts R, Stratmann R E, Yazyev O, Austin A J, Cammi R, Pomelli C, Ochterski J W, Martin R L, Morokuma K, Zakrzewski V G, Voth G A, Salvador P, Dannenberg J J, Dapprich S, Daniels A D, Farkas O, Foresman J B, Ortiz J V, Cioslowski J, Fox D J, Gaussian 09 Revision A.02.
27. Becke A D, *J Chem Phys*, 98(1993)5648-5652.
28. Lee C, Yang W, Parr R G, *Phys Rev B*, 37(1988)785-789.
29. Hariharan P C, Pople J A, *Theor Chim Acta*, 28(1973)213-222.
30. Audi G, Wapstra A H, *Nucl Phys A*, 565(1993)1-65.
31. Audi G, Wapstra A H, *Nucl Phys A*, 595(1995)409-480.
32. Vocke R D, *Pure Appl Chem*, 71(1999)1593-1607.

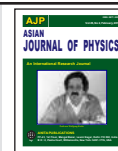
[Received : 30.09.2015; accepted: 01.11.2015]

Volker Deckert is Professor at the Institute of Physical Chemistry at the Friedrich-Schiller University Jena and also heads the Nanoscopy department at the Leibniz Institute of Photonic Technologies, Jena. He received his Ph.D. from the University of Würzburg, working on Raman spectroscopy. As a post-doc his research focus shifted towards non-linear and time-resolved laser spectroscopy at the University of Tokyo and KAST, in Kawasaki. Since his habilitation at the ETH Zurich, he does research on near-field optical spectroscopy, a subject he still pursues and currently applies to biological samples and to the investigation of chemical reactivity on the nanometer scale.



Stefanie Gräfe joined the Friedrich Schiller University Jena in 2013 and is the head of the Theoretical Chemistry group at the Institute for Physical Chemistry. She has received her Ph D from the University of Würzburg working on femtosecond time-resolved quantum dynamics. As a postdoc at the Steacie Institute for Molecular Sciences of the National Research Council in Ottawa, Canada, and afterwards, at the Institute for Theoretical Physics at the Vienna University of Technology she has been working on simulating electronic dynamics in strong-field and attosecond atomic and molecular processes. Since moving to Jena, she also turned her attention to electronic processes in weaker fields, allowing with the help of quantum chemical methods to calculate ground and excited state spectroscopic properties of molecules.





Binary heavy metal bismuthate glass-ceramics with classical glass forming oxide

S Simon, M Muresan-Pop, C Leordean, M Baia and L Baia

*Babes-Bolyai University, Faculty of Physics & Institute of Interdisciplinary Research in Bio-Nano-Sciences,
400084 Cluj-Napoca, Romania*

Dedicated to Professor Wolfgang Kiefer on the occasion of his 75th birthday

As-prepared and heat treated heavy metal binary system of bismuth oxide with classical glass forming oxides were investigated with respect to their ability to form vitreous structure in the composition range of sillenite. For this high ratio of bismuth to classical glass former cation $\text{Bi}/\text{M} = 12$ ($\text{M} = \text{Si}, \text{Ge}$ or B), the X-ray diffraction analysis of as-prepared samples points out $8\text{-Bi}_2\text{O}_3$ nanocrystalline phase separation, while FTIR and Raman spectroscopic analysis provide typical features for the vitreous state, with no feature of crystalline phase. After heat treatment $\text{Bi}_{12}\text{MO}_{20-8}$ sillenite crystalline phases are identified in all samples, and the structural changes induced by sillenites development are clearly revealed in FTIR and Raman spectra. A new attempt for structural units assignment based on analysis of vibrational spectra recorded from heavy metal bismuthate glass-ceramic systems with classical glass forming oxides is presented. © Anita Publications. All rights reserved.

Keywords: Bismuth oxide, FTIR and Raman spectra, Glass-ceramics, Sillenites.

1 Introduction

Heavy-metal oxide glasses commonly defined as glasses containing over 50 percent cations of bismuth and/or lead, which participate in the glass structure as network formers [1], are intensely investigated both as glasses and glass—ceramics because they address a wide array of modern technological challenges in fields such as electronics, optoelectronics, solar energy, protective and decorative coatings, structural mechanics, medical, nuclear technology, superconductors and microfluidics [2].

Even though Bi_2O_3 is not a classical glass former, in the presence of conventional glass formers like SiO_2 , GeO_2 , P_2O_5 and B_2O_3 , or just of usual glass modifiers, it may form a glass network [1]. The glass systems investigated for special applications are usually formed from several components, but the binary systems of bismuthate heavy metal glasses deserve attention with respect to the structural changes induced by the second oxide added to the major content of Bi_2O_3 . The results published on binary systems with the common glass formers (B_2O_3 , SiO_2 , P_2O_5 , GeO_2) showed that the highest Bi_2O_3 content for which the systems are still vitrified is lower in the case of GeO_2 , and especially of P_2O_5 , and therefore the $\text{Bi}_2\text{O}_3\text{-P}_2\text{O}_5$ system has attracted less attention [2].

Based on density, glass transition temperature and short wavelength optical cutoff measurements, significant structural changes were reported for binary bismuth silicate and bismuth borate systems depending on their compositions [3, 4]. Our earlier spectroscopic studies on bismuthate glasses with B_2O_3 , SiO_2 and GeO_2 doped with transition metal or rare earth oxides [5-14] including heavy metal glass compositions contributed to highlighting the structural changes occurring in these systems.

Bi_2O_3 is a polymorphic compound presenting five major structural modifications, one stable: monoclinic α -, three metastable: tetragonal β -, body-centered cubic γ - and orthorhombic ϵ -, and one high-

Corresponding author :

e-mail: simons@phys.ubbcluj.ro, Phone: +40-264-405375, Fax: +40-264-591906 (S Simon)

temperature: face-centered cubic δ - Bi_2O_3 [15]. γ - Bi_2O_3 phase doped with other oxides delivers new crystalline structures of $\text{Bi}_{12}\text{SiO}_{20}$ sillenite type, but if the charge of dopant is less than $4+$, the structure could differ from that of the ideal composition for tetravalent cations.

The aim of this study was to investigate by X-ray diffraction, infrared and Raman spectroscopies the structural characteristics of binary heavy metal bismuthate glass-ceramics with the glass formers SiO_2 , GeO_2 and B_2O_3 , having the same 12:1 ratio between bismuth and silicon, germanium or boron atoms.

2 Experimental

Bismuthate glass-ceramics of compositions $6\text{Bi}_2\text{O}_3 \cdot \text{SiO}_2$, $6\text{Bi}_2\text{O}_3 \cdot \text{GeO}_2$ and $12\text{Bi}_2\text{O}_3 \cdot \text{B}_2\text{O}_3$ were obtained by melting of Bi_2O_3 , SiO_2 , GeO_2 and H_3BO_3 of reagent purity grade and further denoted as Bi-Si, Bi-Ge and Bi-B, respectively. The mixed components were melted in sintered corundum crucibles, in a Carbolite furnace, at 1250°C for 15 minutes. The melts were quickly poured and cooled at room temperature by pressing between two stainless steel plates. In order to develop high content of crystalline phases in the glass matrices, the as-prepared samples were heat treated at 600°C for 24 hours.

X-ray diffraction analysis was carried out on a Shimadzu XRD-6000 diffractometer using Ni-filtered $\text{CuK}\alpha$ radiation ($\lambda = 1.5418\text{\AA}$) at a scanning speed of $2^\circ/\text{min}$. FTIR spectra were recorded with a spectral resolution of 2 cm^{-1} , in absorption mode, with a FT/IR-6200 Jasco Spectrometer by using the KBr pellet technique. Raman measurements were performed with a Witec Alpha 300R confocal Raman microscope equipped with a Raman spectroscopy system UHTS 300, using the 532 nm line of a Nd-YAG laser.

3 Results and Discussion

The transparent and apparently homogeneous $6\text{Bi}_2\text{O}_3 \cdot \text{SiO}_2$, $6\text{Bi}_2\text{O}_3 \cdot \text{GeO}_2$ and $12\text{Bi}_2\text{O}_3 \cdot \text{B}_2\text{O}_3$ melt-derived samples were expected to be vitreous, but their X-ray diffractograms evidence the presence of crystalline peaks (Fig 1). Nevertheless, the rescaled patterns (Fig 2) evidence the presence of amorphous component, but according to X-ray diffraction this occurs in a quite low amount.

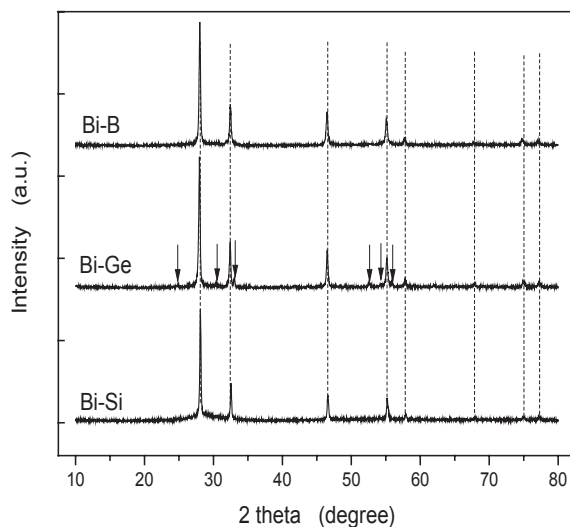


Fig 1. X-ray diffraction patterns of as-prepared samples

The crystalline phase developed in all as-prepared samples is δ - Bi_2O_3 (JCPDS 27-0052). Additional lines, indicated by arrows (Fig 1) for Bi-Ge sample, confirm that the vitrification of Bi_2O_3 with GeO_2 is

lower than with SiO_2 and B_2O_3 . The separation of Bi_2O_3 crystalline phase leads to a second non-crystalline phase rich in the classical glass forming oxide.

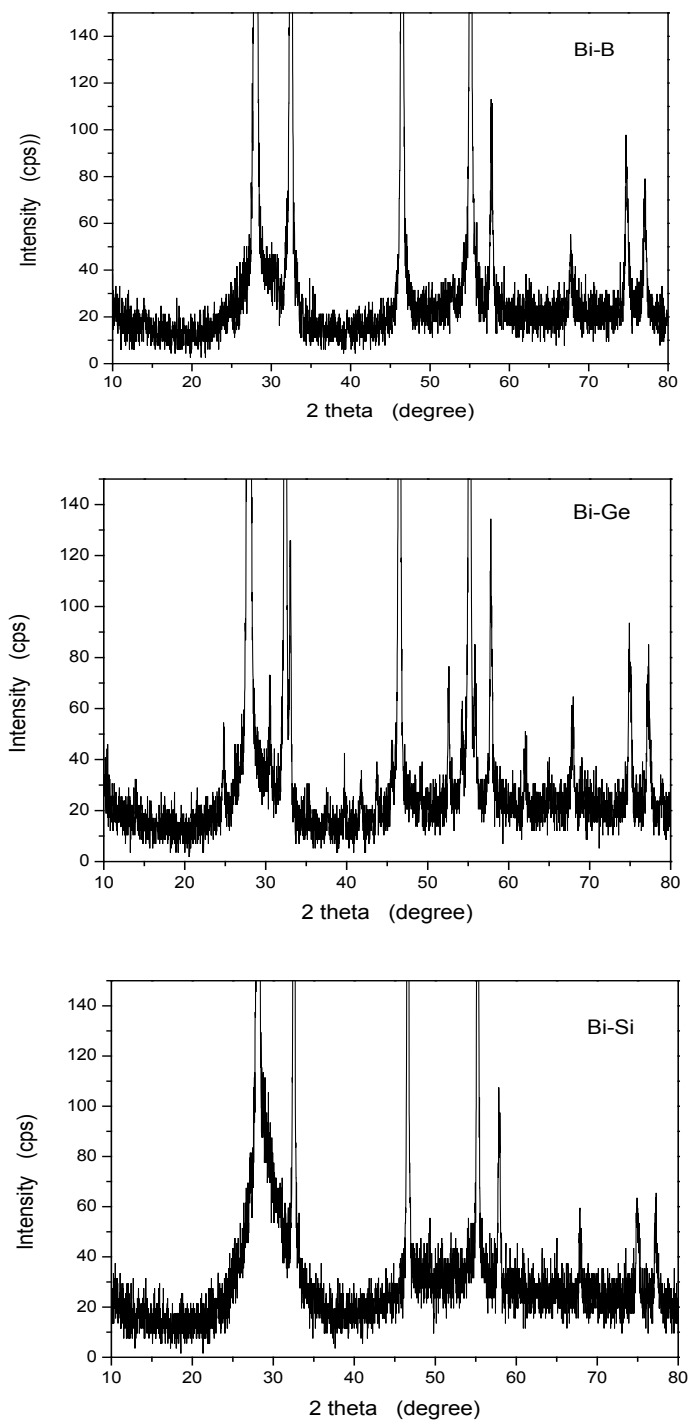


Fig 2. Resealed X-ray diffraction patterns of as-prepared samples

According to infrared and Raman results, the crystalline component observed by X-ray analysis is not reflected in the vibrational spectra, which are typical for structurally disordered systems (Figs 3 and 4). This could suggest that the local order around Bi^{3+} ions in $\delta\text{-Bi}_2\text{O}_3$ crystalline phase is quite similar with that from non-crystalline phase. The ill-defined coordination polyhedra of Bi^{3+} cations is a common feature of the crystalline compounds with very high content of bismuth [2].

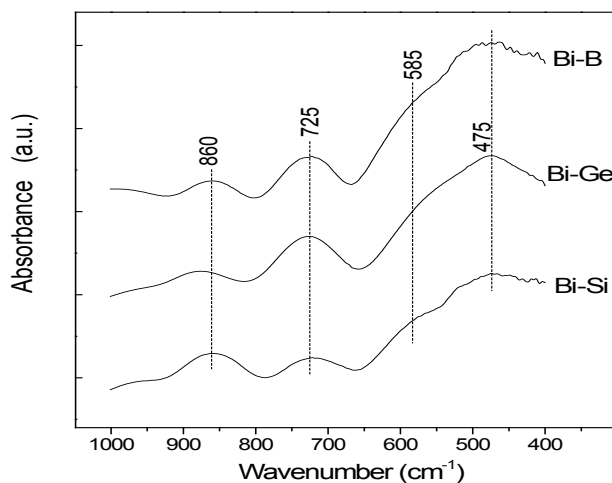


Fig 3. FTIR spectra of as-prepared samples

Broad infrared bands occur around 475, 585, 725 and 860 cm^{-1} (Fig 3). They are usually the bands observed in non-crystalline bismuth containing materials [6, 7, 16]. The relative intensity of the bands depends on the second oxide added to Bi_2O_3 . All these absorption bands are assigned due to vibrations of Bi-O related to $[\text{BiO}_6]$ octahedral-like structural units [16]; in fact they would be better nominated as $[\text{BiO}_5\text{E}]$ structural polyhedra, where the coordinative role of one oxygen is taken by the lone pair of electrons (E) of Bi^{3+} [2]. Bismuth ions are generally considered to form $[\text{BiO}_3]$ pyramidal or $[\text{BiO}_6]$ octahedral units in glasses [17]. The presence of $[\text{BiO}_3]$ structural units, if they would exist, should be signalled by an absorption band at 830 cm^{-1} [18], but this is not evidenced, so that only highly coordinated ($N \geq 6$) bismuth polyhedra build up the bismuthate structure of these samples.

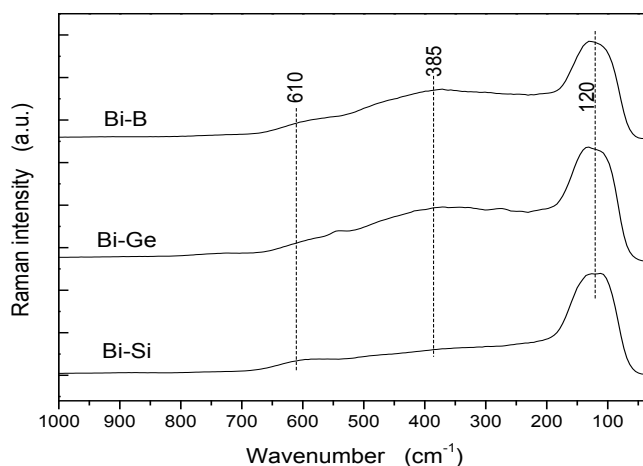


Fig 4. Raman spectra of as-prepared samples

The broad Raman peaks (Fig 4) denotes again the structural disorder in the as-prepared samples and they are typical for all non-crystalline bismuth containing materials [8, 19]. The peaks centred around 120, 385 and 610 cm^{-1} indicate the presence of the Bi^{3+} cations in $[\text{BiO}_6]$ octahedral units, while the shoulder around 385 cm^{-1} can be attributed to the Bi-O-Bi vibration of the octahedral $[\text{BiO}_6]$ or $[\text{BiO}_5\text{E}]$ [19].

Pyramidal units have four fundamental vibrations, which are all Raman active, while octahedral units have six modes of vibrations, three of them being Raman active [20]. The Raman vibrations observed in the as-prepared samples do not correspond to that expected for pyramidal units.

The crystalline phase developed after heat treatment in all samples (Fig 5) is $\text{Bi}_{12}\text{MO}_{20-8}$ ($\text{M} = \text{Si}, \text{Ge}$ or B) sillenite, namely $\text{Bi}_{12}\text{SiO}_{20}$ (JCPDS 37-0485), $\text{Bi}_{12}\text{GeO}_{20}$ (JCPDS 34-0096), and $\text{Bi}_{12}\text{BO}_{19.5}/\text{Bi}_{24}\text{B}_2\text{O}_{39}$ [21].

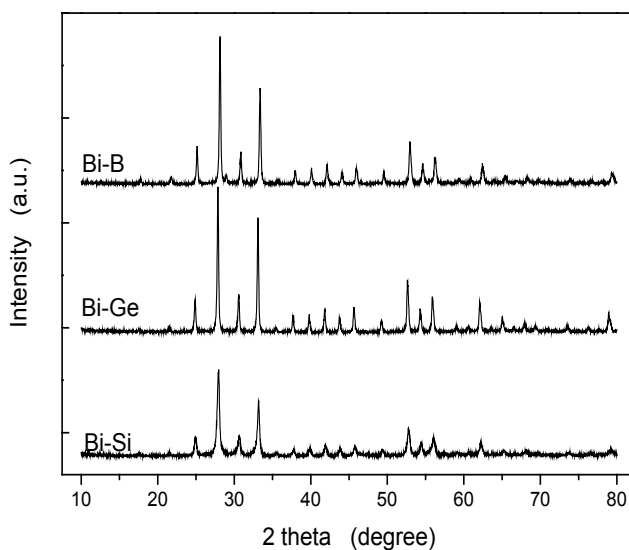


Fig 5. Xray diffraction patterns of heat treated samples

In fact, the composition of these phases fits the samples composition wherein Bi : M ratio is 12:1. The effect of structural rearrangement in an appreciable fraction of crystalline phase is clearly evidenced by the changes observed in infrared and Raman spectra of glass-ceramic samples after heat treatment (Figs 6 and 7).

The width of infrared and Raman bands denotes that the structural disorder is still present in sillenite phases developed after the applied heat treatment. Instead of the broad IR absorption bands observed around 475 and 585 cm^{-1} for as prepared samples, in sillenite samples these are each splitted into two bands, at 465 and 530 cm^{-1} , and at 575 and 605 cm^{-1} , respectively. A new band appearing around 680 cm^{-1} is evidenced in germanium containing sample. The broad absorption band around 725 cm^{-1} is further observed for Bi-Si sillenite, but does not appear in Bi-Ge sillenite spectrum, and is replaced by two narrow bands in case of Bi-B sillenite sample. The new band at 830 cm^{-1} , usually assigned to $[\text{BiO}_3]$ units [18], should be reassigned to $[\text{BiO}_5\text{E}]$ units, the only ones identified in sillenite crystals [2]. The band observed around 860 cm^{-1} from as-prepared samples is shifted to 870 cm^{-1} after heat treatment, and the intensity of Bi-Si has diminished, and is drastically attenuated in Bi-Ge and Bi-B samples.

The structural changes occurred after heat treatment are equally revealed by Raman spectroscopy.

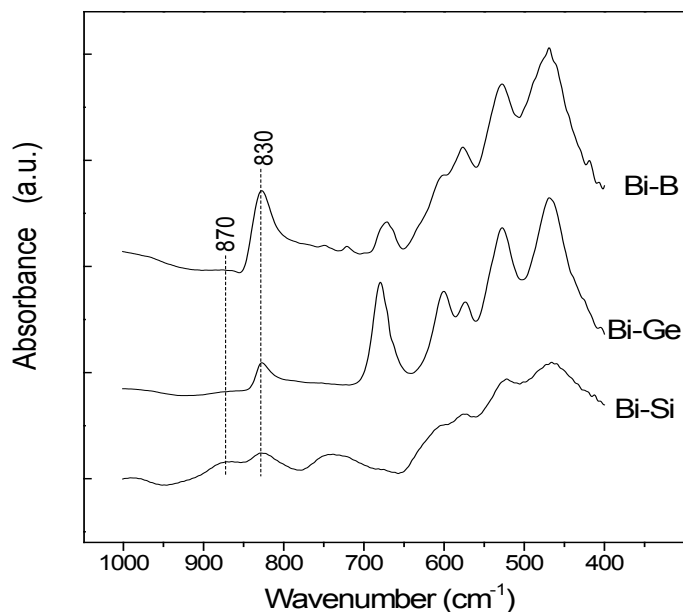


Fig 6. FTIR spectra of heat treated samples

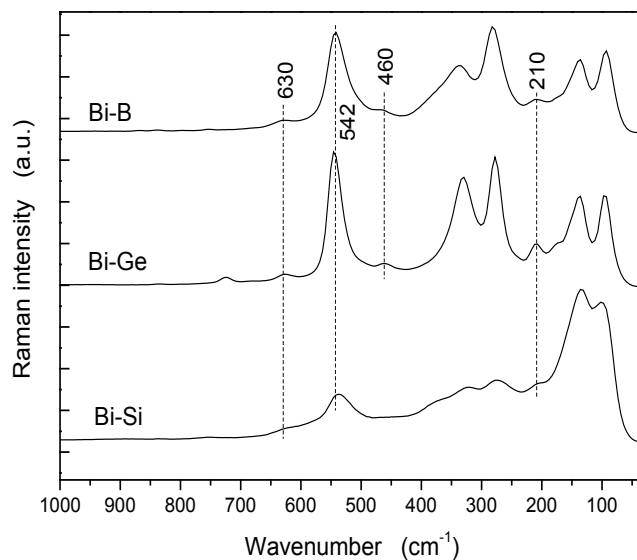


Fig 7. Raman spectra of heat treated samples

Both the broad Raman band at 120 cm^{-1} and the shoulder at 385 cm^{-1} observed from as-prepared samples are replaced each by two bands, at 90 and 130 cm^{-1} , and at 280 and 330 cm^{-1} , respectively. Additional Raman bands are recorded at 210 , 460 and 542 cm^{-1} . The band at 542 cm^{-1} was already perceptible in Bi-Ge sample before heat treatment, and denotes an incipient sillenite phase in the as-prepared sample in accordance with X-ray diffraction pattern (Fig 1). Instead of the very large shoulder at 610 cm^{-1} (Fig 4) a weak band occurs at 630 cm^{-1} (Fig 7). Like in FTIR spectra, where the occurrence of the new band at 830 cm^{-1} after heat treatment proves the presence of $[\text{BiO}_5\text{E}]$ structural units, in Raman spectra the new band around 542 cm^{-1} is likely related to these units.

Recent theoretical results [22] obtained by DFT calculations show that the main lines from infrared and Raman spectra of sillenites are assigned to modes associated with the movement of three oxygen species: O_1 – oxygens bonded to two nearest neighbor bismuth atoms, O_2 – oxygens bonded to three bismuths, and O_3 – oxygens that are forming $[MO_4]$ tetrahedra around Si^{4+} , Ge^{4+} or B^{3+} cations. In this approach, focused on oxygens movement, the main lines in the vibrational spectra of sillenites are related with Bi- O_1 or Bi- O_2 bonds.

4 Conclusions

Melt-derived heavy metal binary systems of bismuth oxide and B_2O_3 , SiO_2 and GeO_2 classical glass formers with Bi:M ratio 12:1 ($M = B, Si$ or Ge) appear transparent and homogeneous, but they contain δ - Bi_2O_3 nanocrystalline phase rich in cations of classical glass formers. As-prepared samples present infrared and Raman spectroscopic features characteristic to vitreous systems, even though the X-ray diffraction patterns are specific to δ - Bi_2O_3 crystalline phase. Only after heat treatment the bands denote features characteristic to sillenite crystalline phases with $[BiO_5E]$ structural units. The results obtained by infrared and Raman spectroscopies support the major preponderance of structural units with high local disorder even in the sillenites.

It appears more appropriate to analyse the structure of heavy metal bismuthate non-crystalline materials in terms of structural units identified in their crystalline counterparts than simply to consider only $[BiO_3]$ and $[BiO_6]$ units. Taking this into account, it is more proper to discuss about low coordinated ($N < 6$) bismuth species (in BiO_3E and BiO_5E units) and highly coordinated ($N \geq 6$) species (in BiO_6E , BiO_7E and BiO_8E units). In all cases, we have to keep in mind that all these units are characterised by a large disorder and that always three oxygens are much closer to bismuth, facts that can explain the ability of bismuth to act as glass network former even when only highly coordinated bismuth species are present in the matrices.

Note: Part of these results were presented by Simon S at Int. Seminar on Glasses and other Functional Materials – ISGFM, Dec. 11-13, 2014, Acharya Nagarjuna University, Guntur, A.P, India.

References

1. Dumbaugh W H, Lapp J C, *J Am Ceram Soc*, 75(1992)2315-2326.
2. Maeder T, *Int Mater Rev*, 58(2013)3-40.
3. Stehle C, Vira C, Hogan D, Feller S, Affatigato M, *Phys Chem Glasses*, 39(1998)83-86.
4. George HB, Vira C, Stehle C, Meyer J, Evers S, Hogan D, Feller S, Affatigato M, *Phys Chem Glasses*, 40(1999) 326-332.
5. Baia L, Maniu D, Iliescu T, Simon S, Schlucker S, Kiefer W, *Asian J Phys*, 9(2000)51-57.
6. Baia L, Stefan R, Kiefer W, Popp J, Simon S, *J Non-Cryst Solids*, 303(2002)379-386.
7. Baia L, Stefan R, Popp J, Simon S, Kiefer W, *J Non-Cryst Solids*, 324(2003)109-117.
8. Baia L, Kiefer W, Simon S, *Recent Res Devel Non-Cryst Solids*, 4(2004)1-25.
9. Baia L, Kiefer W, Simon S, *Rom Rep Phys*, 56(2004)430-435.
10. Baia L, Kiefer W, Simon S, *Phys Chem Glasses*, 46(2005)279-283.
11. Radu A, Baia L, Kiefer W, Simon S, *Vibr Spectrosc*, 39(2005)137-140.
12. Simon S, Todea M, *J Non-Cryst Solids*, 352(2006)2947-2951.
13. Simon S, Udvar A D, *J Am Ceram Soc*, 93(2010)2760-2763.
14. Ponta O, Baia L, Baia M, Simon S, *Z Phys Chem*, 225(2011)647-660
15. Dapcevic A, Poleti D, Karanovic L, Rogan J, Drazic G, *Solid State Sci*, 25(2013)93-102.
16. Iordanova R, Dimitrov V, Dimitriev Y, Klissurski D, *J Non-Cryst Solids*, 180(1994)58-65.

17. Iordanova R, Dimitriev Y, Dimitrov V, Kassabov S, Klissurski D, *J Non-Cryst Solids*, 204(1996)141-150.
18. Dimitrov V, Dimitriev Y, Montenero A, *J Non-Cryst Solids*, 180(1994)51-57.
19. Kharlamov A A, Almeda R M, Heo H, *J Non-Cryst Solids*, 202(1996)233-240.
20. Hazra S, Mandal S, Ghosh A, *Phys Rev B*, 56(1997)8021-8025.
21. He F, Wang J, Deng D, Cheng J, *J Chin Ceram Soc*, 37(2009)1791-1795.
22. Arenas D J, Middleton C, Kemper A F, *Phys Rev B*, 91(2015), Article No 144103; doi: 10.1103/PhysRevB.91.144103

[Received:30.9.2015; accepted:13.10.2015]

Professor Simion Simon received at Babes-Bolyai University in Cluj-Napoca, Romania, his Diploma degree in Physics in 1972 with specialization in Solid State Physics, and the title of Doctor in Physics in 1986 for magnetic resonance studies on vitreous and partially crystallized oxide materials. His research results were appreciated by the Romanian Academy by awarding him in 1982 the Hurmuzescu Prize. From 1993 to 1994, he was a Visiting Professor at the Department of Molecular Spectroscopy of the Catholic University of Nijmegen, The Netherlands. Further his research interest extended on correlation between structure and properties of new materials with potential bio-medical and environmental applications.



In the last two decades a fruitful collaboration with the group lead by the distinguished Professor Wolfgang Kiefer at the University of Würzburg, Germany, is acknowledged. Professor Simon has authored and co-authored more than 260 papers published in prestigious scientific journals.

Currently, Professor Simon is the Head of the Interdisciplinary Research Institute on Bio-Nano-Sciences of Babes-Bolyai University in Cluj-Napoca, Romania.

Marieta Pop-Muresan is a researcher at the Interdisciplinary Research Institute on Bio-Nano-Sciences of Babes-Bolyai University, Cluj-Napoca, Romania. In 2012, she received the Ph D degree in Physics, at Babes-Bolyai University of Cluj-Napoca, under the supervision of Professor Simion Simon.



Her scientific interests are in the fields of structural and functional materials, crystal engineering and polymorphism. She has published 13 papers in peer-reviewed journals.

Cosmin Leordean Lucian received his Ph D degree in 2014 at Babes-Bolyai University, Cluj-Napoca, Romania, under the scientific advisory of Professor Simion Astilean, with a thesis on fabrication and demonstration of unconventional plasmonic substrates towards SERS biosensing applications. He is co-author of 11 papers published in peer-reviewed journals.



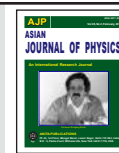
Monica Baia studied physics at the Babes-Bolyai University of Cluj-Napoca, Cluj-Napoca, Romania, and obtained her Ph.D. degree in nature sciences in 2003 under the supervision of Prof. dr. dr. h.c. Wolfgang Kiefer from the University of Wuirzburg, Germany. In 2003, she also began her academic career as a Lecturer at the BabesBolyai University of Cluj-Napoca. Starting with October 2005 she worked for a nine-month period with Prof. Juergen Popp's group as a Postdoctoral Research Fellow at the University of Jena, Germany. In 2007 she received the Prize In Hoc Signo Vinces of the National University Research Council of Romania. Since 2008 she has worked as an Associate Professor at the Faculty of Physics of the Babes-Bolyai University.



Her research interests are focused on the elucidation of the structure and adsorption behavior of pharmaceutical and biological relevant compounds by using Raman spectroscopy and SERS, the study of the optical and structural properties of metallic ordered and disordered nanostructures for their further use as SERS substrates in biomolecular and pollutants detection as well as the development and application of nanostructured materials for wastewater treatment via photocatalysis. She is the author or coauthor of more than 85 publications in peer-reviewed journals, three books and two book chapters. She is also serving as editorial board member for several scientific journals.

Lucian Baia earned his Ph.D. degree in 2003 at the University of Wuirzburg, Germany under the supervision of Prof. dr. dr. h.c. Jurgen Popp. In 2003, he also began his academic career as a Lecturer at the Faculty of Physics of the Babes-Bolyai University of Cluj-Napoca. Since 2008, he is working as Associate Professor at the Department of Condensed Matter Physics and Advanced Technologies at the Faculty of Physics. His current research focuses on the obtaining and characterization of porous nanoarchitectures with controllable morphology and structure for environmental and biomedical applications. He is author or coauthor of more than 100 peer-reviewed publications, three books, and three book chapters, three patent applications and is also serving as editorial board member for several scientific journals.





Femtosecond time-resolved four-wave mixing spectroscopy of coupled electron-nuclear motion

Julian Albert and Volker Engel

Institute for Physical and Theoretical Chemistry, University Würzburg,

Emil-Fischer-Str. 42, 97074, Würzburg, Germany.

(Dedicated to Professor Wolfgang Kiefer on the occasion of his 75th birthday)

We present a theoretical study of time-resolved four-wave mixing (FWM) spectroscopy on a model system describing coupled electron-nuclear dynamics. Changing the parameterization of the Coulomb-interaction, two situations can be created. In one case, the Born-Oppenheimer adiabatic approximation holds. In adjusting the pulse sequence it is then possible to separately monitor ground state and excited state vibrational wave-packet dynamics. In the second case, strong non-adiabatic coupling is present so that the separation of ground- and excited state nuclear dynamics becomes difficult. To investigate details of the dynamics and its relation to the spectroscopy, we compare FWM-signals obtained from an exact numerical calculation to those obtained within the adiabatic approximation. © Anita Publications. All rights reserved.

Keywords: Femtosecond, Laser pulses, Emission, Born-Oppenheimer approximation Time-resolved four-wave mixing (FWM) spectroscopy

1 Introduction

Modern non-linear spectroscopic techniques are valuable tools to investigate the structure of and dynamics in molecules [1,2]. One of such techniques is four-wave-mixing (FWM) spectroscopy. The latter employs the interaction of three laser pulses, which induce a third-order polarization in the molecular sample under study. This then leads to the emission of a signal field, which reveals properties of the system. With the availability of ultra-short pulses it became possible to characterize molecular dynamics in solution with FWM-techniques obtaining a resolution on the femtosecond time scale [3–5]. Later on, gas-phase systems were also studied [6,7]. A significant step forward was taken by Kiefer and co-workers who applied femtosecond time-resolved FWM to I_2 gas samples [8–11] (for later work see, e.g., Refs. [12,13]) and developed a pulse-scheme which allows for the detection of ground-state molecular dynamics which is usually difficult to access.

In the mentioned experiments on gas phase I_2 samples, the laser fields couple the ground and a first excited electronic state. The used pulse sequence consists of two pulses with wave vectors (k_1 , k_2) interacting simultaneously with the system. A third pulse (k_3) is delayed by a time τ . The signal consists of the time-integrated polarization (in homodyne detection) emitted in direction $k_1 - k_2 + k_3$, which is detected as a function of the pulse delay. As a general trend, it was shown that, for negative delay times, the motion in the excited electronic state is monitored. On the other hand, for positive τ , the ground state vibrational dynamics is mapped. These experimental results were confirmed by theory [14–16]. It has to be noted that such a clear separation is possible only when the Born-Oppenheimer (BO) approximation [17] is valid which means that the two electronic states are coupled exclusively by the laser fields. If non-adiabatic couplings are present, vibrational dynamics is not restricted to a single state and a different picture will appear. Non-

Corresponding author :

e-mail: volker.engel@uni-wuerzburg.de (Volker Engel)

adiabatic effects being present in excited states were also studied by Kiefer and co-workers with FWM techniques [18,19]. In this paper, we present a theoretical study of FWM-spectroscopy on coupled electron-nuclear dynamics. Therefore, we use a model restricted to two degrees-of-freedom, where an electron and a proton move in one dimension between two fixed ions. This model, introduced by Shin and Metiu [20], has proved to be very useful in illustrating basic features of electron-nuclear dynamics [21-28]. In Section 2, the model is described, and the calculation of the FWM-signal is outlined. Numerical results are presented in Section 3, which also contains a summary of the paper.

2 Theory and Model

2.1 Shin-Metiu model

To study coupled electron-nuclear dynamics we consider the configuration which is sketched in Fig 1, upper panel. Two protons are fixed at positions of $L = \pm 5 \text{ \AA}$. An electron and a proton move in a single dimension with coordinate r and coordinate R , respectively.

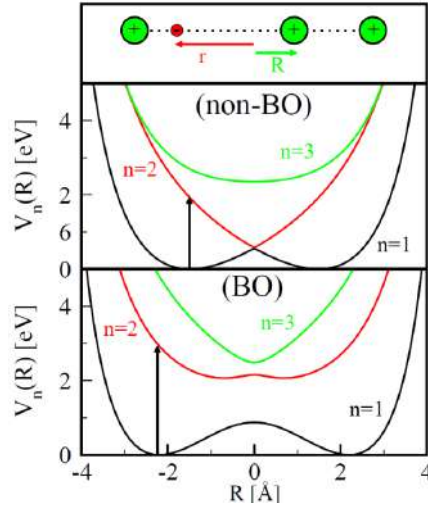


Fig 1. Upper panel: Configuration of the model system consisting of two fixed protons and an electron with coordinate r and a proton with coordinate R . Different parameterizations of the interaction potential lead to potential energy curves which reflect the situation of strong (non-BO, $R_c = 2.5 \text{ \AA}$) and weak (BO, $R_c = 1.5 \text{ \AA}$) non-adiabatic coupling. The arrows indicate the photon energies used in the calculations.

The interaction potential is parameterized as in [20] (atomic units are used here and in what follows):

$$V(\tau, R) = \frac{1}{|L/2 - R|} + \frac{1}{|L/2 + R|} - \frac{\text{erf}(|L/2 - r|/R_f)}{|L/2 - r|} - \frac{\text{erf}(|R - r|/R_c)}{|R - r|} - \frac{\text{erf}(|L/2 + r|/R_f)}{|L/2 + r|}. \quad (1)$$

Here (erf) denotes the error function and the screening parameter R_f is taken as 1.5 \AA . The second parameter (R_c) determines the interaction between the moving particles and by adjusting it, the cases of adiabatic and non-adiabatic motion can be realized, see below. The Hamiltonian is:

$$\hat{H} = \frac{\hat{P}^2}{2M} + \frac{\hat{p}^2}{2} + V(r, R), \quad (2)$$

where \hat{P} and \hat{p} are the nuclear and electronic momentum operator, respectively, and M is the proton mass.

The electronic Schrödinger equation is obtained for fixed values of the nuclear coordinate R :

$$\left[\frac{\hat{P}^2}{2} + V(r, R) \right] \varphi_n(r, R) = V_n(R) \varphi_n(r, R). \quad (3)$$

Numerical solution of this equation yields potential energy curves $V_n(R)$ and electronic wave functions $\varphi_n(r, R)$, where (n) is the quantum number of the electronic state $|n\rangle$. Depending on the value of the parameter R_c , different potentials are obtained. In Fig 1, lower and middle panel, we show potentials calculated for values of $R_c = 1.5 \text{ \AA}$ and $R_c = 2.5 \text{ \AA}$, respectively. Only the lowest three states with quantum numbers ($n = 1-3$) are included in the figure. It is seen that for $R_c = 1.5 \text{ \AA}$, the ground and first excited state potentials are well separated which suggests that the adiabatic approximation holds in the respective energy range. This is indeed the case [21,23], and we will show that this situation is comparable to that of the I_2 molecule (see section 1), leading to similar features in the FWM-signals. Within the adiabatic approximation, the nuclear dynamics in the two states can be treated separately by solving the nuclear time-dependent Schrödinger equation:

$$i \frac{\partial}{\partial t} \psi_n(R, t) = \hat{H}_n \psi_n(R, t) = \left(\frac{\hat{P}^2}{2M} + V_n(R) \right) \psi_n(R, t). \quad (4)$$

On the other hand, regarding the potentials in the middle panel of Fig 1, one notices that the lowest two potentials show an avoided crossing with a very small energy gap at $R = 0$, pointing a breakdown of the BO-approximation.

2.2 Four-wave mixing signals

The total electric field perturbing the electron-nuclei system consists of three laser pulses and is written as:

$$E(t) = \sum_{l=1}^3 [E_l^{(+)}(t - T_l) + E_l^{(-)}(t - T_l)], \quad (5)$$

where

$$E_l^{(\pm)}(t - T_l) = \frac{1}{2} A_l(t - T_l) e^{\mp i\omega_l(t - T_l)}. \quad (6)$$

Here, the (+) component (wave vector in $(+k_l)$ -direction) triggers an absorption process and the (-) component (wave vector in $(-k_l)$ -direction) induces stimulated emission. We employ Gaussian pulse envelopes $A_l(t - T_l)$ of different widths, having maxima at times T_l . The three photon energies are set to the same value ($\omega_l = \omega$) which, for the signal, corresponds to the case of degenerate four wave mixing (DFWM). As values we choose $\omega = 2.9 \text{ eV}$ for the parameterization with $R_c = 1.5 \text{ \AA}$ and $\omega = 1.9 \text{ eV}$ for $R_c = 2.5 \text{ \AA}$. These values are marked with arrows in Fig 1. The pulse sequence is such, that the first two pulses ($l = 1, 2$) act simultaneously at $T_1 = T_2 = 0$, and the third pulse ($l = 3$) is time delayed with the delay time $\tau = T_3$.

The time-dependent polarization of third order, leading to emission under the phase-matching condition ($k_s = k_1 - k_2 + k_3$) has several contributions. In order to illustrate the non-BO effects it is sufficient to restrict the calculation to a single term (being the most significant one in the iodine case [14]) which reads:

$$P^{(3, c)}(t, \tau) = \langle \psi^{(0)}(r, R, t) | \mu(r, R) | \psi^{(3)}(k_3 - k_2 + k_1, r, R, t, \tau) \rangle_{r, R}. \quad (7)$$

Here enters the dipole moment $\mu(r, R) = (-r + R)$ and different wave functions evolving from perturbation theory. The superscript (c) is added to indicate that here the polarization is determined from solutions of the time-dependent Schrödinger equation for the coupled motion. The zeroth-order functions is:

$$\psi^{(0)}(r, R, t) = e^{-iE_0 t} \psi_0(r, R), \quad (8)$$

where $\psi_0(r, R)$ is the ground-state wave function with energy E_0 . The third-order wavefunction, for positive delay-times τ , is calculated iteratively [29, 30] as:

$$\begin{aligned} \psi^{(1)}(k_1, r, R, t + \Delta t) &= \hat{U}(\Delta t) \psi^{(1)}(k_1, r, R, t) + \\ &\quad i(\mu(r, R)E_1^+(t + \Delta t) \psi^{(0)}(r, R, t + \Delta t)), \end{aligned} \quad (9)$$

$$\begin{aligned} \psi^{(2)}(-k_2 + k_1, r, R, t + \Delta t) &= \hat{U}(\Delta t) \psi^{(2)}(-k_2 + k_1, r, R, t) + \\ &\quad i(\mu(r, R)E_2^-(t + \Delta t) \psi^{(1)}(k_1, r, R, t + \Delta t)), \end{aligned} \quad (10)$$

$$\begin{aligned} \psi^{(3)}(k_3 - k_2 + k_1, r, R, t + \Delta t) &= \hat{U}(\Delta t) \psi^{(3)}(k_3 - k_2 + k_1, r, R, t) + \\ &\quad i(\mu(r, R)E_3^+(t + \Delta t) \psi^{(2)}(-k_2 + k_1, r, R, t + \Delta t)). \end{aligned} \quad (11)$$

Here enters the propagator for the coupled motion: $\hat{U}(\Delta t) = e^{-i\hat{H}\Delta t}$, and Δt is a finite time-step. For negative delay-time, the same scheme but for interchanged pulses, $l = 1$ and $l = 3$ applies. The propagation is performed numerically [31] on a two-dimensional grid.

Within the *BO* description, the polarization is

$$P^{(3, BO)}(t, \tau) = \langle \psi_1^{(0)}(R, t) | \mu_{1n}(R) | \psi_n^{(3)}(k_3 - k_2 + k_1, R, t, \tau) \rangle_R, \quad (12)$$

with the transition dipole moment:

$$\mu_{1n}(R) = \mu_{n1}(R) = \langle \varphi_1(r, R) | \mu(-r + R) | \varphi_n(r, R) \rangle_r. \quad (13)$$

The unperturbed function

$$\varphi_1^{(0)}(R, t) = e^{-iE_{1,0}t} \varphi_{1,0}(R), \quad (14)$$

is the ground state vibrational eigenfunction of Hamiltonian \hat{H}_1 with energy $E_{1,0}$. The iteration scheme now reads:

$$\begin{aligned} \psi_n^{(1)}(k_1, R, t + \Delta t) &= \hat{U}_n(\Delta t) \psi_n^{(1)}(k_1, R, t) \\ &\quad + i(\mu_{n1}(R)E_1^+(t + \Delta t) \psi_1^{(0)}(R, t + \Delta t)), \end{aligned} \quad (15)$$

$$\begin{aligned} \psi_1^{(2)}(-k_2 + k_1, R, t + \Delta t) &= \hat{U}_1(\Delta t) \psi_1^{(2)}(-k_2 + k_1, R, t) \\ &\quad + i(\mu_{1n}(R)E_2^-(t + \Delta t) \psi_n^{(1)}(k_1, R, t + \Delta t)), \end{aligned} \quad (16)$$

$$\begin{aligned} \psi_n^{(3)}(k_3 - k_2 + k_1, R, t + \Delta t) &= \hat{U}_n(\Delta t) \psi_n^{(3)}(k_3 - k_2 + k_1, R, t) \\ &\quad + i(\mu_{n1}(R)E_3^+(t + \Delta t) \psi_1^{(2)}(-k_2 + k_1, R, t + \Delta t)). \end{aligned} \quad (17)$$

where $\psi_n^{(j)}$ is the vibrational wave function in state $|n\rangle$ in j -order perturbation theory.

The FWM-signal is calculated as (homodyne detection [32]):

$$S^{(s)}(\tau) = \int_{-T_p}^{T_p} dt |P^{(3, s)}(t, \tau)|^2, \quad (18)$$

where T_p is the full width at half maximum of the laser pulses and $s = c, BO$. We checked numerically that the calculated signals do not change significantly if the time-integration is performed over longer times, for a detailed discussion see Ref [16].

3 Results

We first regard the case of $R_c = 1.5 \text{ \AA}$, where the BO-approximation is valid and treat laser induced resonant transitions between the electronic states $|1\rangle$ and $|2\rangle$, where the potentials are those displayed in the lower panel of Fig 1. We use a pulse width of 2.8 fs which approximately corresponds to the impulsive limit [32], where all three pulses are δ -pulses. It is instructive to evaluate the polarization (Eq (12)) in this limit. This yields, for positive delays τ :

$$P^{(3, BO)}(t, \tau) = \langle \psi_1^{(0)}(t) | \mu_{12} | \hat{U}_2(t - \tau) \mu_{12} \hat{U}_1(\tau) \mu_{12} \mu_{21} \psi_1^{(0)}(0) \rangle, \quad (19)$$

Inserting the completeness relation employing the vibrational eigenfunctions $|\varphi_{n, mn}\rangle$ with energies $E_{n, mn}$ in states |1) and |2), respectively, yields

$$P^{(3, BO)}(t, \tau) = -e^{iE_{1,0}t} \sum_{m_1, m_2} \langle \psi_1^{(0)}(0) | \mu_{12} | \varphi_{2, m_2} \rangle \langle \varphi_{2, m_2} | \mu_{21} | \varphi_{1, m_1} \rangle \langle \varphi_{1, m_1} | \mu_{12} \mu_{21} | \psi_1^{(0)}(0) \rangle e^{-iE_{2, m_2}t} e^{i(E_{2, m_2} - E_{1, m_1})\tau}. \quad (20)$$

This leads to the signal

$$S^{(BO)}(\tau) = \sum_{m_1, m_2} \sum_{m'_1, m'_2} c(m_1, m_2, m'_1, m'_2) e^{i(E_{2, m_2} - E_{2, m'_2})\tau} e^{i(E_{1, m_1} - E_{1, m'_1})\tau} \int_{-T_p}^{T_p} dt e^{i(E_{2, m_2} - E_{2, m'_2})t} \quad (21)$$

where we have collected the product of the various matrix elements into coefficients $c(m_1, m_2, m'_1, m'_2)$. For long enough times T_p , the time-integrals are proportional to δ -functions δ_{m_2, m'_2} so that the signal simplifies to:

$$S_+^{(BO)}(\tau) \approx \sum_{m_1, m'_1} \sum_{m_2} c(m_1, m_2, m'_1, m'_2) e^{i(E_{1, m_1} - E_{1, m'_1})\tau} \quad (22)$$

We thus see that, for positive delay-times, the signal oscillates with energy differences between energies in the electronic ground state.

For negative delay-times the polarization reads:

$$\begin{aligned} P^{(3, BO)}(t, \tau) &= \langle \psi_1^{(0)}(t) | \mu_{12} | \hat{U}_2(t - \tau) \mu_{12} \mu_{21} \hat{U}_2(\tau) \mu_{21} \psi_1^{(0)}(0) \rangle \\ &= -e^{iE_{1,0}t} \sum_{m_2, m'_2} \langle \psi_1^{(0)}(0) | \mu_{12} | \varphi_{2, m_2} \rangle \langle \varphi_{2, m_2} | \mu_{21} \mu_{12} | \varphi_{2, m'_2} \rangle \langle \varphi_{2, m'_2} | \mu_{21} | \psi_1^{(0)}(0) \rangle \\ &\quad e^{-iE_{2, m_2}t} e^{i(E_{2, m_2} - E_{2, m'_2})\tau}, \end{aligned} \quad (23)$$

and the signal, using the same arguments as given above, is

$$S_-^{(BO)}(\tau) \approx \sum_{m_2, m'_2} b(m_2, m'_2) e^{i(E_{2, m_2} - E_{2, m'_2})\tau}, \quad (24)$$

with coefficients $b(m_2, m'_2)$ containing products of dipole matrix elements. We now encounter oscillations of the signal occurring as a function of the delay time τ which are determined by the energy differences in the excited state.

In Fig 2, upper panel, we show the BO-signal for the weak coupling case ($R_c = 1.5 \text{ \AA}$). At times when the three pulses overlap, the signal exhibits some transient effects. Oscillations are seen which reveal a different period for positive and negative delay times. We calculate the vibrational energies in both states and, within the energy range accessible by the pulses, find average spacings of $\Delta E_1 = 0.074 \text{ eV}$ and $\Delta E_2 = 0.086 \text{ eV}$, respectively. These numbers correlate with vibrational periods of $T_{1, \text{vib}} = 55 \text{ fs}$ and $T_{2, \text{vib}} = 47 \text{ fs}$, which is in perfect agreement with the numerical results. Note that, in calculating the energy spacings, symmetry has to be taken into account. Starting from the gerade (g) ground vibrational state, only ungerade (u) excited state vibrational levels can be excited. A two-photon transition back to the ground states results in a vibrational wave packet consisting of eigen functions with (g)-symmetry.

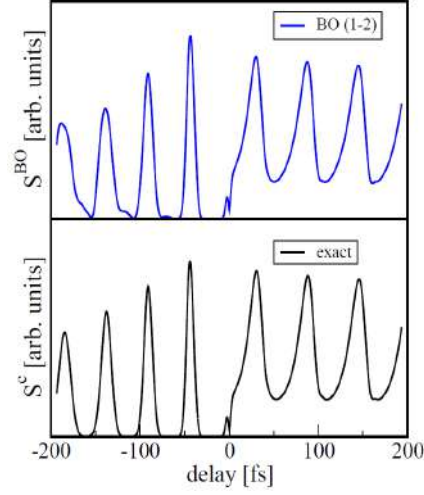


Fig 2. Comparison of DFWM-signals obtained within the Born-Oppenheimer approximation (upper panel) and for the coupled electron-nuclear motion (lower panel). Here, the weak coupling case $R_c = 1.5 \text{ \AA}$ is treated.

We now turn to the spectrum obtained from the exact calculation. The analytical expression corresponding to Eqs (22,24) are:

$$S_+^{(c)}(\tau) \sim \sum_{\alpha, \beta} \sum_{\alpha'} c(\alpha, \beta, \alpha', \beta) e^{i(E_{\alpha} - E_{\alpha'})\tau}, \quad (25)$$

$$S_-^{(c)}(\tau) \sim \sum_{\beta, \beta'} c(\beta, \beta') e^{i(E_{\beta} - E_{\beta'})\tau}, \quad (26)$$

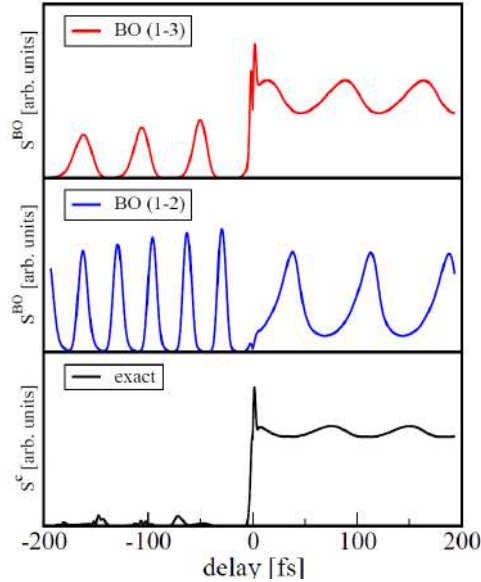


Fig 3. DFWM-signals for the strong coupling case ($R_c = 2.5 \text{ \AA}$). Curves obtained within the Born-Oppenheimer approximation are displayed for the $+$ transition in the upper panel and for the $-$ transition in the middle panel. The exact spectrum is shown in the lowest panel of the figure.

Here, we do not associate the energy levels with different electronic states (i.e., do not classify the energies by an electronic and nuclear quantum number). Thus, in principle, energy differences between arbitrary levels appear in the expression for the signal. This, however, is not the case for weak coupling ($R_c = 1.5 \text{ \AA}$) as can be seen from Fig 2. The exact spectrum, displayed in the lower panel of the figure agrees almost perfectly with the BO-spectrum. This manifests the expectation that the adiabatic approximation is valid and implies that the energy differences appearing in Eqs (25,26) can indeed be associated with vibrational energy differences in the excited or ground electronic state, respectively.

Next, the case of strong adiabatic coupling ($R_c = 2.5 \text{ \AA}$) is regarded. The lower panel of Fig 3 shows the exact spectrum. At negative delays, small-amplitude oscillations are seen. For positive delay times oscillations with a period of 75 fs occur on a large constant background signal. A comparison to the BO-signal calculated for laser-induced transitions between the states $|1\rangle$ and $|2\rangle$ (middle panel) shows that the spectra are not compatible with each other. This clearly demonstrates that, if only the lowest two electronic states are included, the BO-treatment fails.

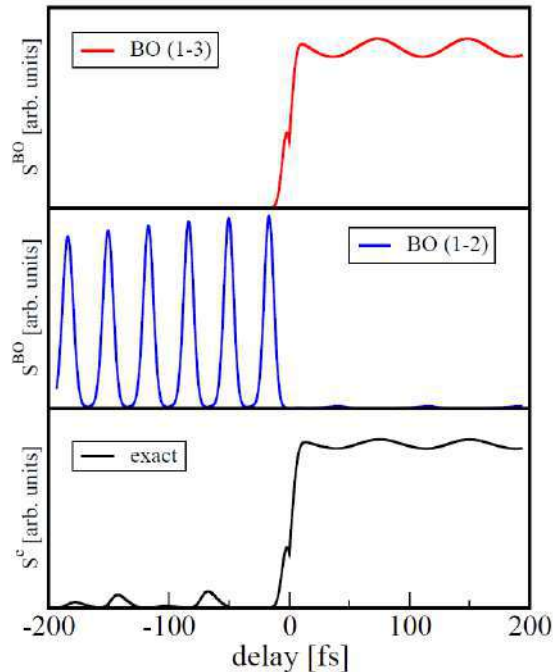


Fig 4. Same as Fig 3 but for longer laser pulses.

To clarify the importance of higher electronic states, we perform a BO-calculations for the $|1\rangle$ to $|3\rangle$ transition which has a much higher oscillator strength [33] than the one to the first excited state. The corresponding signal is displayed in the upper panel of Fig 3. It is seen that its time-dependence shows some characteristics of the exact signal. In particular the oscillations at positive delays have the same period and the background signal is also seen. This means that the use of the BO-approach involving the $|1\rangle$ to $|3\rangle$ states is a better (but still not a good) approximation than taking only the $|1\rangle$ to $|2\rangle$ states into account. We repeat the calculation using pulses of 10 fs width which leads to the spectra displayed in Fig 4. Because the transitions to state $|3\rangle$ are non-resonant, the respective signal (upper panel) is now suppressed at negative delays. Nevertheless, the ground-state dynamics (positive delays), including the background signal, is very well reproduced within the Born-Oppenheimer treatment of the $|1\rangle$ to $|3\rangle$ field coupled states. This is not true for the $|1\rangle$ to $|2\rangle$ transition (middle panel of Fig 4). Neither for positive nor for negative delays the signal resembles the exact one.

4 Conclusion

To conclude, we calculate femtosecond DFWM-signals which monitor the coupled electronic and nuclear dynamics in a model system. Employing different parameterization of the interaction potential, situations are established where a Born-Oppenheimer description of the dynamics is possible or fails. In the first case, the picture which was first established in experiments on I₂ molecules is recovered: The signal at negative pulse delays monitors the excited state vibrational dynamics whereas at positive delay times, the ground-state dynamics can be mapped. This interpretation breaks down, if strong non-adiabatic coupling is present. Then, the limitation to a two-state model with no non-adiabatic coupling is no longer possible. Even if more electronic states with non-zero oscillator strengths are included in the adiabatic approximation, the calculated signals cannot reproduce the results obtained if the complete coupled dynamics is taken into account.

5 Acknowledgement

We gratefully acknowledge financial support by the DFG within the FOR 1809.

References

1. Shen Y R, *The Principles of Nonlinear Opticals*, (Wiley, New York), 1982.
2. Mukamel S, *Principles of Nonlinear Optical Spectroscopy*, (Oxford University Press, New York), 1995.
3. Leonhardt R, Holzapfel W, Zinth W, Kaiser W, *Chem Phys Lett*, 133(1987)373-377.
4. Zinth W, Leonhardt R, Holzapfel W, Kaiser W, *IEEE J Quantum Electron*, 24(1988)455-459.
5. Purucker H.-G, Tunkin V, Laubereau A, *J Raman Spectrosc*, 24(1993)453-458.
6. Hayden C C, Chandler D W, *J Chem Phys*, 103(1995)10465.
7. Motzkus M, Pedersen S, Zewail A H, *J Phys Chem*, 100(1996)5620-5633.
8. Schmitt M, Knopp G, Materny A, Kiefer W, *Chem Phys Lett*, 270(1997)9-15.
9. Schmitt M, Knopp G, Materny A, Kiefer W, *Chem Phys Lett*, 280, (1997)339-347.
10. Schmitt M, Knopp G, Materny A, Kiefer W, *J Phys Chem A*, 102(1998)4059-4065.
11. Materny A, Chen T, Schmitt M, Siebert T, Vierheilg A, Engel V, Kiefer W, *Appl Phys B*, 71(2000)299-317.
12. Grimberg B I, Lozovoy V V, Dantus M, Mukamel S, *J Phys Chem A*, 106(2002)697-718.
13. Lang T, Frey H.-M, Beaud P, Motzkus M, *J Chem Phys*, 115(2001)5418-5426; doi.org/10.1063/1.1397325.
14. Meyer S, Schmitt M, Materny A, Kiefer W, Engel V, *Chem Phys Lett*, 281(1997)332-336.
15. Meyer S, Schmitt M, Materny A, Kiefer W, Engel V, *Chem Phys Lett*, 287(1998)753-754.
16. Meyer S, Schmitt M, Materny A, Kiefer W, Engel V, *Chem Phys Lett*, 301(1999)248-254.
17. M. Born and K. Huang, *Theory of Crystal Lattices*, (Oxford University Press, London), 1954.
18. Siebert T, Schmitt M, Engel V, Materny A, Kiefer W, *J Am Chem Soc*, 124(2002)6242-6243.
19. Siebert T, Maksimenka R, Materny A, Engel V, Kiefer W, Schmitt M, *J Raman Spectrosc*, 33(2002)844-854 .
20. Shin S, Metiu H, *J Chem Phys*, 102(1995)9285-9295; doi.org/10.1063/1.468795.
21. Erdmann M, Marquetand P, Engel V, *J Chem Phys*, 119(2003)672-679; doi.org/10.1063/1.1578618
22. Erdmann M, Gross E K U, Engel V, *J Chem Phys*, 121(2004)9666-9670.
23. Falge M, Engel V, Gräfe S, *J Chem Phys*, 134(2011)184307/1 - 184307/8.
24. Falge M, Engel V, Gräfe S, *J Phys Chem Lett*, 3(2012)2617-2620.
25. Abedi A, Agostini F, Suzuki Y, Gross E K U, *Phys Rev Lett*, 110(2013)263001/1-263001/5;doi.org/10.1103/PhysRevLett.110.263001
26. Agostini F, Abedi A, Suzuki Y, Gross E, *Mol Phys*, 111(2013)3625-3640.
27. Min S K, Abedi A, Kim K, Gross E, *Phys Rev Lett*, 113(2014)263004/1-263004/5;doi.org/10.1103/PhysRevLett.113.263004

28. Agostini F, Abedi A, Suzuki Y, Min S, Maitra N T, Gross E, *J Chem Phys*, 142(2015)084303; doi.org/10.1063/1.4908133.
29. Engel V, *Comput Phys Commun*, 63(1991)228-242.
30. Renziehausen K, Marquetand P, Engel V, *J Phys B: At Mol Opt Phys*, 42(2009)195402; doi.org/10.1088/0953-4075/42/19/195402.
31. Feit M D, Fleck J A, Steiger A, *J Comput. Phys*, 47(1982)412-433.
32. Domcke W, Stock G, *Adv Chem Phys*, 100(1997)1-169.
33. Erdmann M, Engel V, *J Chem Phys*, 120(2004)158-164; doi.org/10.1063/1.1629275.

[Received:18.09.2015; accepted:02.10.2015]



The accuracy of the M06L DFT method in the prediction of the vibrational Spectra of 4-amino-2-chlorobenzonitrile: A detailed interpretation of the Molecular Structure and vibrational IR and Raman spectra and other molecular properties using several DFT methods

M Alcolea Palafox^a, Anupama^b, Rachna Rastogi^{c*}, M Jane Alam^d, Daisy Bhat^e, and V K Rastogi^{c,e}

^a*Nofima AS - the Norwegian Institute of Food, Fisheries and Aquaculture Research, PB 210, N-1431 Ås, Norway.*

^b*Department of Chemistry, SRM University, NCR Campus, Modinagar-201 204, India.*

^c*Indian Spectroscopy Society, KC 68/1, Old Kavinagar, Ghaziabad-201 002, India.*

^d*Department of Physics, Aligarh Muslim University, Aligarh, India.*

^e*Internet Lab, R D Foundation Group of Institutions, NH-58, Kadarabad (Modinagar), Ghaziabad, India.*

Dedicated to Professor Wolfgang Kiefer on the occasion of his 75th birthday

The accuracy of the M06L DFT method in the prediction of the vibrational spectra of 4-amino-2-chlorobenzonitrile molecule was tested and compared with that of the B3LYP method. The experimental FT-IR and FT-Raman spectra in the solid state were recorded at room temperature, and the bands assigned with accuracy by comparison with the results obtained by different methods, including MP2 and DFT. The FT-IR spectrum in Nujol mull was also recorded and analyzed. Several scaling procedures were used and several recommendations were presented. The wavenumbers of most of the modes were found in the expected range and the error obtained was in general very low. The thermodynamic parameters were calculated and discussed. The NBO analysis was done and Molecular Electrostatic Potential (MEP) was plotted. The calculated HOMO and LUMO energies showed that charge transfer occurs within the molecule. Several general conclusions were deduced. © Anita Publications. All rights reserved.

Keywords: M06L DFT method; FT-IR and FT-Raman spectra; Molecular Electrostatic Potential (MEP); HOMO and LUMO.

1 Introduction

The theoretical prediction of vibrational spectra is of practical importance and has become an important part of spectrochemical and quantum chemical investigations. A variety of different approaches combining the theoretical and experimental results for predicting accurate vibrational wavenumbers have been suggested and reviewed by us [1-3]. However, the accuracy of one of the new DFT methods, the M06L, has not been tested yet from the spectroscopic point of view. Thus, the main aim of the present manuscript was to present scaling equations to be used with this method and to determine the accuracy obtained with them in a simple BN derivative, the 4-amino-2-chlorobenzonitrile molecule (4A-2CBN), which has not been analyzed yet completely. Thus all the results obtained in the present study are being reported for the first time.

4A-2CBN molecule was selected for the present study because of the interesting biochemical and physical properties of benzonitrile (in short BN) and its amino derivatives. Substituted benzonitriles have been studied extensively due to their wide applications in various fields, e.g. they are used in the

Corresponding author :

e-mail: alcolea@ucm.es (M Alcolea Palafox); v_krastogi@rediffmail.com (V K Rastogi)

manufacturing of polymers and anhydrous metallic salts and as well as intermediates for pharmaceuticals, agrochemicals, pesticides and other organic chemicals [4-8], and also they have many other important applications [9-12]. Several halogen derivatives are well known herbicides since 1960s, and it was found that benzonitriles, substituted at the 2 and 6 positions by halogen or methyl, had the highest herbicidal activity. 2,6-dichlorobenzonitrile (2,6-DCBN) is a contact herbicide which controls broadleaf weeds in grass type crops and in cranberry bogs. Some 2,6-dichloro-1-substituted benzene derivatives showed herbicidal activity, comparable with that of 2,6-dichlorobenzonitrile. 2,6-difluorobenzamide, a fluorinated derivative of DCBN, is used to synthesize benzyl urea like pesticides. Due to the high electro-negativity of chlorine atom, entirely different physical and chemical properties are observed in these compounds as compared to the other halogenated derivatives [13-16].

Although numerous experimental studies using the IR and Raman spectroscopic techniques, and theoretical ones have been made in recent years on the vibrational spectra of BN and its mono- and di-substituted derivatives [17-36], however, as far as we know, no structural data and a complete rigorously studied vibrational analysis on 4A-2CBN molecule, Fig 1, are available in literature yet [37]. Therefore, the another aim of the present work is to analyze in detail for the first time the molecular geometry and vibrational spectra of this molecule. The assignments and interpretation of the experimental IR and Raman bands are based on DFT calculations and accurate scaling. Also, the results of the NLO properties, MEP mapping and HOMO-LUMO analysis for the title compound are discussed for the first time. The importance of this molecule may be seen from the fact that the substituted benzonitriles are finding increasing applications in a variety of fields.

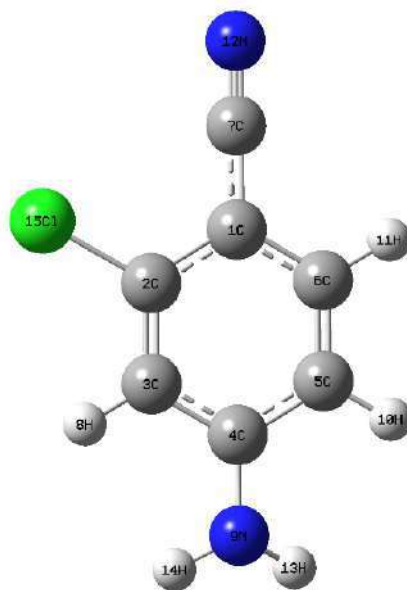


Fig 1. Label of the atoms in 4A-2CBN molecule.

2 Experimental

The compound 4A-2CBN ($C_7H_5ClN_2$) of spectral grade in solid state was purchased from M/s Aldrich Chemicals (Milwanke, WI USA) and used as such without any further purification. The FTIR spectrum of this compound in KBr pellet (with 1 mg sample per 300 mg KBr) was measured on a Perkin Elmer FT-IR Model 1760 X, while the infrared spectrum in nujol mull was recorded on Nicolet DX spectrometer. The spectra are shown in Figs 2-3.

The FT-Raman spectrum was measured on a Nicolet Raman 950 instrument operating at room temperature. The spectrum was recorded in powder form in the region of 3500-0 cm^{-1} . The spectrum was accumulated by acquisition of 400 scans at a fixed temperature. The sample was mounted in the sample illuminator using an optical mount and no sample pretreatment was undertaken. The NIR output (1064 nm) of an Nd:YAG laser was used to excite probe. The instrument was equipped with InGaAs detector. The instrument was set at 250 mW. The spectra are shown in Figs 4-5.

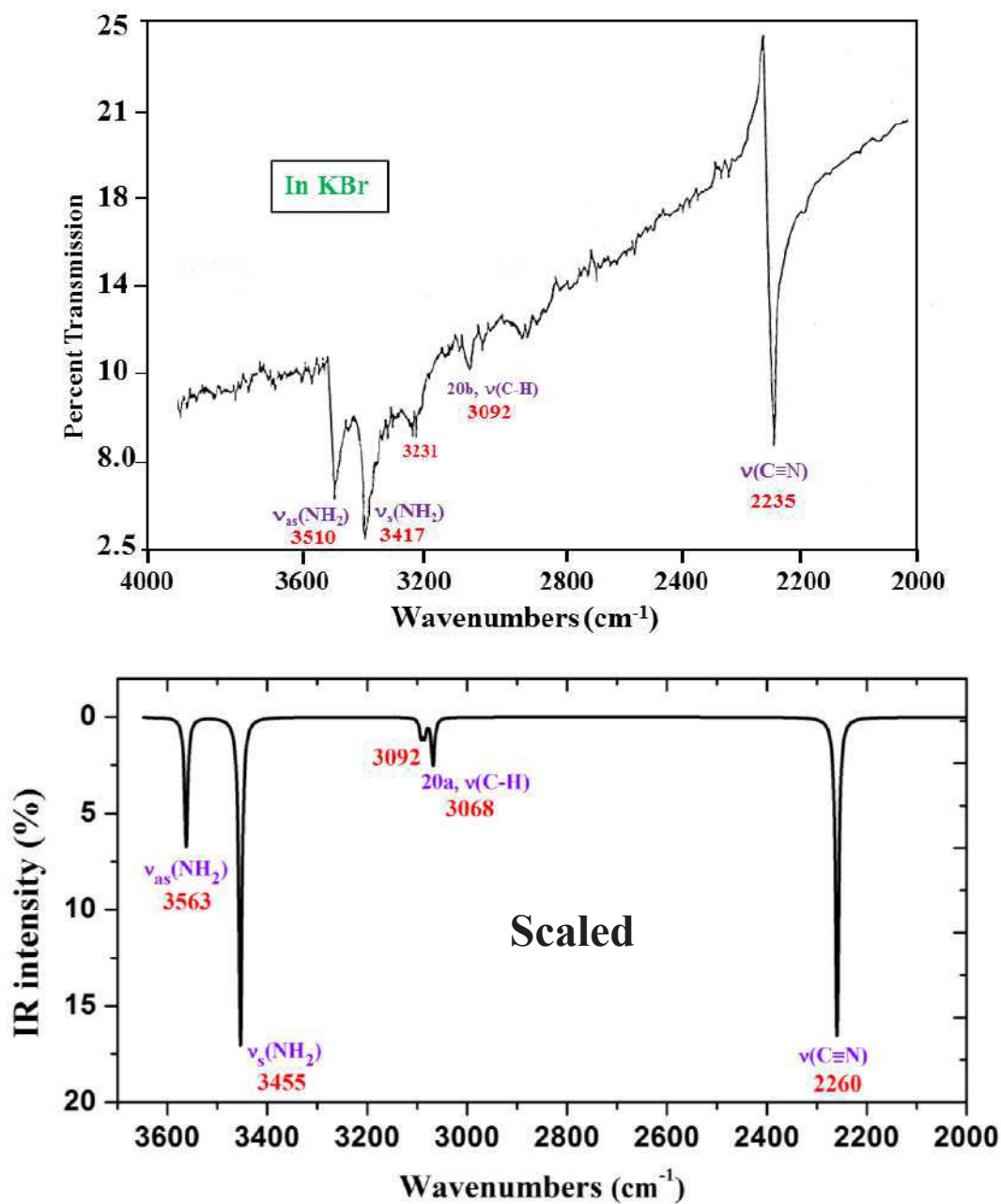


Fig 2. Calculated (scaled) and experimental IR spectra of 4A-2CBN in the region 4000-2000 cm^{-1} in KBr matrix

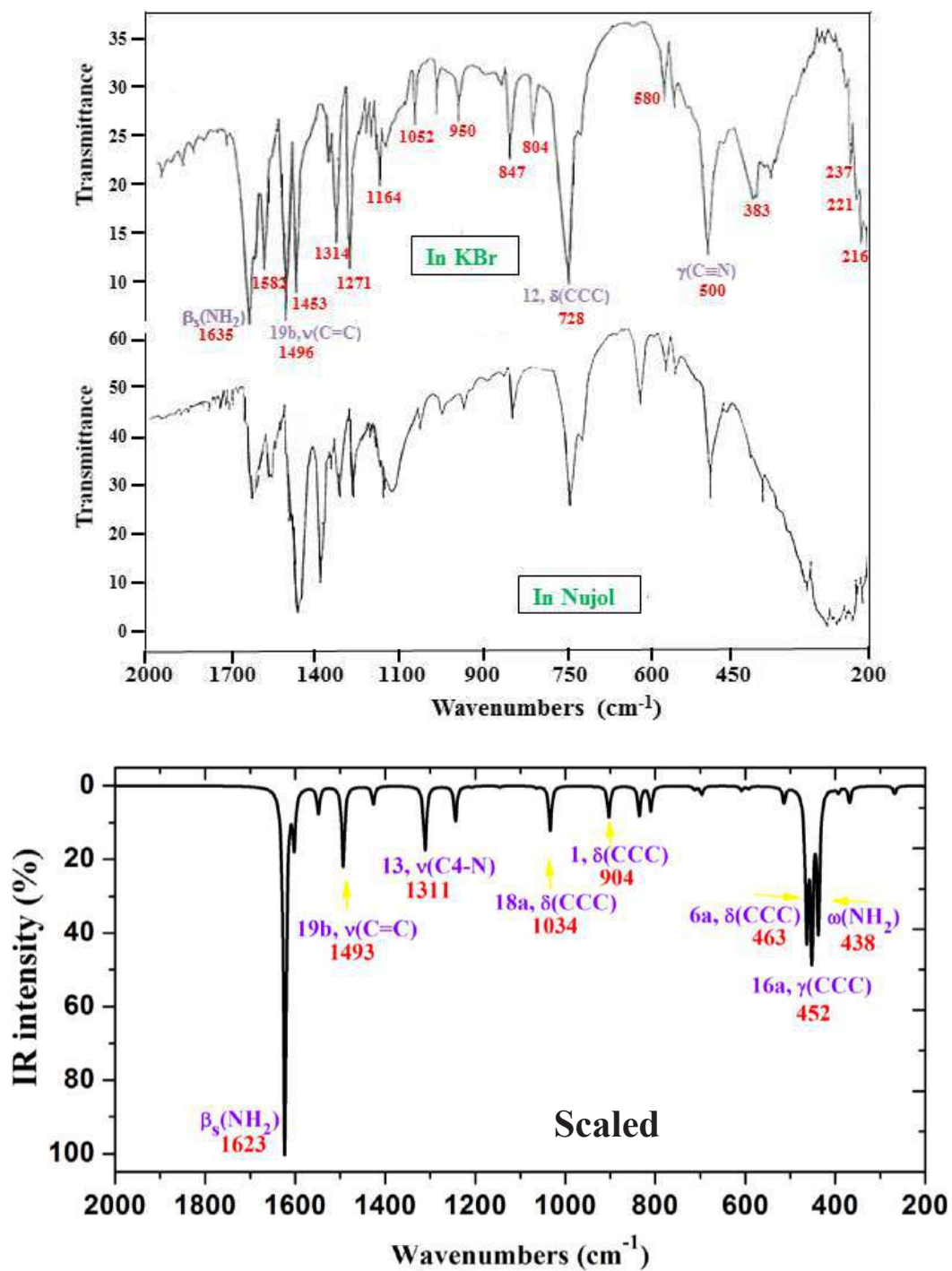


Fig 3. Experimental IR spectra of 4A-2CBN molecule in the 2000-200 cm⁻¹ range in KBr and Nujol matrix, and theoretical scaled spectrum using the scale equation procedure.

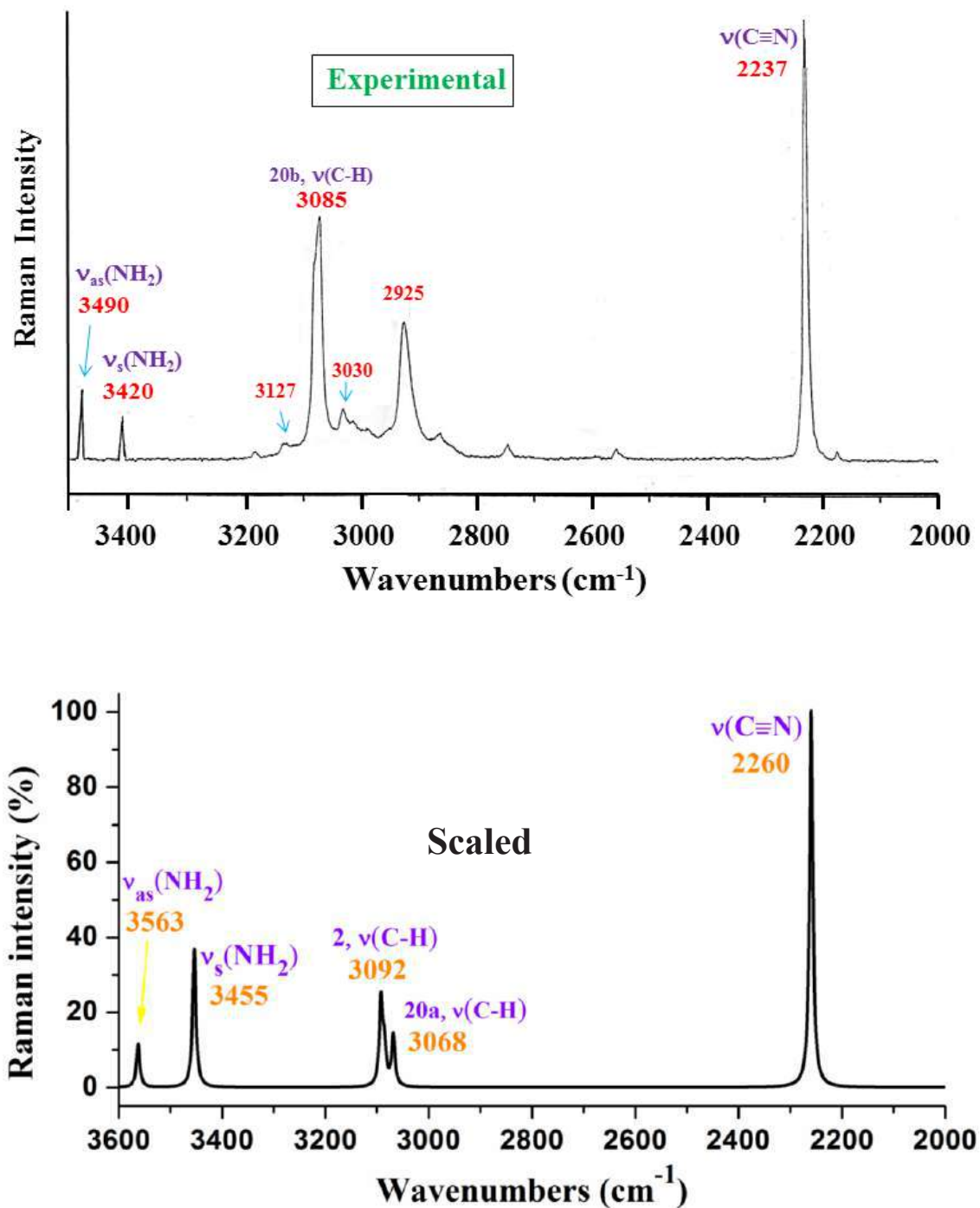


Fig 4. Experimental and theoretical scaled Raman spectrum in the 3500-2000 cm^{-1} range using the scale equation procedure with benzene molecule.

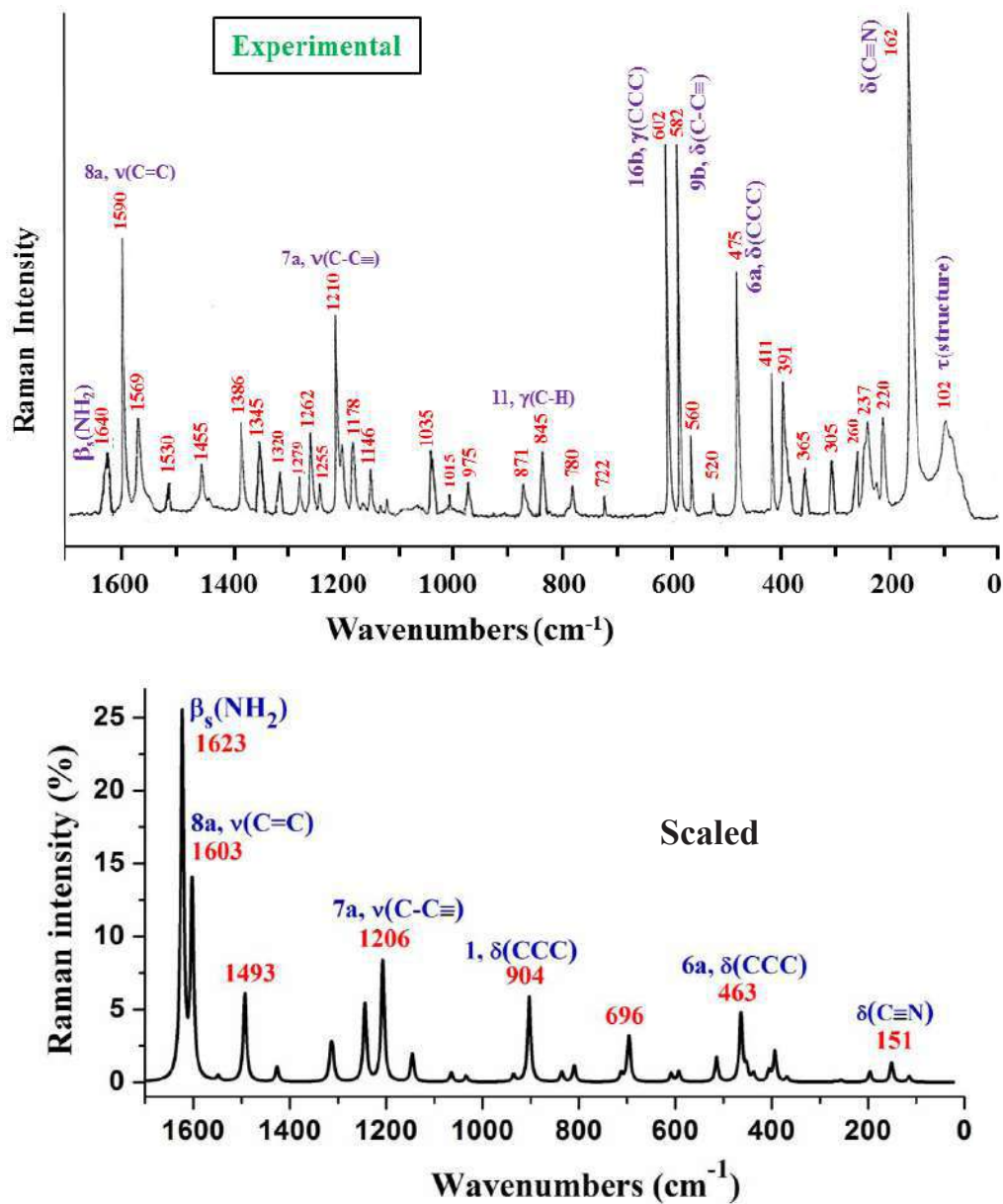


Fig 5. Experimental and theoretical scaled Raman spectrum in the 1700-0 cm⁻¹ range using the scale equation procedure with benzene molecule.

3 Computational details

Ab initio HF (Hartree-Fock), MP2 (second-order Møller-Plesset) and DFT methods are most commonly used for the calculations of vibrational normal modes of a molecule to interpret and understand its experimental vibrational (infrared and Raman) spectra. In the calculations done by these methods, the effect of anharmonicity on both the vibrational frequencies and on the IR and Raman intensities is neglected. Therefore, the calculated harmonic frequencies and IR and Raman intensities, in many cases, are not in good

agreement with the experimentally observed IR and Raman spectra [38]. In the present study, the density functional theoretical (DFT) computations [39] were performed because they provide a very good overall description of medium-size molecules. Moreover, for the wavenumber calculations [1-3,40] they appear more accurate than HF and MP2, and at lower computational cost.

Mainly, three levels of theory have been used for geometry optimisation and calculations of vibrational wavenumbers: B3LYP/6-31G(d,p), B3LYP/6-311++G(3df,pd), and M06-L/6-31G(d,p). Among the DFT methods, B3LYP is the most popular, and it has been used satisfactorily in many studies of DNA components [41-46], of drug designing [47-49], and of several other important molecules [50-54]. With these methods and basis sets we have recently studied the geometry, and molecular properties of a series of chlorobenzonitriles and difluorobenzonitriles [32,33, 54-57].

In the present study, the results obtained by B3LYP method were compared with those obtained with the new method M06L [58] available today in Gaussian 09 [59] program package, and developed by Zhao *et al* [60]. M06L generally yields good results for a broad range of interactions, including non-covalent interactions [58,60]. However, the accuracy of M06L in the calculation of the vibrational wavenumbers has not been tested yet, although several studies with M06 method have been reported [61].

The geometry structure and atomic charges calculated by DFT methods were confirmed by using *ab initio* MP2 calculations. For comparison purposes the natural NBO atomic charges [62,63] were also calculated in BN molecule.

Molecular geometries were fully optimized by Berny's optimization algorithm in redundant internal co-ordinates, and with the standard optimization convergence criteria. Imaginary frequencies were not found in the vibrational analysis which proves that the geometries determined belong to a true minimum. The harmonic approximation was used at the same level of theory that the optimized geometry. Visualization and checking of calculated data were done by using the Gauss View 4.1 program for the stable form of the molecule.

Raman scattering activities (S_i) calculated by Gaussian 09 program were suitably converted to relative Raman intensities (I_i) using the following relationship derived from the basic theory of Raman scattering [64-66]:

$$I_i = \frac{f(\nu_0 - \nu_i)^4 S_i}{\nu_i [1 - \exp(-h\nu_i / kT)]}$$

where f is the suitable chosen common scaling factor for all the peak intensities, ν_0 is the laser exciting frequency (cm^{-1}); in this work we have used the exciting wavenumber $\nu_0 = 9938.5$ (which corresponds to the wavelength of 1064 nm of a Nd:YAG laser), ν_i is the vibrational wavenumber of the i th normal mode, and h , c and k are universal constants.

4 Results and discussion

4.1 Geometry Optimization

The optimized bond lengths, bond angles and torsional angles determined by the different theoretical methods in the isolated state of 4A-2CBN molecule are listed in the 2nd to 5th columns of Table 1, while the labeling of the atoms is plotted in Fig 1. Although X-ray experimental data on 4A-2CBN has not been reported yet, however, the calculated values with the different methods were, in general, in accordance to the microwave data reported for the molecule of BN [67], to the X-ray values in 4-aminobenzonitrile (4ABN) [55b-d], and to the computed values in several BN derivatives [25,26]. In the crystal of the solid state, the molecules of 4A-2CBN are expected to be connected to a three-dimensional network, as reported in 4ABN [68-70], and to form intermolecular H-bonds between an amino H-atom and the cyano group of a neighboring molecule, with classical hydrogen bonds of the N-H...N type. As a consequence, an unexpected

small deviation from co-planarity for the phenyl and cyano groups can be predicted. Also, in the crystal the cyano group is expected to appear bent towards the substituent amino group.

Table 1. Optimized geometrical parameters at B3LYP, M06L and MP2 levels in 4A-2CBN and benzonitrile (BN) molecules.

Parameters	4A-2CBN				BN	
	B3LYP/ 6-31G(d,p)	B3LYP/ 6-311++G(3df,pd)	M06L/ 6-31G(d,p)	MP2/ 6-31G(d,p)	B3LYP/ 6-31G(d,p)	MP2/ 6-31G(d,p)
<i>Bond lengths</i>						
C1-C2	1.408	1.403	1.407	1.404	1.405	1.403
C2-C3	1.387	1.382	1.384	1.39	1.392	1.393
C3-C4	1.408	1.401	1.404	1.402	1.397	1.397
C4-C5	1.41	1.404	1.407	1.405	1.397	1.397
C5-C6	1.383	1.378	1.38	1.387	1.392	1.393
C6-C1	1.409	1.402	1.406	1.404	1.405	1.403
C1-C7	1.428	1.423	1.42	1.43	1.435	1.436
C2-Cl	1.749	1.734	1.734	1.734	-	-
C4-N	1.38	1.377	1.374	1.392	-	-
C≡N	1.164	1.153	1.169	1.184	1.163	1.184
<i>Bond angles</i>						
C2-C1-C6	117.6	117.8	117.5	118.5	120.1	120.5
C-C2-C	121.5	121.2	121.5	120.8	119.7	119.4
C-C3-C	120.3	120.5	120.2	120.5	120.2	120.3
C-C4-C	118.7	118.7	118.8	118.9	120.2	120.1
C-C5-C	120.3	120.3	120.3	120.4	120.2	120.3
C-C6-C	121.5	121.5	121.6	120.9	119.7	119.4
C2-C1-C7	122.5	122.3	122.1	121.7	120	119.7
C6-C1-C7	119.9	119.9	120.4	119.8	120	119.7
C1-C2-Cl	120	120.1	119.7	120.3	-	-
C3-C2-Cl	118.5	118.7	118.8	119	-	-
C3-C4-N	120.4	120.4	120.3	120.3	-	-
C5-C4-N	120.8	120.8	120.8	120.6	-	-
C-C≡N	179.9	178.1	178.3	178.3	180	180
H-N-H	114	114.2	113.8	111.4		
ε tilt angle	2	2.1	1.4	4.6		
ω (inversion)	32.5	31.5	33.3	42.1		
<i>Torsional angles</i>						
C2-C-C4-N	177.6	177.7	177.4	177		
C3-C-N-H14	20.3	19.6	20.6	26.9		
C5-C-N-H13	-20.5	-19.7	-21.3	-27.6		

Two optimum conformations were determined in 4A-2CBN molecule, with the planar form of the -NH₂ group being saddle point. Thus, the data on this conformer were omitted in the present manuscript. With the exception of this -NH₂ group, in the stable form the molecule is completely planar. The nitrogen atom is ca. 0.10 Å above the plane of the phenyl ring (at MP2 level) with both hydrogen atoms in opposite directions.

Phenyl-ring structure

As compared to MP2 values, the calculated C-C bond lengths by B3LYP appear with the same accuracy as that by M06L. However, the C-C1 bond length computed by M06L has the same value as that by MP2, while by B3LYP/6-31G(d,p) it is 0.015 Å longer. The calculated C≡N bond length by B3LYP and M06L are noticeably lower than by MP2, i.e. these methods (B3LYP and M06L) appear to fail in the calculation of C≡N bond length, although the difference is larger by B3LYP than by M06L.

For comparison purposes the values obtained in BN molecule were also collected in the 6th-7th columns of Table 1. The broad features observed by the replacement of the hydrogens in positions 2 and 4 of the BN moiety by chlorine and amino substituents, respectively, can be described as follows:

(i) The effect of the chlorine atom on the ring bond lengths is small; at the MP2 level the C1-C2 and C1-C6 bonds have the same value, while C2-C3 is only 0.003 Å longer than C5-C6. The effect on the angles is also very small or almost null, with very close value for C1-C2-C3 and C1-C6-C5.

(ii) The increment of the lengths in the C-C bonds adjacent to C1-C7 and C4-N10 is accompanied by slightly irregular hexagonal structure, measured in the *ipso* angles C2-C1-C6 and C3-C4-C5, with values at the MP2/6-31G(d,p) level of 118.5° and 118.9°, respectively. These values are in agreement with that calculated at the same level by us in the aniline molecule [71], 118.84°, but in contrast with the very small change calculated in BN, 120.5°. This feature indicates that the C≡N substituent alone does not have any effect on its *ipso* angle.

(iii) The ring structure appears a little distorted. It shows a quinonoid structure, and thus with C1-C2 (C1-C6) and C3-C4 (C4-C5) bond lengths (1.40 Å at the MP2 level) longer than the C2-C3 (C5-C6) bonds, 1.39 Å. This effect is larger by DFT methods than by MP2. This quinonoid form is characteristic of BN molecule, with a C2-C3 bond length of 1.393 Å by MP2, and it remains in 4ABN with a value of 1.389 Å for this bond.

(iv) The ring angles at the C1 and C4 sites of substitution appear slightly closing, which leads to an opening of the angles at the vicinal C2 (C6) and very slightly at C3 (C5) atom positions.

(v) All the distortions can be explained in terms of the change in hybridization affected by the substituent at the carbon site to which it is appended. Thus, the ring angles obtained in 4A-2CBN can be reasonably explained by the superposition of the ring angular distortions of *ortho*-chlorobenzene, *para*-aminobenzene and BN, although the effect of the chlorine atom is small due to its low positive charge. It is as follows: starting from the symmetrical structure of benzene ring, the angle decreases slightly at the site of the -C≡N and -NH₂ substitutions and increases by ca 0.4–0.9° at adjacent positions. This is due to the electronegative C≡N substitution, which leads to a lengthening of the nearest C1-C2 bond and shortening of the vicinal C2-C3 (C6-C5) bonds, as observed in BN molecule, although with lower values.

(vi) The chlorine atom has no influence on the planarity of the structure. Thus, with the exception of the NH₂ group, 4A-2CBN is a planar molecule, as BN, i.e. all the ring torsional angles with values 0 or 180°.

(vii) The chlorine atom withdraws negative charge (0.22 *e*⁻ by MP2, where *e*⁻ is the charge of an electron) from the bonded C2 atom, which therefore changes to a small and positive value, Table 2. The effect of the NH₂ group is small on this atom, only there is a slight decrease in the negative charge, upto -0.126 *e*⁻.

The C–X and C≡N bonds

A notable difference in the computed C≡N and C4–N10 bond lengths is observed by the different methods used in the present study. At the MP2 level, the nitrile (C≡N) bond length is 1.184 Å, while by M06L it is 1.169 Å and by B3LYP/6-311++G(3df,pd) is 1.153 Å. For C4–N10 bond length, the differences are also large, with values 1.392 Å by MP2, 1.374 Å by M06L, and 1.377 Å by B3LYP6-311++G(3df,pd).

A small effect due to the chlorine atom on the C1–C7 bond length is observed (1.430 Å by MP2 in 4A-2CBN), which is slightly shorter as compared to BN (1.436 Å) and 4ABN (1.434 Å). The small reduction in 4ABN is mainly due to the –NH₂ group, which is a donor substituent on the ring. As the C≡N group remains almost unchanged, therefore, the substituents have no effect on the C≡N bond length.

Table 2. Calculated natural NBO atomic charges at B3LYP and MP2/6-31G(d,p) levels in 4A-2CBN and BN molecules.

Atom	4A-2CBN				BN	
	B3LYP/6-31-G(d,p)	B3LYP/6-311-++G(3df,pd)	M06L/6-31-G(d,p)	MP2/6-31-G(d,p)	B3LYP/6-31-G(d,p)	MP2/6-31-G(d,p)
C1	–0.224	–0.249	–0.223	–0.257	–0.171	–0.188
C2	0.012	0.021	0.013	0.051	–0.189	–0.17
C3	–0.302	–0.275	–0.306	–0.326	–0.235	–0.239
C4	0.203	0.202	0.213	0.275	–0.216	–0.198
C5	–0.291	–0.255	–0.293	–0.317	–0.235	–0.239
C6	–0.161	–0.114	–0.163	–0.113	–0.189	–0.17
C7	0.277	0.288	0.291	0.326	0.28	0.328
H8	0.256	0.22	0.252	0.254	0.247	0.243
N9	–0.827	–0.772	–0.835	–0.887	–	–
H10	0.245	0.21	0.241	0.243	0.247	0.243
H11	0.261	0.222	0.259	0.258	0.249	0.244
≡N	–0.305	–0.315	–0.322	–0.356	–0.305	–0.361
H13	0.414	0.383	0.42	0.412	–	–
H14	0.414	0.383	0.42	0.412	–	–
Cl	0.03	0.049	0.033	0.025	–	–

Although between 4A-2CBN and 4ABN, the differences in the C1–C7 and C–C bond lengths are small, however in the C4–N bond of the amino group, the difference is significant, and it is 1.392 Å in 4A-2CBN vs. 1.383 Å in 4ABN by MP2. This difference is due to the chlorine atom. The difference between 4ABN and aniline [72] is also significant. Thus, in 4ABN, the C4–N bond is shortened (1.383 Å vs 1.406 Å of aniline molecule), leading to a lower pyramidal character (more *sp*²) of the –NH₂ group, i.e. shortening of the N–H bond (1.010 Å in aniline molecule), opening of the C–N–H and H–N–H angles (113.0 and 109.8°, respectively in aniline), and lower inversion angle ω (34.7° in 4ABN vs 47.2° in aniline) and *tilt* angle ε (4.4° in aniline). This planarization of the amino group in 4ABN has been interpreted [68] due to resonance with the aromatic system.

4.2. Scaling the wavenumbers

The use of adequate quantum chemical methods and scaling procedures, compensates the calculated harmonic wavenumbers to be compared with the anharmonic wavenumbers found by the experiment (IR and Raman spectra) [73,74], and remarkably reduce the risk in the assignment of bands. The procedure selected for scaling the wavenumber depends on the size of the organic molecule and the accuracy required for the predicted wavenumber. In the present study following three scaling procedures were used:

(i) The linear scaling equation procedure (LSE), which employs the linear scaling equation calculated in the benzene molecule at the same level, that are the following:

$$\begin{aligned} \nu^{\text{scaled}} &= 22.1 + 0.9543 \cdot \omega^{\text{calculated}} && \text{for B3LYP/6-31G(d,p) level, from [1,2]} \\ \nu^{\text{scaled}} &= 23.6 + 0.9528 \cdot \omega^{\text{calculated}} && \text{for B3LYP/6-31G(d,p) level} \\ \nu^{\text{scaled}} &= 31.2 + 0.9515 \cdot \omega^{\text{calculated}} && \text{for B3LYP/6-311++G(3df,pd) level} \\ \nu^{\text{scaled}} &= 29.7 + 0.9502 \cdot \omega^{\text{calculated}} && \text{for M06L/6-31G(d,p) level} \end{aligned}$$

The results are presented in Table 3. The calculated equation in the benzene molecule with the M06L method has a worse correlation coefficient r .

For the NH_2 vibrations, we used the following scaling equation which was obtained from the amino group of aniline molecule:

$$\begin{aligned} \nu^{\text{scaled}} &= 44.5 + 0.9441 \cdot \omega^{\text{calculated}} && \text{for B3LYP/6-31G(d,p) level, from [72]} \\ \nu^{\text{scaled}} &= 38.4 + 0.9367 \cdot \omega^{\text{calculated}} && \text{for M06L/6-31G(d,p) level} \end{aligned}$$

Figures 2-5 show the experimental IR and Raman spectra, together with their simulated scaled spectra using the LSE procedure at the B3LYP/6-31G(d,p) level of theory.

(ii) The two linear scaling equations, one from 0-1000 cm^{-1} , and another one from 1000-4000 cm^{-1} . The equations used, presented for the first time here, were:

$$\begin{aligned} \nu^{\text{scaled}} &= -21.0 + 1.0102 \cdot \omega^{\text{calculated}} && \text{for the 0-1000 } \text{cm}^{-1} \text{ range and B3LYP/6-31G(d,p)} \\ \nu^{\text{scaled}} &= 32.5 + 0.9490 \cdot \omega^{\text{calculated}} && \text{for the 1000-4000 } \text{cm}^{-1} \text{ range and B3LYP/6-31G(d,p)} \\ \nu^{\text{scaled}} &= -19.3 + 1.0157 \cdot \omega^{\text{calculated}} && \text{for the 0-1000 } \text{cm}^{-1} \text{ range and M06L/6-31G(d,p)} \\ \nu^{\text{scaled}} &= 37.0 + 0.9469 \cdot \omega^{\text{calculated}} && \text{for the 1000-4000 } \text{cm}^{-1} \text{ range and M06L/6-31G(d,p)} \end{aligned}$$

(iii) The polynomial scaling equation, $y = a + b_1x + b_2x^2$ where “y” is the scaled frequency, “x” is the calculated frequency, and “a”, “ b_1 ” and “ b_2 ” are coefficients determined in the benzene molecule. This scaling equation procedure is new and its accuracy has not been reported yet

$$\begin{aligned} \nu^{\text{scaled}} &= -4.3 + 0.9923 \cdot \omega^{\text{calculated}} - 10.03 \cdot 10^{-6} \cdot (\omega^{\text{calculated}})^2 && \text{for B3LYP/6-31G(d,p) level} \\ \nu^{\text{scaled}} &= 3.6 + 0.9871 \cdot \omega^{\text{calculated}} - 9.39 \cdot 10^{-6} \cdot (\omega^{\text{calculated}})^2 && \text{for M06L/6-31G(d,p) level} \end{aligned}$$

4.3 Analysis of the different vibrations

In order to have the spectroscopic signatures of 4A-2CBN molecule, we performed calculations using B3LYP/6-31G(d,p), B3LYP/6-311++G(3df,pd), and M06-L/6-31G(d,p) methods. It is worthwhile to note that calculations were performed in gas phase, whereas spectra were recorded in solid samples, therefore there are some disagreements between calculated and observed vibrational wavenumbers. Table 3 collects the theoretical (calculated) results. The first column lists the computed wavenumbers at the B3LYP/6-31G(d,p) level in decreasing order, while the second column shows their respective relative IR intensities (A), and relative Raman scattering activities (S), third column. The relative IR and Raman intensities were determined by dividing the computed values by the intensity of the strongest ones at 1678 and 2345 cm^{-1} , respectively.

Table 3. Calculated harmonic wavenumbers (ω , cm^{-1}), relative infrared intensities (A, %), relative Raman scattering activities (S, %), Raman depolarization ratios for plane (P) and unpolarized (U) incident light, reduced mass (μ , amu), and force constant ($\text{mdyn}\cdot\text{\AA}^{-1}$, f) obtained in 4A-2CBN at different computational levels.

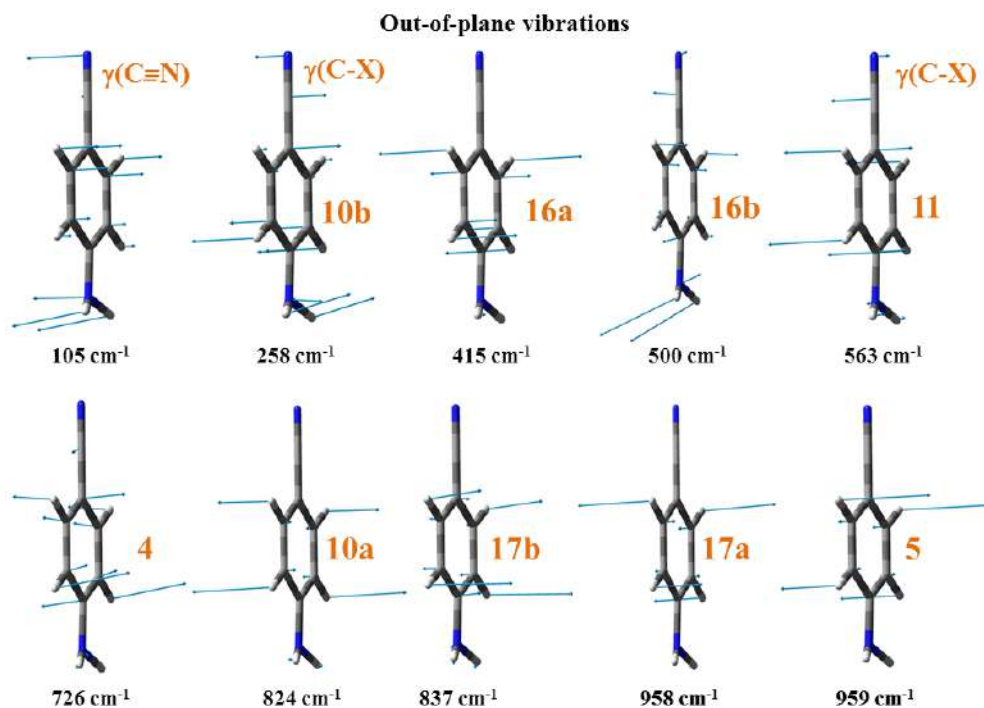
ω	B3LYP/6-31G(d,p)			B3LYP/6-311++G(3df,2pd)			M06L/6-31G(d,p)			MP2/6-31G(d,p)			Characterization
	A	S	ω	A	S	ω	U	P	μ	f	ω	ω	
3217	1	28	3202	1	22	0.19	0.32	0.19	1.1	6.6	3228	3279	100%, 2, $\nu(\text{C-H})$ in C5-H, C6-H
3209	1	12	3194	1	9	0.27	0.42	0.27	1.1	6.6	3219	3268	100%, 20b, $\nu(\text{C-H})$ in C3-H
3192	2	17	3178	3	13	0.43	0.60	0.43	1.1	6.5	3211	3259	100%, 20a, $\nu(\text{C-H})$ in C5-H, C6-H
1657	15	11	1643	50	16	0.55	0.71	0.55	3.1	5.0	1669	1688	51%, 8a, $\nu(\text{C=C})$ + 48%, $\beta_3(\text{NH}_2)$
1599	7	0	1585	9	0	0.36	0.53	0.36	6.0	8.9	1607	1639	98%, 8b, $\nu(\text{C=C})$
1541	22	5	1529	31	4	0.38	0.55	0.38	3.1	4.3	1550	1564	94%, 19b, $\nu(\text{C=C})$
1471	5	1	1461	6	1	0.41	0.58	0.41	3.0	3.8	1486	1502	97%, 19a, $\nu(\text{C=C})$
1355	2	2	1338	12	1	0.47	0.64	0.47	2.5	2.7	1389	1446	97%, 14, $\nu(\text{C=C})$
1351	16	1	1331	13	2	0.27	0.43	0.27	6.1	6.4	1364	1362	81%, 13, $\nu(\text{C4-N, CCC})$ + 18%, $\delta(\text{NH}_2)$
1280	10	4	1277	18	4	0.16	0.27	0.16	1.8	1.8	1280	1302	94%, 3, $\delta(\text{C-H})$
1241	0	7	1234	0	6	0.18	0.30	0.18	2.6	2.3	1247	1253	85%, 7a, $\nu(\text{C-C=, CCC})$ + 13%, $\nu(\text{C}\equiv\text{N})$
1177	0	2	1175	1	1	0.18	0.30	0.18	1.3	1.0	1175	1195	100%, 18b, $\delta(\text{C-H})$
1060	12	0	1058	15	0	0.08	0.15	0.08	3.2	2.1	1070	1084	92%, 18a, $\delta(\text{C-H, CCC})$
958	0	0	972	0	0	0.72	0.83	0.72	1.3	0.7	951	942	99%, 5, $\gamma(\text{C-H})$ in C5-H, C6-H
924	8	4	922	10	5	0.06	0.11	0.06	5.3	2.7	936	882	70%, 1, $\delta(\text{CCC})$ + 12%, $\delta(\text{NH}_2)$ + 10% $\nu(\text{C-CL})$
852	8	0	872	8	0	0.31	0.48	0.31	1.6	0.7	847	806	95%, 17b, $\gamma(\text{C-H})$ in C3-H
826	7	1	830	9	0	0.60	0.75	0.60	1.5	0.6	813	780	95%, 11, $\gamma(\text{C-H})$ in C5-H, C6-H
724	1	0	724	0	0	0.31	0.47	0.31	3.9	1.2	730	730	55%, 12, $\delta(\text{CCC})$ + 30%, $\delta(\text{C}\equiv\text{N})$ + 13%, $\delta(\text{NH}_2)$
711	0	0	721	2	0	0.09	0.17	0.09	5.3	1.6	710	714	90%, 4, $\gamma(\text{CCC, C-C}\equiv)$
706	2	2	707	2	2	0.13	0.24	0.13	7.2	2.1	714	629	77%, 6b, $\delta(\text{CCC})$ + 14%, $\nu(\text{C-CL})$
614	1	1	619	3	0	0.75	0.86	0.75	3.5	0.8	611	589	88%, 16b, $\gamma(\text{CCC})$ + 10%, $\gamma(\text{C}\equiv\text{N})$
598	1	0	608	1	0	0.08	0.14	0.08	7.1	1.5	608	556	53%, 9b, $\delta(\text{C-C}\equiv, \text{CCC})$ + 32%, $\delta(\text{C}\equiv\text{N})$
462	38	3	461	15	3	0.18	0.30	0.18	3.9	0.5	461	459	40%, 6a?, $\delta(\text{C4-N, CCC})$ + 37%, $\omega(\text{NH}_2)$ + 16%, $\delta(\text{C}\equiv\text{N})$
451	43	1	448	22	0	0.70	0.83	0.70	2.9	0.3	438	432	39%, 16a, $\gamma(\text{CCC})$ + 38%, $\omega(\text{NH}_2)$ + 15%, $\gamma(\text{C}\equiv\text{N})$
401	0	0	403	0	0	0.26	0.42	0.26	4.1	0.4	404	398	48%, 15, $\delta(\text{C4-N, CCC})$ + 27%, $\delta(\text{C}\equiv\text{N})$ + 20%, $\delta(\text{NH}_2)$
389	2	1	391	2	1	0.60	0.75	0.60	13.5	1.2	395	390	45%, 7b, $\nu(\text{C-CL})$ + 38%, $\delta(\text{C}\equiv\text{N})$ + 17%, $r(\text{NH}_2)$
258	2	0	256	3	0	0.50	0.67	0.50	5.5	0.2	257	246	65%, 10b, $\gamma(\text{C4-N, CCC})$ + 28%, $\gamma(\text{C}\equiv\text{N})$
245	0	0	246	0	0	0.70	0.83	0.70	6.3	0.2	245	245	60%, 9a, $\delta(\text{C-CL, ring})$ + 21%, $\delta(\text{C}\equiv\text{N})$ + 19%, $r(\text{NH}_2)$
182	0	0	181	0	0	0.75	0.86	0.75	5.2	0.1	176	178	74%, 10a, $\gamma(\text{C-CL, ring})$ + 19%, $\gamma(\text{NH}_2)$
97	0	0	96	0	0	0.75	0.86	0.75	6.0	0.0	99	93	71%, $\tau(\text{structure})$ + 16%, $\gamma(\text{C-C}\equiv)$ + 13%, $\gamma(\text{C-CL})$

The columns 4 to 10th collect the results at the B3LYP/6-311++G(3df,pd) level. In the column 7th is listed the Raman depolarization ratios for plane polarised (P), and unpolarized incident light (U), 8th column, reduced masses (μ), 9th column, and the force constant of each vibration (f), 10th column. To check the accuracy of methods, the calculated wavenumbers at the M06L and MP2 levels are also listed in the columns 11-12th, respectively. In the last column appears the characterization established by B3LYP for each calculated wavenumber determined in the ring modes. For the characterization of the ring modes was taking into account the atomic displacement vectors obtained in 4ABN molecule, and plotted in Fig 6. For the assignments of the ring modes was followed the Varsanyi's notation [75] for a 1,2,4-tri-substituted benzene. The modes corresponding to the substituents appear listed in Table 4.

Table 4. Modes corresponding to the substituents in 4A-2CBN

Modes	4A-2CBN
Stretching	7a, 7b, 13
In-plane bending	9a, 9b, 15
Out-of-plane bending	10a, 10b, 17a

Table 5 collects the scaled values with the linear scaling equation procedure (LSE) at three levels of computation, together with the results obtained by the procedure that uses two linear scaling equations and by the procedure that uses a polynomial scaling equation. For simplicity, in the last both cases only two levels of computation were used. The LSE procedure with two linear equations were used at the B3LYP/6-31G(d,p) level: one with the scaling equation reported by us [1,2], and another one, with a new scaling equation calculated by us here with better values. In both cases the results were very similar. All the calculated scaled wavenumbers



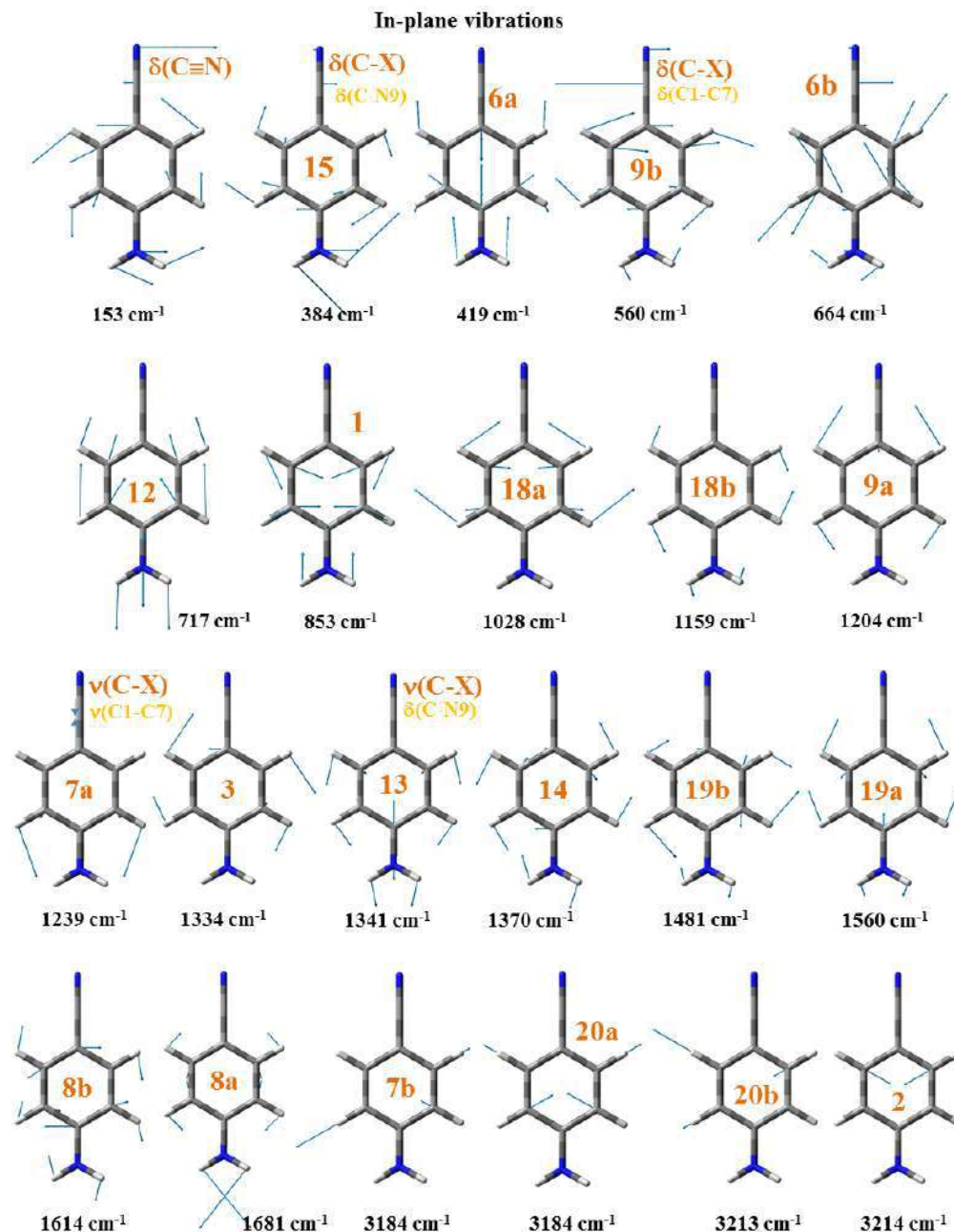


Fig 6. Characterization of the ring modes in 4-aminobenzonitrile molecule at the B3LYP/6-31G(d,p) level.

were compared to the experimental IR values obtained in KBr matrix and by Raman spectroscopy. Also for simplicity, the values obtained in Nujol mull were omitted in the Table because they appear very close to those in KBr matrix, Fig 4. The absolute error, $\Delta v = v(\text{scaled}) - v(\text{experimental})$ obtained for each method and procedure of scaling is included in the Table. The experimental values selected for this comparison appears underlined. Mainly they correspond to infrared values, and some cases, when it is observed an infrared value or it is not clear, from the Raman spectrum.

Table 5. Comparison of the scaled wavenumbers (ν , cm^{-1}) with different scaling procedures and at different DFT levels with the experimental values by IR and Raman spectroscopy, and the error obtained $\Delta\nu = \nu(\text{scaled}) - \nu(\text{experimental})$

B3LYP/6-31G (d,p) from [1,2]	scaling														Experimental		Assignment	
	LSE				Two eqns				polynomial				IR	Raman				
	B3LYP/6-31G (d,p)	B3LYP/6-31G++ G(3df, pd)	M06L/6-31G (d,p)	M06L/6-31G (d,p)	B3LYP/6-31G (d,p)	M06L/6-31G (d,p)	B3LYP/6-31G (d,p)	M06L/6-31G (d,p)	B3LYP/6-31G (d,p)	M06L/6-31G (d,p)	B3LYP/6-31G (d,p)	M06L/6-31G (d,p)						
ν	$\Delta\nu$	ν	$\Delta\nu$	ν	$\Delta\nu$	ν	$\Delta\nu$	ν	$\Delta\nu$	ν	$\Delta\nu$	ν	$\Delta\nu$	ν	$\Delta\nu$			
3092		3089		3078		3097		3085		3094		3084		3092		3127 vw	3127 vw	2, $\nu(\text{C-H})$ in C5-H, C6-H
3084	-8	3081	-11	3070	-22	3088	-4	3078	-14	3085	-7	3077	-15	3084	-8	3092 w	3085 vs	20b, $\nu(\text{C-H})$ in C3-H
3068	46	3065	43	3055	33	3081	59	3062	40	3077	55	3061	39	3076	54	3022 w	3030 vw,2925s	20a, $\nu(\text{C-H})$ in C5-H, C6-H
1603	21	1602	20	1595	13	1616	34	1605	23	1617	35	1612	30	1625	43	1582 s		8a, $\nu(\text{C=C}) + \beta_s(\text{NH}_2)$
1548	18	1547	17	1540	10	1557	27	1550	20	1559	29	1557	27	1566	36		1590 vs	8b, $\nu(\text{C=C})$
1493	-3	1492	-4	1486	-10	1503	7	1495	-1	1505	9	1501	5	1511	15	1496 vs	1530 w	19b, $\nu(\text{C=C})$
1426	-27	1425	-28	1422	-31	1442	-11	1428	-25	1444	-9	1434	-19	1450	-3	1453 vs	1455 m	19a, $\nu(\text{C=C})$
1315	-31	1315	-31	1305	-41	1350	4	1318	-28	1352	6	1322	-24	1357	11	1346 w	1386 m	14, $\nu(\text{C=C})$
1311	-3	1311	-3	1298	-16	1326	12	1315	1	1329	15	1318	4	1333	19	1314 s	1345 m	13, $\nu(\text{C4-N, CCC}) + \delta(\text{NH}_2)$
1244	-27	1243	-28	1247	-24	1246	-25	1247	-24	1249	-22	1249	-22	1252	-19	1271 vs	1320 w	3, $\delta(\text{C-H})$
1206	-1	1206	-1	1206	-1	1215	8	1210	3	1218	11	1212	5	1220	13	1207 sh	1279w,1255w	7a, $\nu(\text{C-C}\equiv, \text{CCC}) + \nu(\text{C}\equiv\text{N})$
1145	-19	1145	-19	1150	-14	1146	-18	1149	-15	1150	-14	1150	-14	1150	-14	1164m, 1132w	1210s, 1191sh 1178m,1146w	18b, $\delta(\text{C-H})$ 18a, $\delta(\text{C-H,CCC})$
1034	-1	1034	-1	1038	3	1046	11	1038	3	1050	15	1036	1	1049	14	1008 m	1035m,1015w	5, $\gamma(\text{C-H})$ in C5-H, C6-H
936	-14	936	-14	956	6	933	-17	947	-3	947	-3	937	-13	934	-16	950 m	975 w	1, $\delta(\text{CCC}) + \delta(\text{NH}_2) + \nu(\text{C-Cl})$
904	12	904	12	909	17	919	27	912	20	931	39	904	12	919	27	865vw, 892vw	871 w	17b, $\gamma(\text{C-H})$ in C3-H
835	-12	835	-12	861	14	835	-12	840	-7	841	-6	834	-13	833	-14	847 m	845 m	11, $\gamma(\text{C-H})$ in C5-H, C6-H
810	6	811	7	821	17	802	-2	813	9	806	2	808	4	800	-4	804 m	780 w	12, $\delta(\text{CCC}) + \delta(\text{C}\equiv\text{N}) + \delta(\text{NH}_2)$
713	-15	713	-15	721	-7	723	-5	710	-18	722	-6	709	-19	719	-9	728 vs	722 w	4, $\gamma(\text{CCC, C-C}\equiv)$
701	-9	701	-9	718	8	704	-6	697	-13	702	-8	696	-14	700	-10	710 sh		6b, $\delta(\text{CCC}) + \nu(\text{C-Cl})$
696	—	696	—	704	—	708	—	692	—	706	—	691	—	704	—			16b, $\gamma(\text{CCC}) + \gamma(\text{C}\equiv\text{N})$
608	-9	609	-8	621	4	610	-7	599	-18	601	-16	601	-16	603	-14		602 vs	9b, $\delta(\text{C-C}\equiv, \text{CCC}) + \delta(\text{C}\equiv\text{N})$
593	13	593	13	610	30	607	27	583	3	598	18	586	6	600	20	617 vw 580 m	582 vs	6a, $\delta(\text{C4-N,CCC}) + \omega(\text{NH}_2) + \delta(\text{C}\equiv\text{N})$
463	-3	464	-2	470	4	468	2	446	-20	449	-17	452	-14	457	-9		475 s	16a, $\gamma(\text{CCC}) + \omega(\text{NH}_2) + \gamma(\text{C}\equiv\text{N})$
452	41	453	42	458	47	446	35	435	24	426	15	441	30	434	23	466 sh	411 m	15, $\delta(\text{C4-N,CCC}) + \delta(\text{C}\equiv\text{N}) + \delta(\text{NH}_2)$
405	—	406	—	415	—	414	—	384	—	391	—	392	—	401	—			7b, $\nu(\text{C-Cl}) + \delta(\text{C}\equiv\text{N}) + \tau(\text{NH}_2)$
393	10	394	11	404	21	405	22	372	-11	382	-1	380	-3	392	9		391 m	10b, $\gamma(\text{C4-N,CCC}) + \gamma(\text{C}\equiv\text{N})$
268	8	269	9	275	15	274	14	240	-20	242	-18	251	-9	257	-3	383 br,s	305m, 260m	9a, $\delta(\text{C-CL, ring}) + \delta(\text{C}\equiv\text{N}) + \tau(\text{NH}_2)$
256	19	257	20	266	29	262	25	226	-11	230	-7	238	1	245	8	329 sh	237 m	10a, $\gamma(\text{C-CL, ring}) + \gamma(\text{NH}_2)$
196		197		204		197		163		159		176		177		237 sh	220 m	$\tau(\text{structure}) + \gamma(\text{C-C}\equiv) + 13\% \gamma(\text{C-Cl})$
115	13	116	14	123	21	124	22	77	-25	81	-21	92	-10	101	-1	221sh, 216 sh	102 br, m	

vs-very strong, s-strong, m-medium, w-weak, vw-very weak, sh, shoulder, ν -stretching, br-broad, δ -in-plane bending, γ -out-of-plane bending, τ -torsion, ω -wagging, br-broad.

Table 6. The cyano and amino groups of 4A-2CBN. Comparison of the calculated harmonic wavenumbers (ω , cm^{-1}), relative infrared intensities (A, %), relative Raman scattering activities (S, %), Raman depolarization ratios for plane polarised (P) and unpolarized (U) incident light, reduced mass (μ , amu), and force constant ($\text{mdyn}\cdot\text{\AA}^{-1}$, f) obtained at different levels. The scaled wavenumbers (ν , cm^{-1}) with the linear scaling equation are compared to the experimental values by IR and Raman spectroscopy.

		Calculated values										Scaled		Experimental		Assignment			
		B3LYP/6-311++G(3df,pd)					M06L/6-31G (d,p)					B3LYP/6-311++G(3df,pd)		M06L/6-31G (d,p)			IR	Raman	
ω	A	S	ω	A	S	P	U	μ	f	ω	ν	ω	ν	ω	ν				
3710	7	16	3695	11	10	0.75	0.86	1.1	8.9	3752	3547	3758	3563	3553	3490	3510	s	3490 m	100%, $\nu_{\text{asym}}(\text{NH}_2)$
3597	17	50	3591	24	43	0.16	0.27	1.0	7.9	3626	3448	3638	3455	3435	3420	3417	vs	3420 w	100%, $\nu_{\text{sym}}(\text{NH}_2)$
1678	100	21	1661	100	10	0.48	0.65	1.4	2.3	1693	1612	1712	1623	1624	1635	vs	1640 m	61%, $\beta_2(\text{NH}_2)$ + 39%, δ_a , $\nu(\text{C}=\text{C})$	
1092	0	0	1085	0	0	0.58	0.73	1.4	1.0	1104	1064	1134	1064	1073	1052	m		74%, $\tau(\text{NH}_2)$ + 24%, $\delta(\text{C}-\text{H})$	
436	37	0	431	89	1	0.51	0.68	1.5	0.2	438	442	406	438	449				51%, $\omega(\text{NH}_2)$ + 31%, $\gamma(\text{ring})$	
362	4	0	361	4	0	0.58	0.74	1.1	0.1	381	375	306	368	395	350	w	365	w	+12%, $\gamma(\text{C}\equiv\text{N})$
																			85%, $\tau(\text{NH}_2)$ + 13%, $\gamma(\text{C}-\text{H})$
2345	17	100	2327	27	100	0.28	0.44	12.7	40.4	2323	2245	2204	2260	2210	2235	vs	2237	vs	
135	1	1	137	1	1	0.71	0.83	14.0	0.2	133	162	131	151	148	162	vs	162	vs	91%, $\nu(\text{C}\equiv\text{N})$
515	4	1	519	4	0	0.75	0.86	8.7	1.4	519	526	478	514	511	558	vw,	560	m,	50%, $\delta(\text{C}\equiv\text{N})$ + 25%, $\delta(\text{C}-\text{CL})$
															500	vw	520	vw	+17%, $\delta(\text{ring})$
																			49%, $\gamma(\text{C}\equiv\text{N})$ + 37%, 17a, $\gamma(\text{C}-\text{C}\equiv\text{CCC})$

The values obtained in the substituent modes, C≡N and NH₂, are collected in Table 6. To understand the effect of substituents, these data were also compared with those obtained at the same computational level in 4ABN molecule. Only important modes are discussed in the present work. As the assignments for the remaining ring modes are obvious and therefore require no further discussion.

Table 7. The molecular-root-mean-square-error (rms), the mean-absolute-deviation (MAD), the standard deviation (SD), and the greatest positive and negative deviations from experiment for each level of computation and for the calculated and scaled wavenumbers of the ring modes of 4A-2CBN.

procedure	level	rms ^a	MAD	stanDev	Large error	
					minimum	maximum
calculated	B3LYP/6-31G(d,p)	49.0	30.0	39.6	-5.0	170.0
	6-311++G(3df,pd)	43.7	27.8	34.3	-8.0	156.0
	M06L/6-31G(d,p)	55.7	34.7	44.4	-6.0	189.0
	MP2/6-31G(d,p)	73.6	48.3	56.5	-41.0	237.0
LSE	B3LYP/6-31G(d,p), from [1,2]	18.8	15.0	11.6	-31.0	46.0
	6-31G(d,p)	18.9	15.2	11.4	-31.4	42.9
	6-311++G(3df,pd)	21.2	17.6	11.9	-41.0	47.0
	M06L/6-31G(d,p)	21.3	16.9	13.2	-25.0	58.8
Two equations	B3LYP/6-31G(d,p)	18.0	15.3	9.8	-27.6	39.7
	M06L/6-31G(d,p)	19.9	15.6	12.5	-22.0	55.5
polynomial	B3LYP/6-31G(d,p)	17.2	14.2	9.9	-24.1	38.9
	M06L/6-31G(d,p)	20.1	16.0	12.4	-19.3	54.4

^arms, defined as $[\sum(\omega^{\text{cal}} - \nu^{\text{exp}})^2/n]^{1/2}$, where n is the number of wavenumbers considered. ^bMAD, defined as $[\sum(\omega^{\text{cal}} - \nu^{\text{exp}})]/n$

Table 7 collects the rms (the molecular root mean square error), the MAD (mean absolute deviation), the SD (the standard deviation), and the greatest positive and negative deviations from experiment for each level of computation and each procedure of scaling. It is worthwhile to note the following:

(i) MP2 calculated wavenumbers are the worst. Their values appear with very large overestimation and underestimation amount, and its scaling (did not included in the Table for simplicity) does not give the enough improvement to be considered.

(ii) The M06L scaled wavenumbers with the three scaling procedures appear in general with slightly lower accuracy than those by the B3LYP method.

(iii) The B3LYP method with the large 6-311++G(3df,pd) basis set does not represent an improvement on the scaled wavenumber when it is used with the 6-31G(d,p) basis.

(iv) Both LSE linear equations used at the B3LYP/6-31G(d,p) level lead to similar results.

(v) The best procedure of scaling is that which uses a polynomial equation, although the difference is small as compared to the other two procedures, by the LSE and by the two linear scaling equations.

Therefore, the discussion is mainly based on B3LYP/6-31G(d,p) results, and those obtained by using the polynomial scaling equation.

C-X (X = Cl, C≡, and N9) modes

The $\nu(\text{C-X})$ stretching vibrations corresponding to substituents are the normal modes **13**, **7a** and **7b**, Table 4. Mode **13** corresponds to the amino substituent, $\nu(\text{C4-N})$, while **7b** is related to the chlorine atom, $\nu(\text{C-Cl})$, and mode **7a** to the cyano substituent, $\nu(\text{C-C}\equiv)$.

The in-plane bending, $\delta(\text{C-X})$ vibrations are the modes **15**, **9a** and **9b**. The mode **15** was identified corresponding to the amino substituent, $\delta(\text{C4-N})$, while mode **9a** to the chlorine atom, $\delta(\text{C-Cl})$, and mode **9b** to the cyano substituent, $\delta(\text{C-C}\equiv)$. The out-of-plane bending, $\gamma(\text{C-X})$ vibrations are the modes **17a**, **10a** and **10b**. According to the atomic displacement vectors, mode **10b** corresponds to $\gamma(\text{C4-N})$, while mode **10a** to $\gamma(\text{C-Cl})$ and **17a** to $\gamma(\text{C-C}\equiv)$.

C-Cl vibrations

The stretching vibrations belonging to the bond between the ring and the halogen atom generally give strong bands in the frequency range of $1130\text{--}480\text{ cm}^{-1}$ [76], and the wavenumber corresponding to these bands is influenced by the mass and bond strength of the neighboring substituents. Moreover, the smaller the halide atom the greater is the influence of the neighbor. In monochlorobenzene derivatives, such as in 4-chloro-3-nitrobenzonitrile [77], 2-amino-5-chlorobenzonitrile [78] and in 2-chloro-6-methyl benzonitrile [79], the C-Cl stretching wavenumber mainly appears in the $600\text{--}870\text{ cm}^{-1}$ range [75,80], whereas in dichlorobenzene derivatives, such as 2-amino-3,5-dichlorobenzonitrile [33], the main contributions are calculated at 397 and 381 cm^{-1} , and in 2,5-dichlorobenzonitrile they are computed at 459 and 330 cm^{-1} [56].

According to the Varsányi notation for a 1,2,4-trisubstituted benzene derivative, the $\nu(\text{C-X})$ stretching vibrations corresponding to the substituents are the normal modes **13**, **7a** and **7b**, Table 4. In these modes that corresponding to the chlorine substituent is characterized as **7b**. The halogen atom directly attached to the benzene ring interacts with its vibrations. With a “heavy” substituent, as in our case, the stretching vibrations appear strongly coupled with CCC, NH_2 and $\text{C}\equiv\text{N}$ modes, and thus they are expected to be calculated below 600 cm^{-1} . Thus, in 4A-2CBN it was computed at 389 cm^{-1} (scaled at 380 cm^{-1} by polynomial scaling equation at the B3LYP level) and well related to the experimental IR and Raman bands at 383 and 391 cm^{-1} , respectively. Weak contributions of this C-Cl stretching mode were also determined in the calculated vibrations at 924 and 706 cm^{-1} .

$\delta(\text{C-Cl})$ in-plane bending vibration is better characterized as mode **9a**, and it appears strongly coupled with $\delta(\text{C}\equiv\text{N})$ bending and $r(\text{NH}_2)$ rocking modes. This (C-Cl) in-plane bending mode was related to the experimental IR and Raman bands at 237 cm^{-1} . Also, a high % PED of the C-Cl bending is calculated in the vibration at 135 cm^{-1} and characterized as $\delta(\text{C}\equiv\text{N})$.

In general, C-X out-of-plane vibrations are also coupled with the substituents, making difficult their identification. Mode **10a** appears coupled with $\gamma(\text{NH}_2)$ mode, and it was related to the C-Cl substituent. By polynomial scaling equation it was scaled at 176 cm^{-1} , something far of the experimental IR and Raman bands at 216 and 220 cm^{-1} , respectively. Perhaps the anharmonic contribution of the $\gamma(\text{NH}_2)$ mode is responsible for this feature. A slight contribution of the $\gamma(\text{C-Cl})$ mode was also identified in the computed wavenumber at 97 cm^{-1} .

Cl-C7≡ and C4-N9 vibrations

The C1-C7 \equiv stretching (mode **7a**) is identified in the calculated vibration at 1241 cm^{-1} (scaled at 1212 cm^{-1}), in accordance to that calculated in 4ABN at 1239 cm^{-1} [17]. It is predicted with almost null IR intensity and medium-strong Raman intensity, and it was correlated to the shoulder detected in the IR spectrum at 1207 cm^{-1} and to the strong Raman band at 1210 cm^{-1} . The atomic displacement vectors for this

vibration look like mode **12**, instead of **7a**, according to the Varsányi description for a 1,2,4-trisubstituted benzene derivative. Thus, for a better assignment of the modes in 4A-2CBN and to avoid possible mistakes, their atomic displacements vectors were compared to those of the ring modes in 4ABN and plotted, Fig 6. Similar feature appears in the C4-N9 stretching mode **13**, calculated at 1351 cm^{-1} (scaled at 1318 cm^{-1}) with strong IR intensity and weak-very weak Raman intensity, and good related to the experimental strong IR band observed at 1314 cm^{-1} and to the weak band at 1320 cm^{-1} in Raman. In 4ABN this mode is calculated at 1341 cm^{-1} . However, according to the atomic displacement vectors for this vibration in benzene molecule it should be better characterized as mode **1** instead of **13**. Figure 6 helps in its well assignment as mode **13**.

The C-C \equiv in-plane bending (mode **9b**) was assigned to the computed wavenumber at 598 cm^{-1} , close to that calculated in 4ABN at 560 cm^{-1} . This mode is strongly coupled with the C \equiv N in-plane bending, with similar % PED as in 4ABN molecule. It appears scaled at 586 cm^{-1} in good accordance to the experimental IR band at 580 cm^{-1} and Raman line at 582 cm^{-1} .

Mode **15** corresponds to C4-N9 in-plane bending. Its characterization appears difficult due to the strong coupling with CCC, C \equiv N and NH₂ modes. It was calculated at 401 cm^{-1} , close to that at 384 cm^{-1} in 4ABN, i.e. the influence of the chlorine atom on this vibration is very less.

The highest %PED of the C-C \equiv out-of-plane bending mode **17a** appears in the computed wavenumber at 515 cm^{-1} , and mainly assigned as $\gamma(\text{C}\equiv\text{N})$ mode. In 4ABN the $\gamma(\text{C-C}\equiv)$ vibration corresponds to mode **11**, and it was calculated at 563 cm^{-1} [17].

Mode **10b** corresponds to the C4-N9 out-of-plane bending. It also appears strongly coupled with CCC and C \equiv N out-of-plane bending modes. It was calculated at 258 cm^{-1} , at exactly the same wavenumber as in 4ABN, i.e. the chlorine atom has no influence on this C4-N9 out-of-plane mode.

Phenyl ring modes

C-H modes

These modes are little affected by the nature of substituents and usually appear above 3000 cm^{-1} as weak to moderate bands [81-82]. The calculated three stretching C-H vibrations (modes **2**, **20a** and **20b**) appear in a very close frequency range, with the frequency corresponding to C3-H bond in the middle of those between C5-H and C6-H bonds. The range predicted for these modes are in good accordance to our scaled and experimental wavenumbers, Table 5. The calculated IR intensity is in general weak-very weak, in agreement with that observed in the experimental spectrum, and with strong Raman intensity, also in accordance to that found experimentally.

The in-plane C-H bending vibrations of the phenyl ring are expected to appear in the range $1000\text{-}1300\text{ cm}^{-1}$ [81]. In the present study, the in-plane bending, $\delta(\text{C-H})$ mode **18b** is predicted at 1150 cm^{-1} , while mode **18a** is predicted at 1036 cm^{-1} with medium intensity, in good accordance to the experimental IR band at 1164 cm^{-1} (**18b**) and with the band of medium Raman intensity at 1035 cm^{-1} for **18a**. The IR band detected at 1008 cm^{-1} can be tentatively assigned to this mode. Mode **3** is computed with high IR intensity, scaled at 1249 cm^{-1} and well related to the very strong IR band at 1271 cm^{-1} .

The out-of-plane C-H bending vibrations of the phenyl ring are expected to appear in the range $700\text{-}1000\text{ cm}^{-1}$ [81]. In the present study, three out-of-plane bending, $\gamma(\text{C-H})$ modes: **17b**, **11** and **5** appear identified in the $780\text{-}975\text{ cm}^{-1}$ range, also in good accordance with our scaled values, Table 5. We cannot distinguish clearly the modes **11** and **17b** by their atomic displacement vectors. In benzene and 4ABN molecule, mode **17b** appears at a higher wavenumber than **11**. Thus, the same can also happen in 4A-2CBN molecule, and therefore we can tentatively assign the calculated wavenumber at 852 cm^{-1} as mode **17b** and that at 826 cm^{-1} as mode **11**. Modes **5** and **11** were related to the C5-H and C6-H bonds, while mode **17b** to C3-H bond. Modes **17b** and **11** are predicted with medium IR intensity, in accordance to that observed in the IR spectrum.

C=C modes

They are calculated strongly coupled with C-H modes and in several cases coupled with C≡N stretching and bending vibrations. The coupling with amino modes is very small. The tangential vibrations **8a**, **8b**, **19a**, **19b** and **14** belong to the stretching group. Modes **8** and **19** are in general fairly insensitive to substitution [67-70]. In 1,2,4-trisubstitution the frequency of the **8a** component is higher than that of **8b**, while the frequency of component **19b** is greater than that of **19a**. This feature can be explained by the potential energy contribution of the C-H in-plane bending vibrations associated to each mode, and when it is large the frequency of the vibration is high. Thus, this contribution is calculated greater in **8a** than in **8b**, with a reduced mass of 2.2 and 6.2 amu, respectively, at B3LYP/6-31G(d,p) level and therefore mode **8a** appears at higher wavenumber than **8b**.

Modes **19b** and **19a** were calculated at 1541 (**19b**) and 1471 (**19a**) cm^{-1} in 4A-2CBN vs 1525 cm^{-1} in benzene molecule [1-2]). According to Scherer in the Varsanyi book [75] this vibration couples very strongly with vibrational pair **18**, with similar motion of the hydrogen atoms. The strong IR intensity calculated for mode **19b** is in accordance to the very strong band observed experimentally. The assignment of mode **14**, the Kekule ring stretching mode, is usually difficult because the displacement vectors of the hydrogen atoms do not follow the directions as they appear in benzene molecule [1-2].

Radial skeletal vibrations correspond to modes **1**, **12**, **6a** and **6b**, and they appear coupled strongly with stretching and bendings C≡N modes. Mode **1** was calculated with medium-weak intensity at 924 cm^{-1} (scaled at 904 cm^{-1}) and was good related to the IR band observed in KBr matrix at 892 cm^{-1} . Also it is predicted with weak Raman intensity, in agreement to the weak Raman line at 871 cm^{-1} . Mode **12** appears strongly coupled with C≡N and NH₂ bending modes and it is calculated with weak IR intensity and almost null Raman intensity. It is scaled at 709 cm^{-1} (721 cm^{-1} at B3LYP/6-311++G(3df,pd) level) in accordance to the experimental IR band at 728 cm^{-1} and to the weak Raman band at 722 cm^{-1} . Mode **6b** was calculated at 706 cm^{-1} in agreement with that determined in 4ABN at 664 cm^{-1} [17].

The displacement vectors of the computed wavenumber at 462 cm^{-1} do not permit its clear identification. However, in 4ABN mode **6a** is calculated at 419 cm^{-1} [17], and accordingly we have assigned the calculated vibration at 462 cm^{-1} in 4A-2CBN to this mode. It is scaled at 452 cm^{-1} and, therefore, it was related to the IR band at 466 cm^{-1} and to the Raman band at 475 cm^{-1} .

Out-of-plane skeletal vibrations corresponding to modes **4**, **16a** and **16b** of benzene were also accurately determined. The frequency of the normal mode **4** is rather insensitive to substitution. Thus, it is calculated at 711 cm^{-1} vs. 718 cm^{-1} in benzene molecule and 726 cm^{-1} in 4ABN [17]. It is predicted with almost null IR and Raman intensity, scaled at 696 cm^{-1} and therefore it is related to the shoulder detected at 710 cm^{-1} . Modes **16a** appears strongly coupled with out-of-plane C≡N and NH₂ vibrations that cause a frequency increase. Thus, it was calculated at 451 cm^{-1} vs. 415 cm^{-1} in 4ABN and in benzene molecule. Mode **16b** is predicted with weak IR intensity and scaled at 601 cm^{-1} , and therefore it was excellently related to the very weak experimental IR band at 617 cm^{-1} and Raman line at 602 cm^{-1} .

Amino group modes

The calculated and scaled wavenumbers using the scaling procedure mentioned above for the different modes of the amino group are collected in Table 6, together with the experimental IR and Raman data and the assignment including the %PED.

The NH₂ group involves the symmetric (ν_{sym}) and antisymmetric (ν_{asym}) N-H stretching vibrations. These modes can be easily identified and assigned on account of their characteristic magnitudes, however intramolecular bonding may lowers the magnitudes of these frequencies. The antisymmetric ν_{asym} stretching mode of NH₂ group appears calculated at a higher wavenumber (3710 cm^{-1} by B3LYP/6-31G(d,p)) than the symmetric ν_{s} one (3597 cm^{-1}). They were scaled by the LSE at 3563 and 3455 cm^{-1} , respectively, and they were related to the strong-very strong IR bands observed experimentally at 3510 and 3417 cm^{-1} , respectively.

The difference between theoretical and experimental can be attributed to intermolecular H-bonds in the solid state (not simulated in the present study) through this NH₂ group [72]. The predicted effect of the chlorine atom on these bands is very small. Thus, in 4ABN molecule they were computed at 3703 and 3591 cm⁻¹, respectively, only ca. 7 cm⁻¹ lower than to those calculated in 4A-2CBN. However, in the experimental IR bands the difference is larger, and in 4ABN [17] they were detected at 3490 (ν_{as}) and 3370 (ν_s) cm⁻¹ vs. 3510 (ν_{as}) and 3417 (ν_s) in 4A-2CBN. This large difference, which was not predicted theoretically, can be due to intermolecular H-bonds in the crystal through the NH₂ group which are stronger in 4ABN than in 4A-2CBN. Although there are no X-ray data of this molecule available in literature, the vibrational spectra in the solid state show that the chlorine atom in 4A-2CBN appears to reduce the strength of these H-bonds. As in other benzene derivatives [61], it is possible that in 4A-2CBN molecule the halogen atom forms intermolecular halogen bonds of type C-X...π (where X is a halogen atom). It is worthwhile to note that the calculated value of the intensity of ν_s mode is greater than ν_{as}, in agreement with that as observed in the IR spectra.

In the experimental IR spectrum of 4A-2CBN, two close strong bands were detected at 1635 and 1582 cm⁻¹ and on the basis of %PED they are assigned to the β_s(NH₂) and **8a** modes, respectively in consonance with two calculated strong bands which were scaled at 1623 and 1603 cm⁻¹. Both these modes appear to be coupled strongly and the % PED difference between them is: 61% of β_s(NH₂) in the band mainly assigned as β_s(NH₂), and 48% in the band assigned as mode **8a**. However, depending of the level of computation, this % PED can change and, therefore, the β_s(NH₂) mode can be assigned to a vibration at a wavenumber lower than that of mode **8a**, as it is predicted by M06L method, Tables 3 and 4. This feature is also observed in the case of 4ABN molecule [17].

Concerning the intensity, the scissoring mode β_s(NH₂) is calculated with the highest IR intensity, in accordance with that observed experimentally, which permits its clear identification in the spectra. The highest IR intensity computed for the β_s(NH₂) mode is also in accordance with that calculated in the aniline molecule [72]. However, in contrast, mode **8a** appears with intensity higher than β_s(NH₂) in the experimental Raman spectrum. This higher Raman intensity of mode **8a** than β_s(NH₂) was only accurately predicted by B3LYP/6-311++G(3df,pd).

The rocking mode of (NH₂) group, denoted as r (or δ_{as}), was scaled by B3LYP at 1064 cm⁻¹, almost at the same wavenumber obtained by M06L at 1062 cm⁻¹. In aniline molecule this mode appears strongly coupled with the **18a** ring mode [72]. However, in 4ABN and 4A-2CBN this coupling is weak, and r(NH₂) appears with a 74% PED. The chlorine atom slightly affects its wavenumber, thus it was scaled in 4ABN [17] at 1051 cm⁻¹ (calculated at 1078 cm⁻¹), and also with very weak or null IR and Raman intensity.

It seems extremely difficult to identify the experimental band corresponding to the position of the strongly anharmonic ω(NH₂) wagging vibration in the spectra of 4A-2CBN. In addition, this mode is sensitive to the intermolecular H-bonds through the NH₂ group. Therefore, we have not assigned this mode in the experimental spectra of 4A-2CBN, in agreement with previous authors [83]. However, on contrary the experimental band at 475 cm⁻¹ (IR) and 490 cm⁻¹ (Raman) in 4ABN have been assigned to this mode [17]. It is worthwhile to note that due to anharmonicity, mode mixing of inversion motion of hydrogen atoms of the NH₂ group with other out-of-plane motions cannot be described accurately, whereas in-plane normal mode motions can be reasonably modeled leading to lower errors .

The W(NH₂) mode in 4A-2CBN is calculated as the second strongest IR intensity band by B3LYP/6-311++G(3df,pd) and M06L/6-31G(d,p) with a relative IR intensity ca. 90, but by B3LYP/6-31G(d,p) it is lower with a relative IR intensity of 37, and in accordance with the experimental IR bands with weak-medium intensity which can be observed in the 400-500 cm⁻¹ range. This mode appears in the experimental spectra of aniline molecule and its derivatives as a very broad band with weak-medium intensity [72,84,85]. However, in the present case it was scaled by B3LYP/6-31G(d,p) at 438 cm⁻¹ using the linear scaling equation from the benzene molecule or at 456 cm⁻¹ using the equation from the amino group of aniline molecule [72]. The calculated wavenumber of W(NH₂) mode has little dependence on the basis set used, in accordance with

that observed in aniline molecule [72], but in contrast to that reported by other authors [19]. But, in aniline molecule, the value of wavenumber of this mode depends on the method used: by the B3LYP method and 6-31G(d,p) at 603 cm^{-1} , at 609.3 cm^{-1} with the 6-31+G(2d,p) basis, as well as with the 6-311++G(2d,p) at 608.0 cm^{-1} [71]. The computed wavenumber of this mode in 4A-2CBN, 436 cm^{-1} is lower than in aniline molecule [72] in accordance with a lower inversion angle ω calculated in 4A-2CBN molecule. At the B3LYP/6-311++G(3df,pd) level, the value in 4A-2CBN molecule is 31.5° (by X-ray is 34° [70]) while in aniline molecule [71] it is 39.7° .

Because the C_2 symmetry of the NH_2 group, the $\tau(\text{NH}_2)$ torsional band is not allowed by the IR selection rules. However, in the IR and Raman spectra can be identified a torsional band. This fact, as in the case of aniline molecule, was interpreted in Ref. [86,87] as combinations of the torsion and inversion vibrations (transit $1\leftarrow 0$), which are active in IR. In 4A-2CBN it is calculated at 362 cm^{-1} , which appears higher than calculated in 4ABN, 352 cm^{-1} , and in aniline molecule, 276 cm^{-1} . It can be explained as by the lowering of the inversion angle in 4A-2CBN and a shortening of the C-N bond, as compared to aniline molecule, which leads to an increment in the barrier height and hence to the wavenumber of the torsional mode. It is predicted with weak IR intensity at 368 cm^{-1} in accordance to the weak experimental IR band at 350 cm^{-1} . In 4ABN it has been assigned [17] to the experimental IR band at 330 cm^{-1} .

Vibrations of Nitrile ($\text{C}\equiv\text{N}$) group

The characteristic experimental wavenumber of $\text{C}\equiv\text{N}$ stretching vibrations of BNs falls ca. $2200\text{--}2300\text{ cm}^{-1}$ [80,88,89] with IR intensity which varies from medium-weak to strong depending on the substituents. However, as the geometry of the cyano group is not affected significantly by new substituents on the phenyl ring, therefore, their vibrational wavenumbers remain almost unchanged from the BN molecule [25,26]. In BN, $\nu(\text{C}\equiv\text{N})$ appears at 2230 cm^{-1} . Electron donating substituents, such as $-\text{NH}_2$, increase the IR intensity of $\nu(\text{C}\equiv\text{N})$ and decrease its frequency value, whereas the electron withdrawing groups ($-\text{F}$, $-\text{OH}$, and $-\text{Cl}$,) decrease the IR band intensity of $\nu(\text{C}\equiv\text{N})$ and increase its frequency to the higher limit of the characteristic spectral region [34,77,90-92].

In 4A-2CBN, the $\nu(\text{C}\equiv\text{N})$ stretching mode is highly localized on the $\text{C}\equiv\text{N}$ bond with a Potential Energy Distribution (PED) of 91%. It is slightly coupled with C1-C7 stretching to the extent of ca. 10%. It is calculated by all the methods with medium-strong IR intensity and very strong Raman intensity, the highest in the spectra. These results are in good agreement with the very strong experimental band observed at 2235 cm^{-1} in IR and at 2237 cm^{-1} in Raman spectra, and with the values obtained in other BNs [34]. The FTIR band intensity is slightly decreased by the electron withdrawing group ($-\text{Cl}$), while the Raman intensity is enhanced by the conjugation of the aromatic ring.

In the scaled bands at 713 , 696 , 593 cm^{-1} , and also in many bands below 500 cm^{-1} are determined contributions of the bending in-plane mode. However, the main contribution for the $\delta(\text{C}\equiv\text{N})$ mode is observed in the calculated band at 135 cm^{-1} with very weak IR intensity, and strongly coupled with C-Cl and ring bending vibrations. Due to this coupling, especially with the chlorine atom, this mode is calculated in 4A-2CBN at a lower wavenumber than in 4ABN molecule, 154 cm^{-1} .

The out-of-plane modes are identified in the calculated bands at 614 , 451 , 258 and 97 cm^{-1} , but the main contribution for the $\gamma(\text{C}\equiv\text{N})$ mode is observed in the calculated band at 515 cm^{-1} . This mode also appears strongly coupled with CC ring vibrations, and it is predicted with weak IR intensity and very weak Raman intensity in accordance with the experimental IR and Raman bands at 500 and 520 cm^{-1} , respectively.

Due to the linearity of the $\text{C}-\text{C}\equiv\text{N}$ bond, 179.9° by B3LYP/6-31G(d,p), sometimes the in-plane and out-of-plane bending vibrations appear calculated in reverse form, as in the present case with 4A-2CBN. Thus, $\delta(\text{C}\equiv\text{N})$ appears characterized at 135 cm^{-1} instead of at 515 cm^{-1} , $\gamma(\text{C}\equiv\text{N})$, and vice-versa. In other BN derivatives with other DFT methods, they are characterized in the right way. e.g. in 2,5-dichlorobenzonitrile [56] they are calculated at 621 cm^{-1} , $\delta(\text{C}\equiv\text{N})$ and at 138 cm^{-1} , $\gamma(\text{C}\equiv\text{N})$.

Combination bands

Several experimental Raman bands observed in the spectrum are far of the spectral range of the different ring modes and substituents modes. Thus, they can be assigned as combination bands: $1178+391=1569$ m, $871+391=1262$ m, and $780+475=1255$ w.

4.4 Other molecular properties

The values of the NBO atomic charges determined with the DFT and MP2 methods are listed in Table 2. For comparison purposes the calculated values in benzonitrile molecule are also included in the same Table. Some differences were observed between them. It is noted that the negative charge is mainly localized on the N9 atom, which produces the largest positive charge on the C4 atom. The chlorine atom has a very small positive charge. Thus, its effect on the BN structure is small, with a slight decrease in the positive charge on C7, and null effect on \equiv N atom.

The NBO atomic charges calculated by M06L method are in general larger than those calculated by B3LYP, but they are slightly lower than those calculated by MP2. The positive charge calculated by M06L on the chlorine atom is also larger than that calculated by B3LYP and MP2.

Thermodynamic parameters of 4A-2CBN were calculated and collected in Table 8. For an improvement in the determination of the Zero-Point Vibration Energies (ZPVE) and the entropy, $S_{\text{vib}}(T)$, the use of specific scale factors have been recommended [1-2], leading to the results shown in this Table. The translational, rotational and vibrational components are used to compute the entropy and free energy. The calculated values of the entropy by the three DFT methods appear very close and higher than those determined in BN molecule. These values of entropy indicate that as the temperature increases, the randomness of the molecules increases, i.e. the molecules will be distributed into a greater number of energy levels. At low temperatures, the translational energy levels contribute strongly to the behavior of entropy. Therefore, rotational and vibrational populations are distributed in a few low energy levels. At high temperatures, the vibrational population will be distributed in a larger number of vibrational levels, contributing to increase of entropy.

Table 8. Theoretical computed total energies and Gibbs Free energy (A.U.), rotational constants (GHz), entropies ($\text{cal}\cdot\text{mol}^{-1}\cdot\text{K}^{-1}$) and dipole moments (Debyes) at the B3LYP, M06L and MP2 levels in 4A-2CBN and BN molecules.

Parameters	4A-2CBN				BN	
	B3LYP/ 6-31G(d,p)	B3LYP/ 6-311++G (3df,pd)	M06L/ 6-31G(d,p)	MP2/ 6-31G(d,p)	B3LYP/ 6-31G(d,p)	MP2/ 6-31G(d,p)
Total energy + ZPE (AU)	0.346060 ^a	0.502477 ^a	0.288270 ^a	0.633023 ^b	0.400771 ^c	0.412258 ^d
Gibbs Free energy (AU)	0.380057 ^a	0.536457 ^a	0.322230 ^a	0.667270 ^b	0.431048 ^c	
Rotational constants (GHz)	1.87	1.89	1.9	1.89	5.65	5.65
	0.88	0.89	0.89	0.88	1.54	1.53
	0.6	0.61	0.61	0.6	1.21	1.21
Entropy ($\text{cal}\cdot\text{mol}^{-1}\cdot\text{K}^{-1}$)						
Total	92.02	91.96	91.84	93.12	78.56	79.44
Translational	40.97	40.97	40.97	40.97	39.8	39.81
Rotational	30.16	30.13	30.13	30.15	27.8	27.82
Vibrational	20.9	20.86	20.74	22.01	10.9	11.81
Dipole moments (Debyes)	7.55	7.51	7.74	7.37	4.55	5

^a-839. ^b-837. ^c-324. ^d-323.

A huge change is observed in the rotational constants. They were calculated very small as compared to BN. In the isolated state, by B3LYP they appear very close to those by MP2 and M06L methods.

The calculated dipole moment, Table 8, by M06L appears slightly higher than that calculated by MP2 and B3LYP, although the difference is small. The chlorine atom in 4A-2CBN has a little influence on the dipole moment of the molecule. Thus, the calculated value in 4-aminobenzonitrile is 6.53D by MP2 vs. 7.37 D in 4A-2CBN. The position in which the chlorine atom is bonded does not produce a remarkable change in the dipole moment, as compared to BN, but the effect of the NH₂ group is higher.

4.5MEP mapping

The other molecular properties like SCF energy, dipole moment, non-linear optical properties, HOMO-LUMO analysis and MEP mapping for the 4A-2CBN have been computed at B3LYP/6-311G(d,p) level of theory.

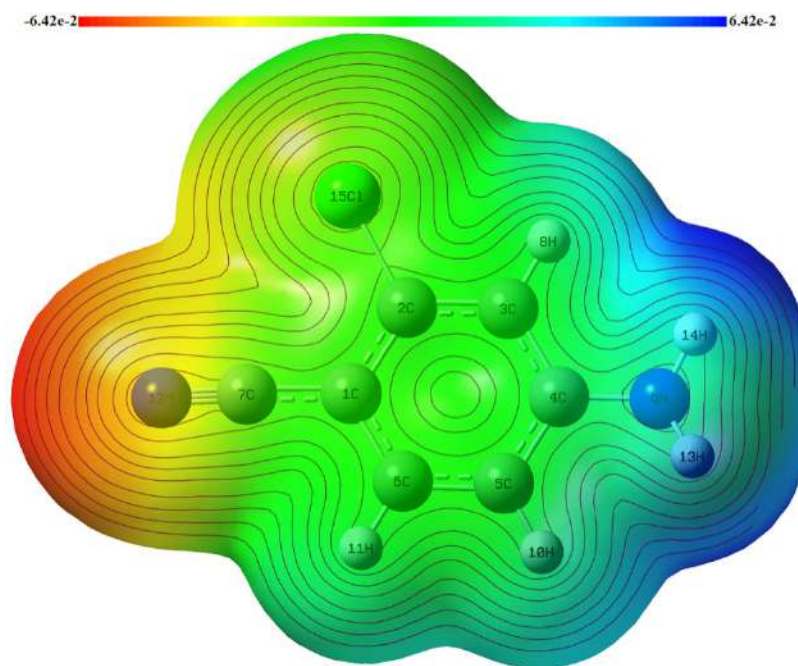


Fig 7. MEP diagram for the 4-amino-2-chlorobenzonitrile molecule

The molecular electrostatic potential (MEP) mapping have been used for understanding and predicting the sites of reactivity for electrophilic and nucleophilic reactions, investigation of biological recognition, hydrogen bonding interactions and other macroscopic properties [93]. The sign of the electrostatic potential in any particular site around a molecule that depends upon whether the effects of the nuclei or electrons are dominant is a key to assign its reactivity there [94]. The MEP surface is a plot of electrostatic potential mapped on to the constant electron density surface that represents the electrostatic potential in terms of colour coding [95,96], Fig 7. The surfaces with blue, green and red colours indicate the positive, zero and negative values of the potential, respectively. The red colour surfaces with negative MEP represent high electron density, whereas the blue colour surfaces with positive MEP correspond to areas of lowest electron density. MEP map for the 4A-2CBN is shown in Fig 7 with colour range from $-6.42e^{-2}$ (deepest red) to $+6.42e^{-2}$ (deepest blue). The surface over the hydrogen atom of NH₂ group shows maximum potential regions

(dark blue coloured/ low electron density) as well as the relatively lower potential sites (light blue coloured) are around the other hydrogen atoms. The surface over the electronegative atom nitrogen (N7) represents the minimum potential (dark red coloured/ high electron density). The blue and red colour regions can be referred to as the site for nucleophilic and electrophilic attack, respectively. Thus, electrophiles (positively charged species) and nucleophiles (negatively charged species) will attack on the red and blue coloured sites, respectively. The regions over the ring and chlorine atom are neutral as characterized by green colour.

4.6 HOMO-LUMO analysis

The highest occupied molecular orbital (HOMO) and lowest unoccupied molecular orbital (LUMO) are main Molecular Orbitals that play important role in chemical reactions. The HOMO acts as an electron donor while LUMO acts as electron acceptor, and for 4A-2CBN molecule they are plotted in Fig 8. The energy gap between the HOMO and LUMO molecular orbitals helps to determine the chemical stability and electrical transport properties of molecules. The lowest excitation energy corresponds to HOMO-LUMO transition under TD-DFT approach which approximates the gap accurately. This gap was computed at TD-B3LYP/6-31G(d,p) level of theory. The low value of gap represents the high reactivity of the molecule in chemical reactions. The HOMO is delocalized over the all atoms and bonds C≡N, C1-C2, C1-C6, C3-C4, C4-C5, C3-H, C5-H, N-H13 and N-H14 except on H11 atom, while, the LUMO is delocalized over the bonds C2-C3, C1-C6, C5-C6, C6-H, C5-H, N-H13, N-H14 and over all atoms except H18. Thus, HOMO-LUMO excitation shows the charge transfer that can be seen in Fig 8. The low value of the energy gap explains the eventual charge transfer interactions taking place within the molecule. The SCF energy, dipole moment, HOMO, LUMO energy eigenvalues and energy gap computed at B3LYP/6-31G(d,p) level of theory are presented in Table 9.

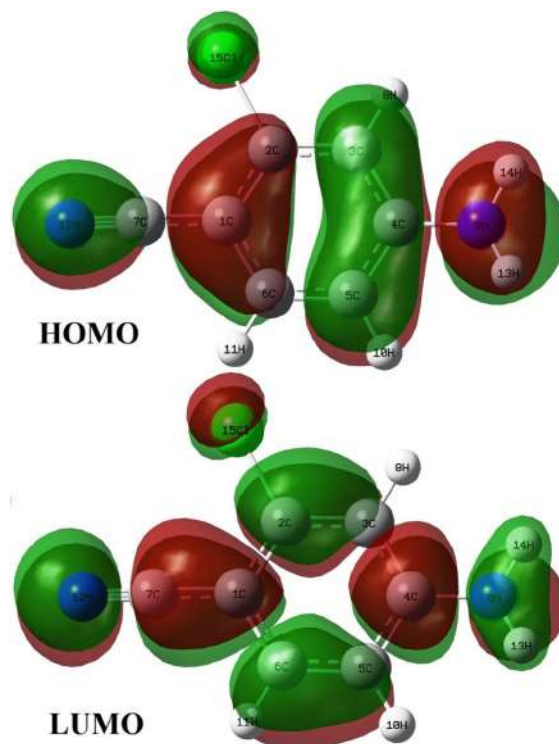


Fig 8. HOMO and LUMO plots for the 4-amino-2-chlorobenzonitrile.

Table 9. The SCF energy, HOMO, LUMO energy eigenvalues and HOMO-LUMO energy gap for the 4A-2CBN at the B3LYP/6-311G(d,p) level.

Energies	value
SCF energy (a.u.)	-839.452254
LUMO energy (eV)	-1.10
HOMO energy (eV)	-6.24
HOMO-LUMO gap (eV)	5.14
	4.68 ^a

^a approximated by using TD-B3LYP/6-31G(d,p) calculation

4.7 NLO properties

DFT calculations play an important role in designing the non-linear optical molecules. The molecules having the larger hyperpolarizability value show a strong NLO potential and can be used in fabrication of many optical devices. The molecules having donor-acceptor group attached to an aromatic ring increases the charge transfer through p-electron delocalization and give raise the hyperpolarizability values [97]. The polarizability, first order hyperpolarizability values and mean first order hyperpolarizability of the 4A-2CBN molecule were computed at B3LYP/6-31G(d,p) level of theory and they are presented in Table 10. The mean first hyperpolarizability of 4A-2CBN is 4.127×10^{-30} esu, which is 11 times greater than those of urea (for urea β_0 is 0.3728×10^{-30} esu) [93]. Thus, the high value of dipole moment and first order hyperpolarizability are representing the NLO potential of 4A-2CBN molecule.

Table 10. Calculated components of polarizability (a.u.), first order hyperpolarizability (a.u.), mean polarizability $\langle \alpha \rangle$ (a.u.), anisotropy of the polarizability γ (a.u.) and the mean first order hyperpolarizability β_0 (esu, 1 a.u. = 8.639×10^{-33} esu) of 4A-2CBN.

	B3LYP/6-31G(d,p)		B3LYP/-31G(d,p)
α_{xx}	149.02	β_{xxx}	-458.69
α_{xy}	7.56	β_{xxy}	-283.47
α_{yy}	101.29	β_{xyy}	73.63
α_{xz}	-1.80	β_{yyy}	-3.90
α_{yz}	-0.44	β_{xxz}	42.70
α_{zz}	34.65	β_{xyz}	11.82
$\langle \alpha \rangle$	94.99	β_{yyz}	6.46
γ	100.40	β_{xzz}	4.61
		β_{yzz}	2.72
		β_{zzz}	0.50
		β_0 (esu) $\cdot 10^{-30}$	4.13

5 Summary and Conclusions

In this paper, we attempted to provide a more comprehensive structural and vibrational study of 4A-2CBN by combining both theoretical and experimental data for the first time. Quantum chemical calculations were done to support the experimental results. Two conformations were computed in 4A-2CBN,

with the -NH_2 group in planar form being a saddle point. The most important findings of the present work are the following:

- (1) From the point of view of accuracy of the method, the equilibrium geometry calculated by the new M06L method in 4A-2CBN was compared with those obtained by B3LYP and MP2. In the calculated C-C bond lengths, M06L appears with the same accuracy as that by B3LYP, however at least by B3LYP with the 6-31G(d,p) basis set used, the $\text{C}\equiv\text{N}$ and C-Cl bond lengths are computed worse.
- (2) To improve the accuracy in the assignment of the calculated wavenumbers in the 4A-2CBN molecule, three different scaling equations procedures have been used. The best procedure of scaling is which uses a polynomial equation, although the difference is small as compared to the other two procedures, by the LSE and by the two linear scaling equations. Low errors were in general obtained in the scaled values.
- (3) For the first time the polynomial scaling equation, $y = a + b_1x + b_2 x^2$ procedure has been presented and used in the 4A-2CBN molecule. Its accuracy has been determined.
- (4) The M06L scaled wavenumbers appear in general with slightly lower accuracy than by B3LYP method
- (5) The calculated linear scaling equation by M06L with the benzene molecule leads to worse correlation coefficient r than by B3LYP. However, the relative IR and Raman intensities predicted by the three DFT methods are very similar. In general, the bands calculated by M06L appear shifted to higher wavenumbers related to those calculated by B3LYP and with larger errors as compared to the experimental results. Thus worse scaled wavenumbers are obtained with the M06L method, and therefore it is not recommended for its use, at least with the 6-31G(d,p) basis set. Further calculations with other molecules and basis set are required to confirm this feature.
- (6) The IR spectra of 4A-2CBN, in KBr matrix and in Nujol and as well its Raman spectrum in the solid state, were recorded and the bands observed were assigned accurately for the first time.
- (7) The assignments of the observed IR and Raman bands find support from related molecules and are consistent with the established ranges of the vibrations of the different modes. Therefore, they seem to be the most accurate today.
- (8) The main effect of the chlorine atom on the BN structure is a slight shortening of the C4-N and Cl-C \equiv bond lengths. Also it withdraws negative charge on the bonded atom C2. As a consequence, a small shortening of C2-C3 and C5-C6 bond lengths is observed as compared to BN, and a lengthening of C1-C2, and angles slightly out of the regular hexagonal structure.
- (9) As compared to MP2, the NBO atomic charges calculated by M06L are in general slightly better than those obtained by B3LYP. DFT methods appear to fail in the calculated charges on C4, C6 and N9 atoms.
- (10) The quinonoid structure of the BN molecule remains in 4A-2CBN, although its symmetry appears slightly modified by the chlorine atom.
- (11) In general C=C modes appear strongly coupled with C-H and $\text{C}\equiv\text{N}$ modes, while the amino modes appear as almost pure modes with very small coupling with other modes.
- (12) The size, shape, charge density distribution and structure activity relationship of the 4A-2CBN molecule were obtained by mapping electrostatic potential surface on the electron density isosurface. HOMO-LUMO energy was also computed. The high value of dipole moment and first order hyperpolarizability represent the NLO potential of 4A-2CBN molecule.

Acknowledgement

MAP wishes to thank NILS Science and Sustainability Programme (ES07), 002-ABEL-CM-2014A Call for financial support. Supported by a grant from Iceland, Liechtenstein and Norway through the EEA

Financial Mechanism. Operated by Universidad Complutense de Madrid. The authors (DB, and VKR) are thankful to Sri Rakesh Mohan Garg, Chairman R D Group of Institutions, Kadrabad, Ghaziabad, India, for providing computer facility in the Institute.

References

1. Palafox M A, Recent Research Developments in Physical Chemistry, India: Transworld Research Network, 2 (1998) 213-232.
2. Palafox M A, *Int J Quantum Chem*, 77(2000)661-684.
3. Palafox M A, Rastogi V K, *Spectrochim Acta*, A 58(2002)411-440.
4. Palafox M A, Rastogi V K, Mittal L, *Int J Quantum Chem*, 94(2003)189-204.
5. Palafox M A, Rastogi V K, Mittal L, Kiefer W, Mital H P, *Int J Quantum Chem*, 106(2006)1885-1901.
6. Imahori H, El Khouly M E, Fujitsuka M, Ito O, Sakata Y, Fukuzumi S, *J Phys Chem B*, 101(2001)325-332.
7. (a) Butera J A, Antane M M, Antane S A, Argentieri T M, Freeden C, Graceffa R F, Hirth B H, Jenkins D, Lennox J R, Matelan E, Norton N W, Qluagliato D, Sheldon J H, Spinelli W, Warga D, Wojdan A, Woods M, *J Med Chem*, 43(2000)1187-1202.
(b) Butera J A, Antane M M, Antane S A, Argentieri T M, Freeden C, Graceffa R F, Hirth B H, Jenkins D, Lennox J R, Matelan E, Norton N W, Qluagliato D, Sheldon J H, Spinelli W, Warga D, Wojdan A, Woods M, *J Med Chem*, 43(2000)1203-1214.
8. Kagara K, Goto S, Ichihara M, *J Synt Org Chem Jpn*, 57(1999)415-421.
9. Fadda A A, Afash M El-Sayed, Awad R S, *Eur J Med Chem*, 60(2013)421-430.
10. Zhang S, Zhang Y, Ma X, Lu L, He Y, Deng Y J, *J Phys Chem B*, 117(2013)2764-2772.
11. Tan W, Zheng D, Wu H, Zhu D, *Tetrahedron Lett*, 49(2008)1361-1364.
12. Peng L, Zhang L, Cheng X, Feng L S, Hao H Q, *Plant Biol*, 15(2013)404-414.
13. Veselá A B, Pelantová H, Sůlc M, Macková M, Lovecká P, Thimová M, Pasquarelli F, Pičmanová M, Pátek M, Bhalla T C, Martinkova L, *J Ind Microb Biotechnol*, 39(2012)1811-1819.
14. Koopman H, Daams J, *Weed Research*, 5(1965)319-326..
15. Björklund E, Styrihave B, Anskjær G G, Hansen M, Sørensen B H, *Sci Total Environ*, 409(2011)3732-3739..
16. Agarwal P, Bee S, Gupta A, Tandon P, Rastogi V K, Mishra S, Rawat P, *Spectrochim Acta*, A121(2014)464-482.
17. Palafox M A, Rastogi V K, Vats J K, *J Raman Spectrosc*, 37(2006)85-99.
18. Vujovic D, Raubenheimer H G, Nassimbeni L R, *Eur J Inorg Chem*, 14(2004)2943-2949.
19. Kolek P, Pirowska K, Najbar J, *Phys Chem Chem Phys*, 3(2001)4874-4888.
20. Kolek P, Pirowska K, Chacaga L, Najbar J, *Phys. Chem Chem Phys*, 5(2003)4096-4107.
21. Kolek P, Pirowska K, Gora M, Kozik B, Najbar J, Kolek P, Pirowska K, Gora M, Kozik B, Najbar J, *Chem Phys*, 285(2002)55-72.
22. Rastogi V K, Jain D K, Sharma Y C, *Asian J Chem*, 3(1991)113-115.
23. Rastogi V K, Palafox M A, Lal B, Jain V, *Indian J Pure & Appl Phys*, 38(2000)564-569.
24. Singh N P, Yadav R A, *Ind J Phys B*, 75(2001)347-355.
25. Rastogi V K, Palafox M A, Singhal S, Ojha S P, Kiefer W, *Int J Quantum Chem*, 107(2007)1099-1114.
26. Rastogi V K, Singhal S, Kumar A P, Rao G R, Palafox M A, *Indian J Pure & Appl Phys*, 47(2009)844-851.
27. Palafox M A, Rastogi V K,, In Perspectives in Modern Optics & Optical Instrumentation, J. Joseph. A. Sharma A, Rastogi V K, Eds; Anita Publications, Delhi, Ghaziabad, India, 2002, 91-98.
28. Sudha S, Sundaraganesan N, Kurt M, Cinar M, Karabacak M, *J Molec Struct*. 985(2011)148-156.
29. Nataraj A, Balachandran V, Karthick T, *J Molec Struct*, 1038(2013)134-144.

30. Jeyavijayan S, Arivazhagan M, *Spectrochim Acta*, A81(2011)466-474.
31. Rastogi V K, Arora C B, Singhal S K, Singh D N, Yadav R A, *Spectrochim Acta*, A53(1997)2505-2510.
32. Rastogi V K, Jain V, Palafox M A, Singh D N, Yadav R A, *Spectrochim Acta*, A57(2001)209-216.
33. Rastogi V K, Palafox M A, Tomar R, Singh U, *Spectrochim Acta*, A110(2013)458-470.
34. Rastogi V K, Palafox M A, Tanwar R P, Mittal L, *Spectrochim Acta*, A58(2002)1987-2004.
35. Sundaraganesan N, Meganathan C, Joshua B D, Mani P, Jayaprakash A, *Spectrochim Acta*, A 71(2008)1134-1139.
36. Krishnakumar V, Dheivamalar S, *Spectrochim Acta*, A71(2008)465-470.
37. Goyal Y, Alam M J, Bhat D, Ahmad S, Palafox M A, Rastogi V K., Fifth International Conference on Perspectives in vibrational spectroscopy, (ICOPVS-2014), Kerala (India) (2014).
38. Rasheed Tabish, Ahmad Shabbir, *Spectrochim Acta*, A 77(2010)446-456.
39. Seminario J M, Politzer P (Eds), Modern density functional theory: a tool for chemistry, Vol 2, (Elsevier, Amsterdam),1995
40. Palafox M A, Tardajos G, Kim J J, Nielsen O F, Lodhi R, Rastogi V K, *Asian J Phys*, 15(2006)281-285.
41. Ponomareva A G, Yurenko Y P, Zhurakivsky R O, Mourik T van, Hovorun D M, *Phys Chem Chem Phys*, 14 (2012)6787-6795.
42. Shishkin O V, Pelmenshikov A, Hovorun D M, Leszczynski J, *J Molec Struct*, 526(2000)329-341.
43. Shishkin O V, Gorg L, Zhikol O A, Leszczynski J, *J Biomol Struct Dyn*, 21(2004)537-553.
44. Shishkin O V, Gorg L, Zhikol O A, Leszczynski J, *J Biomol Struct Dyn*, 22(2004)227-243.
45. Palamarchuk G V, Shishkin O V, Gorb L, Leszczynski J, *J Biomol Struct Dyn*, 26(2009)653-661.
46. Brovarets O O, Hovorun D M, *J Biomol Struct Dyn*, 32(2014)127-154.
47. Palafox M A, *J Biomol Struct Dyn*, 32(2014)831-851.
48. (a) Palafox M A, Posada-Moreno P, Villarino-Marín A L, Martínez-Rincon C, Ortuño-Soriano I, Zaragoza-García I, *J Comput Aided Molec Design*. 25(2011)145-161.
(b) Alvarez-Ros M C, Palafox M A, *Pharmaceuticals*, 7(2014)695-722.
49. Hoffmann M, Rychlewski J, *Rev Mod Quant Chem*, 2(2002)1767-1803.
50. Arjunan V, Raj A, Anitha R, Mohan S, *Spectrochim Acta*, A125(2014)160-174.
51. Arjunan V, Govindaraja S T, Jose S P, Mohan S, *Spectrochim Acta*, A128(2014)22-36.
52. Arjunan V, Devi L, Subbalakshmi R, Rani T, Mohan S, *Spectrochim Acta*, A 130(2014)164-177.
53. Sundaraganesan N, Mariappan G, Manoharan S, *Spectrochim Acta*, A87(2012)67-76.
54. Szafran M, Ostrowska K, Katrusiak A, Dega-Szafran Z, *Spectrochim Acta*, A128(2014)844-851.
55. Kattan D, Palafox M A, Kumar S, Manimaran D, Joe I H, Rastogi V K, *Spectrochim Acta*, A123(2014)89-97.
56. Palafox M A, Bhat D, Goyal Y, Ahmad S, Joe I H, Rastogi V K, *Spectrochim Acta*, A136(2015)464-472
57. Palafox M A, Jothy V B, Singhal S, Joe I H, Kumar S, Rastogi V K, *Spectrochim Acta*, A116(2013)509-517.
58. Zhao Y, Truhlar D G, *J Chem Phys*, 125(2006)194101; doi.org/10.1063/1.2370993
59. Gaussian 09, Revision D.01, Frisch M J, Trucks G W, Schlegel H B, Scuseria G E, Robb M A, Cheeseman J R, Scalmani G, Barone V, Mennucci B, Petersson G A, Nakatsuji H, Caricato M, Li X, Hratchian H P, Izmaylov A F, Bloino J, Zheng G, Sonnenberg J L, Hada M, Ehara M, Toyota K, Fukuda R, Hasegawa J, Ishida M, Nakajima T, Honda Y, Kitao O, Nakai H, Vreven T, Montgomery J A (Jr), Peralta J E, Ogliaro F, Bearpark M, Heyd J J, Brothers E, Kudin K N, Staroverov V N, Kobayashi R, Normand J, Raghavachari K, Rendell A, Burant J C, Iyengar S S, Tomasi J, Cossi M, Rega N, Millam J M, Klene M, Knox J E, Cross J B, Bakken V, Adamo C, Jaramillo J, Gomperts R, Stratmann R E, Yazyev O, Austin A J, Cammi R, Pomelli C, Ochterski J W, Martin R L, Morokuma K, Zakrzewski, G.A. Voth G A, Salvador P, Dannenberg J J, Dapprich S, Daniels A D, Farkas Ö, Foresman J B, Ortiz J V, Cioslowski J, Fox D J, Gaussian, Inc., Wallingford CT, 2009.
60. Zhao Y, Truhlar D G, *Chem Phys Lett*, 502(2011)1-13.

61. Sert Y, Mirosław B, Çırak C, Doğan H, Szulczyk D, Struga M, *Spectrochim Acta*, A128(2014)91-99.
62. Carpenter J E, Weinhold F, *J Molec Struct*, (Theochem), 169(1988)41-62.
63. Reed A E, Curtiss L A, Weinhold F, *Chem Rev*, 88(1988)899-926.
64. Polavarapu P L, *J Phys Chem*, 94(1990)8106-8112.
65. Kerestztury G, Holy S, Varga J, Bensenya G, Wng A Y, Durig J R, *Spectrochim Acta*, A49(1993)2007-2026.
66. Kerestztury G, Raman spectroscopy theory, in Chalmers J M, Griffiths P R (Eds), *Handbook of Vibrational Spectroscopy*, vol 1, (Wiley), 2002, pp 71-87.
67. Casado J, Nygaard L, Sørensen G O, *J Mole Struct*, 8(1971)211-224.
68. Islor A M, Chandrakantha B, Gerber T, Hosten E, Betz R, Kristallogr Z, *NCS*, 228(2013)217-218; doi: 10.1524/nrcs.2013.0107.
69. Merlino S, Sartori F, *Acta Crystallogr*, B38(1982)1476-1480.
70. Heine A, Herbst-Irmer R, Stalke D, *Acta Crystallogr B*, 50(1994)363-373.
71. Palafox M A, Núñez J L, Gil M, *J Molec Struct (Theochem)*, 593(2002)101-131.
72. Palafox M A, Gil M, Núñez J L, Rastogi V K, Mittal L, Sharma R, *Int J Quantum Chem*, 103(2005)394-421.
73. Palafox M A, Rastogi V K, *Spectrochim Acta*, A 58(2002)411-440.
74. Palafox M A, Núñez J L, Gil M, Rastogi V K, *Perspectives in Engineering Optics*, Singh K, Rastogi V K, eds, (Anita Publications, Delhi-Ghaziabad), 2002, pp 356-391.
75. Varsanyi G, *Assignments for vibrational Spectra of Seven hundred benzene derivatives*, Vol 1, (Adam Hilger, London), 1974, pp. 280.
76. (a) Mooney E F, *Spectrochim Acta*, 20(1964)1021-1032.
(b) Mooney E F, *Spectrochim Acta*, 19(1963)877-887.
77. Sert Y, Çırak C, Uçun F, *Spectrochim Acta*, A 107(2013)248-255.
78. Lakshmaiah B, Rao G R, *J Raman Spectrosc*, 20(1989)439-448.
79. Kumar V, Panikar Y, Palafox M A, Vats J K, Kostova I, Lang K, Rastogi V K, *Indian J Pure & Appl Phys*, 48(2010)85-94.
80. Faniran J A, Iweibo I, Oderinde R A, *J Raman Spectrosc*. 11(1981)477-480
81. Roeges N P, *A Guide to the complete interpretation of infrared spectra of organic structures*, (Wiley, New York), 1994;
82. Coates J, *Encyclopedia of Analytical Chemistry*, in Meyers R A (ed), *Interpretation of Infrared Spectrum: A Practical Approach*, (John Wiley, Chichester), 2000.
83. Ram S, Yadav J S, Rai D K, *Ind J Phys B*, 59(1985)19.
84. Palafox M A, *Asian J Phys*. 2(1993)72-80.
85. Palafox M A, *Indian J Pure & Appl Phys*, 30(1992)59-66.
86. Palafox M A, *J Mole Struct*, 175(1988)81-84.
87. Larsen N W, Hansen E L, Nicolaisen F M, *Chem Phys Lett*, 43(1976)584-586.
88. Lin-Vien D, Colthup N B, Fateley W G, Grasselli J G, *The Handbook of Infrared and Raman Characteristic frequencies of Organic Molecules*, (Academic Press Inc, San Diego, California), 1991.
89. Dollish F R, Fateley W G, Bentley F F, *Characteristic Raman Frequencies of Organic Compounds*, (Wiley, New York), 1974.
90. Arivazhagan M, Meenakshi R, Prabhakaran S, *Spectrochim Acta*, A102(2013)59-65.
91. Arjunan V, Carthigayan K, Periandy S, Balamurugan K, Mohan S, *Spectrochim Acta*, A98(2012)156-169.
92. Dheivamalar S, Silambarasan V, *Spectrochim Acta*, A96 (2012) 480-484.
93. Arivazhagan M, Kumar J S, *Indian J Pure & Appl Phys*, 50(2012)363-373.
94. Sapse A M, *Molecular Orbital Calculations for Biological Systems*, (Oxford University Press, New York), 1998.

95. Alam M J, Ahmad S, *Spectrochim Acta*, A128(2014)653-664 and ref. cited therein.
96. Alam M J, Ahmad S, *J Molec Struct*, 1059(2014)239-254.
97. <http://www.sigmaaldrich.com/materials-science/organic-electronics/photonic-optical-materials/tutorial/nlo-materials.html>

[Received: 25.01.2016; revised recd: 12.02.2016; accepted: 28.02.2016]

Dr M Alcolea Palafox is currently Full Professor in Chemical Physics Department, Chemistry Faculty, UNIVERSIDAD COMPLUTENSE DE MADRID, Spain. His major research areas are Vibrational spectroscopy of biomolecules, Quantum chemistry of biomolecules, Molecular structure of anti-virus and anti-cancer drugs, Structure-activity relationships. He has published more than 175 research papers in International Journals and have a strong collaboration with Prof Vinod Rastogi. He is Founding Member of Editorial Board of Asian J Phys and Editor of Asian Chem Letts.



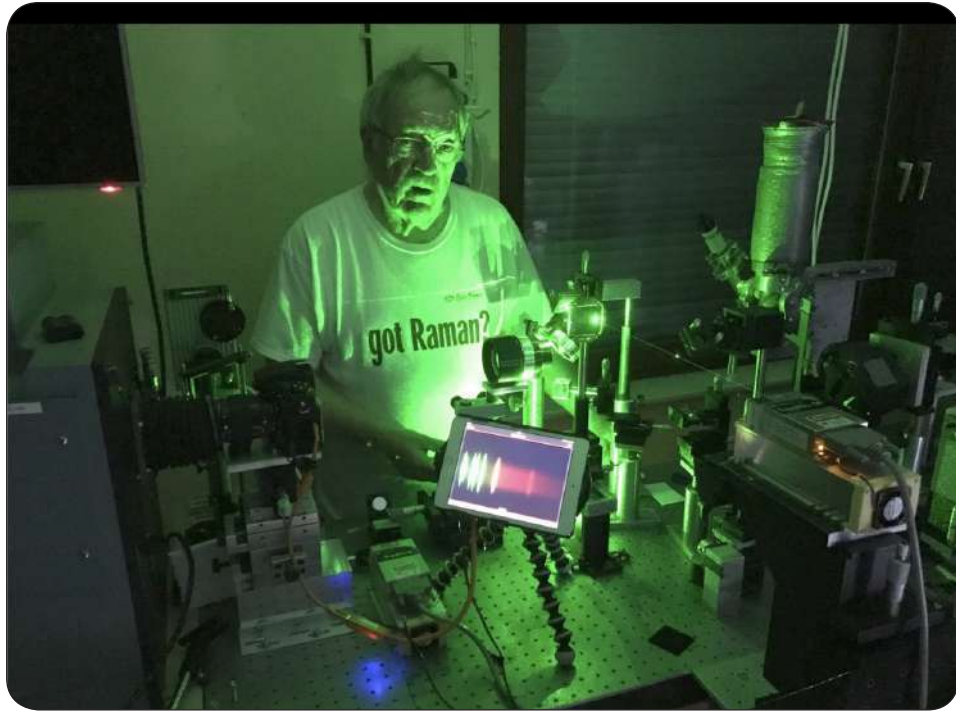
Wolfgang Kiefer
and
His Activities



WK as electronic technician at ELARS (WK is soldering electronics for Raman Laser Beamer)



WK as machinist at ELARS (WK is making part of Raman Laser Beamer)



WK as spectroscopist at ELARS

The *ELARS* Raman Laser Beamer



Model ELRB 2 (1 W, 532 nm, aircooled)

Kramers – Heisenberg – Dirac :
Quantum Theory for Inelastic Light Scattering
„The KHD dispersion relation“



H. A. Kramers ca. 1928



W. Heisenberg ca. 1931



P. A. M. Dirac ca. 1925

„Coherent Raman“
as seen on a
Powerpoint slide



Raman in coherent light
at ca. 5 m distance

The ELARS Raman Laser Beamer

Pleasant Memories

*We all have our time machines.
Some take us back, they're called memories.
Some take us forward, they're called dreams.*



